# Acoustic modeling and design of MRI scanners

# Acoustic modeling and design of MRI scanners

## Proefschrift

ter verkrijging van de graad van doctor
aan de Technische Universiteit Eindhoven,
op gezag van de Rector Magnificus, prof.dr. M. Rem,
voor een commissie aangewezen door het College voor Promoties
in het openbaar te verdedigen op
donderdag 14 januari 1999 om 16.00 uur

door

Adrianus Henricus Wouterus Maria Kuijpers

geboren te Gemert

Dit proefschrift is goedgekeurd door de promotoren:

prof.dr.ir. J.W. Verheij
en
prof.dr.ir. D.H. van Campen

Copromotor:

dr.ir. G. Verbeek

*They always say: "do what you got to do."*
*I always say: "do what's good for you."*
*They always say: "work it for success."*
*I think you should do what makes your heart hurt less.*

*From: The Paladins – follow your heart –*

*Voor Yvonne en mijn ouders*

# Contents

# Summary

A magnetic resonance imaging (MRI) scanner is a medical diagnostic device for imaging of the internal structures of the human body. A well known problem of MRI scanners is their large noise production (up to $90 - 120$ dB(A)) during the scanning process. The noise is produced by the strong vibration of the so-called gradient coil system. In the future, it is expected that new, faster scanning techniques will increase the noise problem. In the interest of patients, operators, and medical staff, it will be necessary to reduce these noise levels considerably in future scanners. Therefore, it is necessary to assess the acoustic performance of the MRI scanner early in the design phase to obtain substantially quieter scanners.

A model for the noise production of MRI scanners can be subdivided in two parts: a structural and an acoustic part. The structural part of the model deals with the generation of structural vibrations due to Lorentz forces excitations. The acoustic part describes the transformation of the structural vibrations into audible noise. This thesis only deals with models for the acoustic part of the noise problem. In a companion doctoral thesis, Kessels [1999] covers the structural part of the MRI noise problem and structural-acoustic optimization techniques.

An adequate acoustic model for low-noise design of MRI scanners should satisfy two important demands: the model must incorporate the relevant aspects of the MRI scanner noise problem and at the same time be practically manageable for the developers of MRI scanners. Therefore, the objective of research presented in this thesis is twofold. On the one hand the research is aimed at the development of accurate and efficient numerical tools to model the noise problem of the MRI scanner. On the other hand it tries to identify the acoustically relevant parameters in the design of a more quiet MRI scanner.

In order to reach the first part of the objective, the development of accurate and efficient numerical tools, three acoustic formulations were developed to model the acoustic radiation of the MRI scanner:

- A semi-analytical formulation for the acoustic radiation of a finite duct with open ends mounted with infinite flanges.
- An acoustic boundary element method (BEM) with Fourier elements.
- A modal description of the acoustics based on the radiation modes formulation.

The semi-analytical formulation was developed to gain insight into the physics of this specific acoustic problem. The method is derived within the general linear duct acoustics theory. The acoustic field inside the finite duct with infinite flanges is described with Fourier-Bessel duct modes. The reflection of acoustic waves at the duct's exits is described with reflection coefficients. Due to the use of special integration techniques, the efficiency

of this method, compared to element based discretization methods, was further improved. Moreover, the formulation offers more insight into the acoustic characteristics of these baffled, finite duct-like structures. However, this model is only applicable to model scanners with a simplified bore having a constant cross section. Therefore, this model should be used primarily for exploratory design studies of general influence parameters, not for detailed acoustic studies of realistically shaped MRI scanners.

A Fourier BEM model was developed to enable the acoustic analysis of axisymmetric structures in general and MRI scanners with a more complex geometry in particular. Compared to acoustic calculations with 3-dimensional BEM formulations, the computation times using the Fourier BEM formulation can be reduced from weeks to one hour. For that, the scanner's geometry is assumed to be axisymmetric and the acoustic variables are described with Fourier series in circumferential direction. This splits up the 3-dimensional acoustic radiation problem into a series of 'quasi-axisymmetric' radiation problems; one for each Fourier harmonic in the series.

The novelty of the Fourier BEM method presented in this thesis lies in the handling of the Fourier integrals in the formulation. Traditionally, these are computed separately for each Fourier harmonic in the series, which requires large computational efforts. By using fast Fourier transform (FFT) algorithms, these Fourier integrals can be computed simultaneously, which causes a considerable speedup, especially when the Fourier series contain more than a few terms.

With the radiation modes formulation, it is possible to identify those components of the vibration field that contribute most to the radiated sound power. Through an eigenvalue analysis of the so-called power coupling matrix, the radiation modes and their associated radiation efficiencies can be found. With these, the vibration distribution can be subdivided into radiating and non-radiating components. The radiation mode shapes and efficiencies only depend on the frequency and on the geometry of the radiating surface, not on the structural properties of the radiator.

Design alterations to an important class of structural parameters (e.g. the material properties, support or load) only change the boundary conditions of the acoustic problem, not the geometry of the acoustic domain itself. This observation was used in a model reduction technique based on the radiation modes formulation. Using this technique, only one complete acoustic analysis is required for each geometry in a design study. In subsequent acoustic analyses, the results of the first analysis can then be reused. Hence, the total computation time for all acoustic analyses can be drastically reduced. This is especially advantageous in optimization studies.

To reach the second part of the research objective, the research on the relevant design parameters for an MRI scanner, the three developed acoustic tools were deployed in a number of preliminary design studies. First, as a rough approximation, the MRI scanner was modeled as a finite duct ending in infinite flanges. This model was analyzed using the semi-analytical formulation. The acoustics of this simplified MRI scanner model, were found to be dominated by so-called near cut-on resonances. These resonances are caused by a high auto-reflection coefficient of a Fourier-Bessel duct mode near its cut-on frequency. The high reflection causes a large amount of the outgoing acoustic wave to be reflected back into the duct. If the phase of outgoing and reflected waves match well, then resonance occurs. This causes peaks in the frequency spectra of the sound power, the sound pressure and the radiation efficiency levels.

The geometry of the bore was found to be an acoustically important parameter for the MRI design. MRI scanner models with a more realistically shaped bore were analyzed with the Fourier BEM. For these models, the near cut-on resonances are still visible, but the corresponding peaks in the noise spectra are smaller. This is caused by a gradually increasing radius of the bore towards the ends, which decreases the auto-reflection coefficients and therefore reduces the resonance phenomena. The radius of the part of the bore with constant cross-section determines the location of the cut-on frequencies. The influence on the acoustics of the outer scanner diameter was found to be negligibly small.

Another design parameter for the MRI scanner is the presence of a patient in the MRI bore. The influence of the patients position in the scanner and the influence of acoustic absorption of the patient's clothing on the scanner's sound radiation was investigated. The position of the patient was found to have some influence on the location of the 'cut-on' frequencies, whereas the clothing absorption seemed to cancel out these effects. Because of the observed small influence on the total noise levels, it is unnecessary for design purposes to model a patient in the MRI scanner.

The potential of the developed acoustic tools was demonstrated in a number of parameter studies on MRI scanner models with different bore geometries and different loading conditions. In these studies, the structural composition of the gradient coil system was varied, in order to find a gradient coil system which minimizes the noise production of the MRI scanner.

The parameter studies revealed that the radiated sound power and the sound pressure level in the MRI bore respond similarly to design changes, in contrast to the velocity level. This means that the radiated power is an appropriate design objective function, because it is directly related to the noise that is experienced. Additionally, it enables the use of the radiation modes reduction technique. The studies show that the structural composition of the optimal gradient coil system depends on the shape of the MRI bore. This means that different gradient coil system designs should be used for MRI scanners with a different bore shape.

Optimum gradient coil system designs are characterized by a mismatch between peaks in the vibration level spectrum and near cut-on resonances. This characteristic is observed both for excitations with only a single and for excitations with multiple circumferential Fourier harmonics. However, with an increasing number of these Fourier harmonics, the number of velocity level peaks and the number of near cut-on resonances also increases. Therefore, the mismatch between vibration level peaks and cut-on resonances will be harder to achieve. This results in a smoothening of the noise spectra and a smaller range between optimal and 'worst-case' acoustic designs when the excitation contains more circumferential Fourier harmonics. Nevertheless, this range is still very significant for the design.

The preliminary design studies showed that the developed acoustic tools combined with the structural tools of Kessels [1999] enable a relatively easy and low-cost evaluation of the influence of design changes on the acoustic radiation of MRI scanners. This makes the use of these kinds of acoustic tools in an industrial design environment for MRI scanners or other axisymmetric structures viable.

# Samenvatting

Een MRI-scanner is een medisch diagnostisch apparaat waarmee, op basis van het fysisch principe van kernspinresonantie, afbeeldingen kunnen worden gemaakt van de interne structuren in het menselijk lichaam. Een bekend probleem bij MRI scanners is hun hoge geluidproductie (in de orde $90-120$ dB(A)) tijdens het scanproces. Het geluid wordt veroorzaakt door sterke trillingen in de zogenaamde gradiëntspoelen. Door nieuwe, snellere scantechnieken zal dit geluidsprobleem naar verwachting in de toekomst alleen maar groter worden. In het belang van patiënten, bedienend personeel en de bij een MRI onderzoek direct betrokken medische staf, is het nodig om in toekomstige scanners het geluid aanzienlijk te reduceren. Daarom is het noodzakelijk om tijdens het ontwerp van de scanner reeds de geluidsproductie te kunnen beoordelen om te trachten tot een geluidsarme MRI scanner te komen.

Het geluidsprobleem van MRI scanners kan modelmatig worden opgedeeld in twee stukken: een mechanisch en een akoestisch deel. Het mechanisch deel betreft de opwekking van mechanische trillingen door Lorentzkrachten. Het akoestische gedeelte beschrijft de omzetting van mechanische trillingen in geluid. Dit proefschrift handelt alleen over modellen voor het akoestisch deelprobleem, terwijl het proefschrift van Kessels [1999] gaat over het mechanisch deelprobleem en over mechanisch-akoestisch optimaliseren van MRI scanners.

Een adequaat akoestisch model voor het ontwerp van MRI scanners moet voldoen aan twee eisen. Het model moet enerzijds de voor het geluidsprobleem relevante aspecten van een MRI scanner bevatten en anderzijds praktisch hanteerbaar zijn voor de ontwikkelaars van MRI scanners. Het doel van dit promotieproject is daarom tweeledig. Het onderzoek is zowel gericht op de ontwikkeling van betrouwbare en efficiënte rekenmethoden om het geluidsprobleem van een MRI scanner te kunnen modeleren, als op de bestudering van akoestisch relevante invloedsfactoren in een ontwerp van een stillere MRI scanner.

Ten behoeve van het eerste deel van de doelstelling, de ontwikkeling van nauwkeurige en efficiënte rekenmethoden, zijn drie akoestische formuleringen ontwikkeld om het geluidsprobleem van bij benadering axisymmetrische MRI scanners te kunnen modeleren:

- Een semi-analytische methode voor de geluidsafstraling van een eindige pijp met open uiteinden waaraan oneindig grote flenzen zijn bevestigd.
- Een akoestische randelementenmethode met Fourier-elementen (Fourier BEM).
- Een modale beschrijving van de akoestiek op basis van de zogenaamde afstraalmodes.

De semi-analytische methode is ontwikkeld om inzicht te verschaffen in de fysica van dit specifieke geluidsprobleem. Deze methode is afgeleid binnen de algemene lineaire theorie van kanaalakoestiek. Er wordt uitgegaan van een beschrijving van het geluidsveld in een

korte pijp met oneindige flenzen, met behulp van Fourier-Bessel basisfuncties. De reflectie van geluidsgolven bij de uiteinden van de pijp wordt in rekening gebracht door middel van reflectiecoëfficiënten. Het gebruik van speciale integratietechnieken maakt de methode een stuk efficiënter dan discretisatie methoden gebaseerd op elementenformuleringen. Daarnaast biedt de methode meer fysisch inzicht in de specifieke akoestische eigenschappen van eindige pijpvormige constructies. Een beperking van dit model is echter dat het slechts bruikbaar is voor scanners met een sterk vereenvoudigde geometrie, waarbij de dwarsdoorsnede van de MRI-tunnel ('bore') constant moet zijn. Daarom is dit model eigenlijk alleen geschikt voor verkennende ontwerpstudies naar algemene invloedsfactoren, en niet voor detailstudies van MRI scanners met een meer realistische geometrie.

Het akoestische BEM model met Fourier-elementen maakt het mogelijk om de akoestiek te modelleren van axisymmetrische constructies in het algemeen en MRI scanners met een meer realistische geometrie in het bijzonder. Ten opzichte van akoestische berekeningen met een 3-dimensionale BEM formulering, worden met deze zogenaamde Fourier BEM formulering de rekentijden teruggebracht van enkele weken tot een klein uur. Daartoe wordt uitgegaan van een axisymmetrische (scanner) geometrie en worden de akoestische variabelen in omtreksrichting beschreven met een Fourier-reeks. Effectief wordt daarmee het 3-dimensionale akoestische afstralingsprobleem opgesplitst in een aantal 'quasi-axisymmetrische' afstralingsproblemen; één voor iedere Fourier-component in de reeks-ontwikkeling.

De innovatie van de Fourier BEM formulering die in dit proefschrift wordt beschreven zit hem in de manier waarop de Fourier-integralen in de formulering worden bepaald. Traditioneel gebeurt dit afzonderlijk voor elke Fourier-component in de reeksontwikkelingen, wat lange rekentijden oplevert. Door gebruik te maken van zogenaamde 'fast Fourier transform' (FFT) algoritmen, kunnen deze integralen simultaan worden bepaald, wat een enorme rekentijdreductie kan opleveren. Deze reductie is vooral merkbaar wanneer de Fourier-reeksen veel termen bevatten.

De beschrijving met akoestische afstraalmodes geeft aan welke componenten van het trillingsveld het meest bijdragen aan de geluidsvermogenproductie. Door een eigenwaarde-analyse toe te passen op de zogenaamde vermogenskoppelingsmatrix vindt men de af-straalmodes met bijbehorende afstraalefficiënties. Daarmee kan het totale trillingsveld worden onderverdeeld in componenten die goed afstralen en componenten die slecht afstralen. De afstraalmodes en -efficiënties hangen alleen af van de frequentie en de geometrie van het afstralende oppervlak, en dus niet van de mechanische eigenschappen van de straler.

Ontwerpwijzigingen aan een belangrijke klasse van constructieparameters (b.v. materiaal-eigenschappen, ophanging of belasting) veranderen alleen de randvoorwaarden van het akoestische probleem en niet de geometrie van het akoestische domein. Deze constatering is gebruikt in een modelreductietechniek gebaseerd op de afstraalmodesformulering. Met deze techniek is in een ontwerpstudie slechts één volledige akoestische analyse nodig per geometrie. In daaropvolgende akoestische analyses kunnen de resultaten van de eerste analyse worden hergebruikt. De totale rekentijd voor alle akoestische analyses tezamen kan daarmee drastisch worden gereduceerd. Dit is bij optimaliseringsstudies een bijzonder belangrijk voordeel.

Voor het tweede deel van de doelstelling van het promotieproject, het onderzoek naar akoestische invloedsfactoren voor het MRI scanner ontwerp, zijn de drie ontwikkelde re-

kenmethodes ingezet voor een aantal verkennende ontwerpstudies. Allereerst is als grove benadering de MRI scanner gemodelleerd als een korte pijp met oneindige flenzen aan de open uiteinden. Uit deze studie, die verricht is met behulp van de semi-analytische beschrijving, is gebleken dat de akoestiek van dit sterk gesimplificeerde MRI model wordt gedomineerd door zogenaamde 'nabij-cut-on' resonanties. Deze resonanties worden veroorzaakt door een hoge zelfreflectiecoefficiënt van een Fourier-Bessel mode van de pijp vlak boven de 'cut-on' frequentie van die mode. Door deze reflectie wordt een groot deel van een uitgaande Fourier-Bessel mode gereflecteerd in de pijp. Als nu de fase van heen- en teruggaande golven goed aansluiten, dan treedt er resonantie op. Dit veroorzaakt pieken in de frequentiespectra van de niveau's van zowel het geluidsvermogen, als de geluidsdruk en de afstraalefficiëntie.

De geometrie van de MRI-tunnel blijkt een belangrijke invloedsfactor voor het ontwerp. Als, met behulp van de Fourier BEM beschrijving, MRI scanners met een meer realistische geometrie worden gemodelleerd, verminderen de pieken in de frequentiespectra van geluidsafstraling die worden veroorzaakt door de 'nabij-cut-on' resonanties. Dit komt door de geleidelijk groter wordende dwarsdoorsnede van een meer realistische MRI-tunnel, waardoor de impedantiesprong aan de tunneluiteinden minder abrupt wordt. Dit heeft tot gevolg dat de zelfreflectiecoefficiënten minder groot zijn en het resonantieverschijnsel kleiner wordt. Daarbij bepaalt de binnendiameter van het deel van de tunnel met een constante dwarsdoorsnede de ligging van de 'cut-on' frequenties. De invloed van de buitendiameter van de scanner op de afstraling blijkt verwaarloosbaar klein te zijn.

Een andere invloedsfactor voor het MRI ontwerp is de aanwezigheid van een patiënt in de scanner. De invloed van een positie van de patiënt in de scanner en de invloed van geluidsabsorptie van kleding van de patiënt op de afstraling van de scanner is onderzocht met behulp van de Fourier BEM techniek. De positie van de patiënt in de scanner heeft vooral invloed op de ligging van de 'cut-on' frequenties. Dit effect wordt echter ten dele teniet gedaan door de absorptie van kleding van de patiënt op te voeren. Uit het onderzoek blijkt dat de invloed van de patiënt op het uiteindelijke geluidsniveau dusdanig gering is, dat het onnodig is om hier rekening mee te houden in het ontwerp van de MRI scanner.

De kracht van het ontwikkelde akoestisch rekengereedschap wordt verder gedemonstreerd in een aantal parameterstudies aan MRI scanners met een verschillende tunnelgeometrie en verschillende krachtsaanstoting. In deze ontwerpstudies werd de mechanische configuratie van de gradiëntspoelen gevarieerd en werd gezocht naar een gradiëntspoelconstructie die de geluidproductie van de scanner minimaliseert. Uit deze parameterstudies is gebleken dat het afgestraalde geluidsvermogen en de geluidsdruk in de MRI-tunnel hetzelfde reageren op ontwerpwijzigingen, in tegenstelling tot het snelheidsniveau aan de wand. Dit betekent dat een beoordeling van de geluidsproductie van een MRI ontwerp het beste kan gebeuren aan de hand van het geluidsvermogen aangezien dit een directe maat is voor de hinderbepalende geluidsproductie en doordat het gebruik van deze maat de toepassing van de modelreductietechniek op basis van afstraalmodes mogelijk maakt. Daarnaast blijkt dat de configuratie van de optimale gradiëntspoel afhangt van de vorm van de MRI-tunnel. Dit betekent dat bij elk MRI scanner ontwerp met een verschillende tunnelgeometrie ook een andere optimale gradiëntspoelconfiguratie hoort.

Kenmerkend voor de optimale gradiëntspoelconfiguraties is het feit dat voor die scanners de pieken in het trillingsspectrum op een zodanige plaats liggen dat ze de 'nabij-cut-on' re-

sonanties zo weinig mogelijk aanstoten. Dit geldt voor krachtsaanstotingen met zowel een enkele als met meerdere Fourier-componenten in omtreksrichting. Maar door toename van het aantal Fourier-componenten in de aanstoting neemt ook het aantal mechanische en mogelijke 'nabij-cut-on' resonanties toe. Daardoor is het moeilijker om aanstoting van de 'nabij-cut-on' resonanties door pieken in het trillingsspectrum te voorkomen. Dit resulteert in gladdere akoestische spectra en een kleinere spreiding tussen akoestisch optimale en akoestisch slechte ontwerpen als er meerdere Fourier-componenten in de aanstoting zitten. Desondanks blijft deze spreiding nog zeer relevant voor het ontwerp.

De verkennende studies naar de invloedsfactoren hebben aangetoond dat de ontwikkelde rekenmethoden in combinatie met de mechanische modellen van Kessels [1999] het mogelijk maken om op relatief eenvoudige en goedkope wijze de invloed van ontwerpwijzigingen op de akoestische afstraling van MRI scanners te bepalen. Dit maakt de inzet van dit soort rekengereedschappen in een industriële ontwerpomgeving voor MRI scanners of andere axisymmetrische constructies haalbaar.

# Notation

## General notation

| | |
|---|---|
| $A,\ a,\ \alpha$ | scalar (italic Latin and Greek symbols) |
| A, a | constant; standard function (upright Latin symbols) |
| $\boldsymbol{a},\ \boldsymbol{\alpha}$ | vector; column (bold italic Latin and Greek lowercase letters) |
| $\boldsymbol{A},\ \boldsymbol{\Gamma}$ | tensor; matrix (bold italic Latin and Greek capitals) |

## Operators and functions

| | |
|---|---|
| $a^*$ | complex conjugate of $a$ |
| Re $a$ | real part of $a$ |
| Im $a$ | imaginary part of $a$ |
| $|a|$ | absolute value of $a$ |
| $|\boldsymbol{a}|$ | length of vector $\boldsymbol{a}$ |
| $\bar{a}$ | time average of $a$ |
| $\langle a \rangle$ | spatial average of $a$ |
| $\mathrm{d}a/\mathrm{d}r$ | total derivative of $a$ with respect to $r$ |
| $\partial a/\partial r$ | partial derivative of $a$ with respect to $r$ |
| $\boldsymbol{A}^{-1}$ | inverse of $\boldsymbol{A}$ |
| $\boldsymbol{A}^{\mathsf{T}}$ | transpose of $\boldsymbol{A}$ |
| $\boldsymbol{A}^{\mathsf{H}}$ | hermitian (complex conjugate transpose) of $\boldsymbol{A}$ |
| $\boldsymbol{a} \cdot \boldsymbol{b}$ | inner product between vectors $\boldsymbol{a}$ and $\boldsymbol{b}$ |
| $\nabla a$ | gradient operator on $a$ |
| $\delta(a)$ | Dirac function on argument $a$ |
| $\delta_{ij}$ | Kronecker delta $(i, j)$ |
| $\mathrm{J}_m$ | Bessel function of the first kind of order $m$ |
| $\mathrm{I}_m$ | modified Bessel function of the first kind of order $m$ |
| $\mathrm{Y}_m$ | Bessel function of the second kind of order $m$ |
| $\mathrm{K}_m$ | modified Bessel function of the second kind of order $m$ |
| $\mathrm{H}_m^{(1)},\ \mathrm{H}_m^{(2)}$ | Hankel functions of the first and second kind of order $m$ |

## Latin symbols

| | | |
|---|---|---|
| $a$ | L | inner radius |
| $A$ | L | outer radius |
| $c_0$ | $\mathrm{L\,T^{-1}}$ | sound velocity in air |
| $c_o$ | — | oscillation parameter |

| | | |
|---|---|---|
| $c_s$ | — | steepness parameter |
| $\mathbf{e}_r, \mathbf{e}_\theta, \mathbf{e}_z$ | — | radial, circumferential and axial unit basis vectors in a cylindrical coordinate system |
| $f$ | $T^{-1}$ | frequency |
| $f_{m\mu}$ | $T^{-1}$ | cut-on frequency of Fourier-Bessel duct mode $(m, \mu)$ |
| $G(\mathbf{x}, \mathbf{y})$ | $L^{-1}$ | free space Green's function of points $\mathbf{x}$ and $\mathbf{y}$ |
| $J$ | — | Jacobian |
| $k$ | $L^{-1}$ | free field acoustic wavenumber |
| $k_{m\mu}$ | $L^{-1}$ | axial wavenumber of Fourier Bessel duct mode $(m, \mu)$ |
| $L$ | $L$ | duct half length |
| $L$ | — | axisymmetric body generator |
| $L_v$ | — | velocity level |
| $L_W$ | — | sound power level |
| $L_p$ | — | sound pressure level |
| $m$ | — | circumferential Fourier harmonic number |
| $\mathbf{n}$ | — | surface normal vector inward the acoustic medium |
| $p$ | $M\,T^{-2}\,L^{-1}$ | acoustic pressure |
| $P$ | $M\,L^2\,T^{-3}$ | sound power |
| $Q$ | $L^3\,T^{-1}$ | volume source strength |
| $r$ | $L$ | radial coordinate |
| $S$ | $L^2$ | surface |
| $t$ | $L$ | thickness |
| $\mathbf{u}$ | $L\,T^{-1}$ | velocity vector |
| $u_r$ | $L\,T^{-1}$ | radial component of velocity |
| $u_\theta$ | $L\,T^{-1}$ | circumferential component of velocity |
| $u_z$ | $L\,T^{-1}$ | axial component of velocity |
| $v$ | $L\,T^{-1}$ | surface normal velocity |
| $V$ | $L^3$ | volume |
| $z$ | $L$ | axial coordinate |
| $z_0$ | $M\,L^{-2}\,T^{-1}$ | specific impedance of air |
| $z_p$ | $M\,L^{-2}\,T^{-1}$ | specific impedance of patient |

## Greek symbols

| | | |
|---|---|---|
| $\alpha$ | — | absorption coefficient |
| $\alpha_{m\mu}$ | $L^{-1}$ | radial wavenumber of duct mode $(m, \mu)$ |
| $\zeta$ | — | modal contribution coefficient |
| $\eta$ | $L\,T^{-1}$ | normal velocity boundary condition |
| $\theta$ | — | circumferential coordinate |
| $\lambda$ | — | eigenvalue |
| $\mu$ | — | radial order of incident duct mode |
| $\nu$ | — | radial order of reflected duct mode |
| $\phi$ | — | basis function |
| $\xi$ | $L$ | local element coordinate |
| $\rho$ | $M\,L^{-3}$ | density |
| $\sigma$ | — | radiation efficiency |
| $\psi$ | $L\,T^{-1}$ | radiation mode |

| $\omega$ | $T^{-1}$ | angular frequency |
|---|---|---|

## Constants

| i | imaginary unit |
|---|---|
| e | natural logarithmic base |
| $\pi$ | circumference to diameter ratio of a circle |

# 1 Introduction

## 1.1 Motivation

Acoustic engineers today are challenged to apply numerical tools to analyze the acoustics of vibrating structures. The use of these tools is becoming increasingly widespread. However, the demands of the acoustic engineers are not yet completely fulfilled. The performance of computer hardware and software is not sufficient to make full acoustic analyses of large complex structures feasible. This became apparent when dealing with the acoustic design of a Magnetic Resonance Imaging (MRI) scanner.

*The MRI scanner*

A Magnetic Resonance Imaging (MRI) scanner (see figure 1.1) is a diagnostic device for medical imaging of the internal structures (soft tissues), flow and other physiological phenomena in the human body. The imaging process is based on nuclear magnetic resonance: when a static magnetic field is applied, the spins of the nuclei of atoms in the human body with an uneven number of protons are aligned and start to precess, i.e., spin around the magnetic field lines. The precession (or Larmor) frequency is linearly dependent on the magnetic field strength. The alignment causes a net longitudinal magnetization. For the imaging process, this alignment is disturbed by sending a radio frequent (RF) pulse which excites the nuclei and brings the spins in phase. The frequency of the pulse must be the same as the precession frequency. This phenomenon is called magnetic resonance and causes a spiraling transverse magnetization. When the RF signal is switched off, the spin axes of the nuclei will realign and dephase. This results in a decrease of transverse magnetization which can be measured. The amplitude of the measured signal depends on the tissue properties. The measured signals are processed to form an image. Spatial encoding of the imaging information is achieved by superimposing a gradient magnetic field on top of the static field which directly influences the precession frequency. Based on the frequency and phase information of the measured signals, the origin of the components of each signal can be deduced. A more detailed and mathematical description of the physical principles of magnetic resonance can be found in one of the many textbooks on this subject [e.g. Vlaardingerbroek and den Boer, 1996; Hashemi and Bradley, 1997].

A well known problem of MRI scanners is their large noise production during the imaging process [e.g. Hurwitz et al., 1989; Hedeen and Edelstein, 1997; Cho et al., 1998]. Both patient and operator are exposed to high noise levels (up to $90 - 120$ dB(A)), mainly caused by the vibration of the so-called gradient coil system (see figure 1.2). To understand this noise production mechanism it is important to look at an MRI scanner's construction. A strong uniform magnetic field ($0.1 - 1.5$ T) is produced by the (superconducting) static field magnet. On this field, a gradient magnetic field is dynamically superimposed which is

**figure 1.1** The MRI scanner in practice.

created by the so-called gradient coil magnets. The gradient coil support system consists of a number of layers with composite materials, in which the copper gradient coil wires are submerged. The coils are driven by a sequence of pulse-like currents of about 300 A in magnitude and with a frequency content mainly in the range of $100 - 2000$ Hz. Because of this switching current in the strong static magnetic field, dynamic Lorentz forces are generated in the gradient coils, which results in vibration of the coils' support system [e.g. Hurwitz et al., 1989; Kessels, 1999]. This vibration causes direct sound radiation at the surface of the gradient coil system. Indirectly, acoustical energy is transported through the coils' supports to the remainder of the scanner and magnetically to the superconducting magnet housing [Kooyman et al., 1993].



□ static field magnet
■ gradient coil system
■ RF transceiver
■ patient support

1m
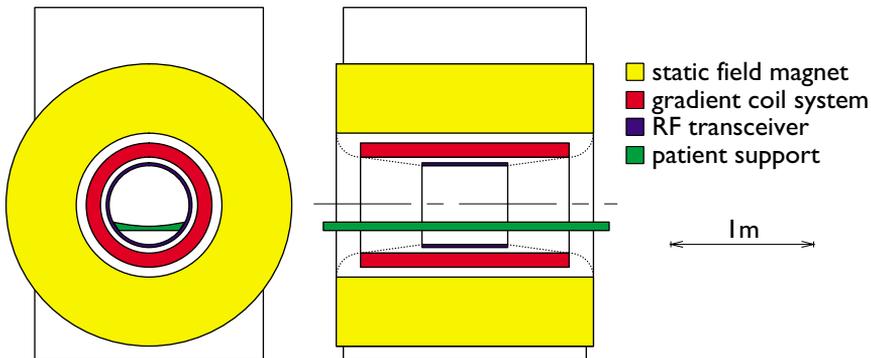
**figure 1.2** Schematic frontal and cross-sectional view of an MRI scanner.

*The noise problem in practice*

Under normal operating conditions, an MRI scanner is located in a hospital's radiology department. The scanner is installed in a separate room (scanner room) and the MRI scanner's operator is normally in a room adjacent to the scanner room (operator room). The operator maintains visual contact with the patient and the scanner through a window, and auditive contact through an intercom system.

For a diagnostic session with the MRI scanner, the patient is placed inside the bore (i.e. scanning section) of the scanner, after which the operator leaves the room and controls the scanning process in the operator room. A diagnostic session takes, on average, about 30 minutes. Under these operating conditions, the acoustic load on patients is rather high, as their position is very close to the noise source: the gradient coil system. It is therefore common practice to use some kind of active or passive hearing protection for a patient in the scanner to reduce the acoustic load on the ears [e.g. Goldman et al., 1989]. The operator experiences substantially less noise than the patient, but is subject to these levels much longer during a working day. However, ear protection is not necessary.

In the (near) future, it is expected that these operating conditions will change dramatically. New techniques are being developed to enable the use of surgical intervention techniques during the scanning process. These new developments require the presence of both the scanner's operator and a team of physicians and assistants inside the scanner room. In this way, those people are also more frequently subject to high noise levels. A complicating factor is the fact that surgical intervention techniques require fast scanning sequences, which result in an even higher noise load. Because of these changing operating conditions, it is insufficient to improve the acoustic treatment of the room and the hearing protection of the patient. The acoustic problem should be handled at the source itself.

*Research project background*

Direct motivation of this research project stems from the cooperation between Philips Medical Systems (PMS) and the TNO institute of Applied Physics. TNO performed a number of acoustical investigations for PMS to reduce the noise problem. They found that the major contribution to the total noise production of the MRI scanner is due to the gradient coil system vibrations [Kooyman et al., 1993; Kooyman, 1994] and that any attempt to achieve a substantial decrease of the noise production should focus first on the contribution of the gradient coil system to the total sound production. But fundamental knowledge and practical tools were lacking to accurately model the vibrations and acoustics of the gradient coil system. In a joint effort between PMS, the Dutch Technology Foundation (STW) and the Eindhoven University of Technology (TUE), a research program was started to develop the tools that were lacking. With these tools, the fundamental and practical knowledge of the structural-acoustic behavior of the gradient coil system can be obtained. Moreover, it was anticipated that these tools and knowledge for the MRI design could also be deployed for the analysis and design of other complex axisymmetric structures.

*Problem description*

Any structural-acoustic noise problem consists, as the name suggests, of two parts: a structural part and an acoustic part. The structural part describes how a force excitation, via the structural dynamics behavior of a system will induce vibrations. The acoustic part
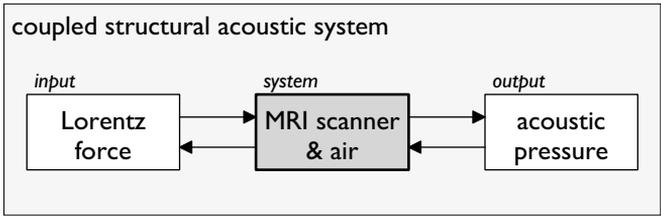
**figure 1.3** Coupled structural-acoustic MRI noise problem.

describes how these vibrations result in audible noise. Often, these parts are integrated, for instance if the generated acoustic pressure field excites the structure. For the MRI scanner this would yield a model as depicted in figure 1.3. However, the mass and stiffness of the gradient coil system prevent it from being excited significantly by the acoustic field. Therefore, the structural and acoustic domains in the noise problem can be separately solved (see figure 1.4). This thesis focuses on the acoustic part of the MRI noise problem, in particular the acoustic radiation of the gradient coil system. This means that the vibrations of the system are assumed to be known and the noise production is the quantity of interest. In a companion doctoral thesis, Kessels [1999] covers the development of structural dynamics tools and models for the MRI noise problem, and structural-acoustic optimization techniques.

It is recognized that a substantial decrease of the noise production of the scanner can only be achieved by explicitly incorporating studies of the acoustic behavior of the gradient coil system into the design phase [e.g. Ling et al., 1995]. However, the acoustic analysis of an MRI scanner is far from straightforward because of its large dimensions (typically outer diameter 2 m) combined with the broad frequency band of excitation ($100 - 2000$ Hz). Modeling such medium frequency problems with modern numerical acoustics tools [e.g. Sysnoise, 1996] would require an enormous amount of computational effort. With today's computer power this would result in simulation times in the order of weeks, which is infeasible in an industrial research and development environment. Moreover, one such an analysis would not directly provide the engineers with enough insight to construct
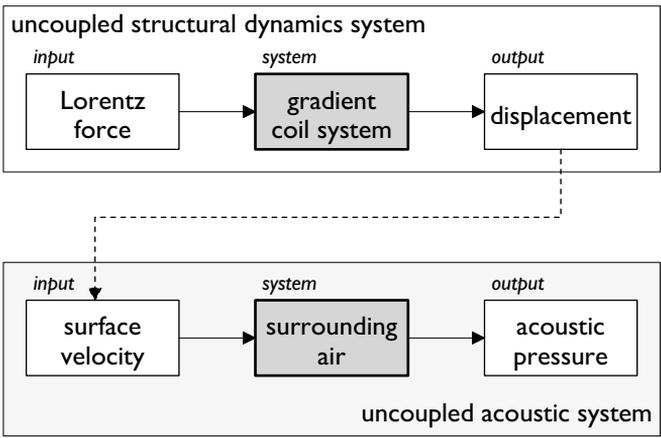


**figure 1.4** Decoupled structural-acoustic MRI noise problem.

a quieter MRI scanner. Likely, more analyses are required to gain some insight into the influence of different design parameters on the sound production. This would augment the computational costs even more.

## 1.2   Objective and strategy

The objective of this thesis is twofold. Firstly, it presents efficient computational methods to analyze the acoustic radiation of (nearly) axisymmetric structures. These methods can be used to predict the sound radiation of MRI scanners. Secondly, it considers the application of these formulations and it presents a systematic approach of how to use these models to analyze noise abatement measures in the design of MRI scanners.

The research strategy that is followed here to achieve the objective is first to develop accurate and efficient models that mathematically describe the radiation characteristics of the MRI scanner. Then, with these models, the typical radiation phenomena that occur in (finite) ducts will be studied. The knowledge gained will then be used to assess the importance of various modeling aspects that might influence the acoustic behavior of the scanner. These assessment studies will demonstrate the capabilities of the developed acoustic tools in the design process of the MRI scanner.

## 1.3   Acoustic modeling considerations

The development of an acoustic model for low-noise design of MRI scanners begins with the choice of the mathematical method that is used to describe the acoustic response due to mechanical vibrations. To be able to effectively use an acoustic model in a design environment, the model should be usable for non-trivial geometries and boundary conditions, its implementation should be efficient, and whenever possible, it should provide some insight into the radiation characteristics of the structure. These model characteristics often largely depend on the acoustic modeling and analysis method that is chosen.

Today, there exists a wide variety of acoustic modeling techniques that could be used for the acoustic analysis of vibrating axisymmetric structures and it is impossible or even undesirable to choose a single one of these methods and mark it as the best method to analyze the radiation of the MRI scanner. It is however possible to sketch the considerations that have lead to the choice of models that were used in this research. This is a process of 'wandering' down a tree-like hierarchical structure of acoustic modeling techniques (see figure 1.5) and at every node a comparison of methods can be made, weighing their benefits and short-comings in the light of the acoustic design of MRI scanners.

As a first step to construct a hierarchy of acoustic methods, one can discriminate between deterministic models (analytical or discretization methods) and stochastic methods (e.g. statistical energy analysis). The deterministic models try to provide an exact local prediction of the acoustic variables based on local input information. In contrast, the stochastic methods try to relate noise production to global variables like energy flows in acoustic systems, and are valid for ensembles of systems with similar but slightly varying properties.

A parameter that can be used to choose between these two modeling methods is the Helmholtz number $ka$, with $k = 2\pi f/c_0$ being the free field wavenumber, with frequency $f$ and sound speed $c_0$, and with $a$ as a characteristic dimension of the radiator. For low
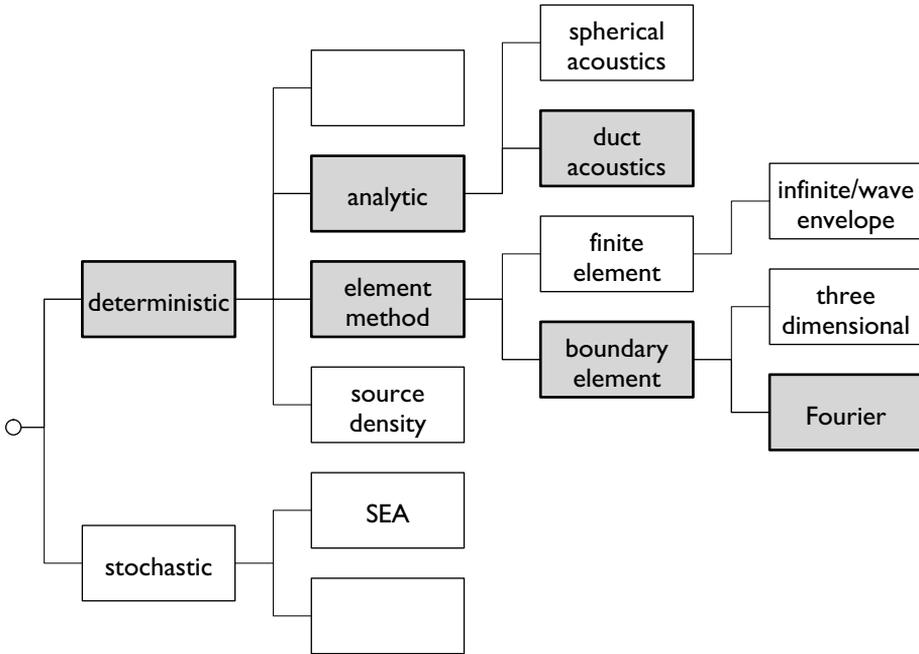
**figure 1.5** A hierarchy of mathematical acoustic modeling techniques. The grey boxes represent the modeling techniques that are treated in this thesis.

Helmholtz numbers, where distinct structural modes normally govern the structural dynamics, the deterministic methods can be used to give detailed information on the radiation characteristics. For efficiency reasons and because of modeling uncertainties, stochastic methods are used in the high Helmholtz number range. The location of the boundary between these ranges is unclear and tends to increase with increasing computer hardware power. However, applications of deterministic formulations are rarely seen above $ka = 10$.

The choice here for an analysis method to obtain an accurate and efficient acoustic model for the MRI scanner is determined by the scanner's geometry and the frequency range of acoustic excitation. With a scanner inner radius of $a = 0.35$ m and an excitation frequency range of $100 - 2000$ Hz, this results in a Helmholtz number range of $0 - 13$. Because of the low Helmholtz numbers and relatively small modal overlap between the structural modes, the use of stochastic methods like statistical energy analysis (SEA) is not the obvious choice. On the other hand, the maximum Helmholtz numbers suggest that deterministic methods will not be very computationally efficient to cover the complete frequency band.

To improve the efficiency of the deterministic models, the radiating parts of the scanner (i.e. the gradient coil system) and the MRI housing are assumed to be geometrically axisymmetric, as a first approximation. However, traditional axisymmetric models cannot be used because the force excitation and resulting vibrations of the scanner are essentially non-axisymmetric. This study will show that this problem can be handled elegantly with Fourier type models in which the circumferential dependency of the boundary conditions are described with Fourier series. This essentially decomposes the 3-dimensional radia-

tion problem into a series of 'quasi-axisymmetric' problems, each for a different Fourier harmonic in the excitation. The Fourier approach can be applied to both analytical and element based methods.

In the hierarchy of deterministic acoustic methods a choice must be made between analytical and element based formulations. An alternative to these formulations might be the recently introduced generalized internal source density method [Stepanishen, 1997], which was not studied here. Characteristic of the analytical models is that they are generally to be preferred over discretization methods because they better uncover the important radiation parameters of the acoustic model, yielding more physical insight. Besides that, they are normally more efficient. However, analytical solutions are generally only available for acoustic models with very simple geometries and boundary conditions. Therefore, for non-trivial geometries and boundary conditions, element based discretization methods like the boundary element method (BEM) or finite element method (FEM) are often the only option. To model the *external* acoustic radiation of vibrating structures, the BEM is to be preferred over FEM, because with the BEM, only the surface of the acoustic domain has to be discretized and not the whole acoustic domain. Moreover, the causality principle, leading to boundary conditions at infinity, is automatically satisfied. Note that a novel enhancement to the finite element method, referred to as the infinite element method or wave envelope element method, alleviates some of these disadvantages and broadens the application range of the finite element method.

For this thesis the Fourier approach has been chosen as a basis for both an analytical and boundary element based analysis method, the former to increase insight, the latter to handle more complex (realistic) MRI geometries. Furthermore, the efficacy of the boundary element based method was enhanced by applying the so-called radiation modes formulation. It will be shown that this formulation is helpful to acquire more understanding of the important radiation parameters which is difficult to obtain from the boundary element model alone. Also the radiation modes formulation will be shown to be usable as a model reduction technique.

## 1.4   Outline

This thesis can be split up into two parts: a part which covers the acoustic formulations for axisymmetric (duct-like) structures and a part which covers the application of these formulations for the acoustic design of the MRI scanner.

*Formulations*

In chapter 2, the first chapter in the modeling part, a (semi-)analytical formulation is presented to model the acoustic radiation of baffled finite ducts with vibrating walls. This formulation can be used to represent a rough approximation of an MRI scanner: it is axisymmetric, the outer radius is assumed to be infinite and the radius of the MRI bore (the scanning section) is constant. The resulting (semi-)analytical model offers understanding of some important acoustic phenomena that are typical of finite duct-like structures.

In chapter 3, a Fourier Boundary Element Method (Fourier BEM) formulation is presented. The Fourier BEM formulation is restricted to axisymmetric structures subject to general (non-axisymmetric) boundary conditions. For these structures, this formulation has a significantly better numerical efficiency than a 3-dimensional BEM formulation.

Chapter 4 deals with the radiation modes formulation. This formulation offers a modal approach for the analysis of exterior radiation characteristics of structures. It offers insight into the strongly radiating components of a structure's vibration field and also makes acoustic model reduction possible. This model reduction technique can be applied, irrespective of the underlying acoustic modeling technique. It can be exploited to its fullest extent in a design optimization environment.

*Applications*

Chapter 5 deals with some essential issues that need to be addressed before any of the developed numerical formulations can be used for the acoustic design of the MRI scanner. To quantify the noise production of the MRI scanner, an appropriate design objective function is chosen. Also, the application of the developed acoustic tools in different stages of the design process is illustrated.

In chapter 6, the versatile power of the developed numerical models is shown in some preliminary design studies for the MRI scanner. The influence of some important aspects of the acoustic MRI scanner model is addressed: the influence of the cut-on resonances, the excitation, the geometry of the scanner's casing, and the presence of a patient. The use of the models in parameter or optimization studies is also shown.

Finally, in chapter 7, the research presented in this thesis is discussed and conclusions are drawn upon the most important results. Also, recommendations are given on topics for future research and development activities for the acoustic design of MRI scanners.

# 2 A semi-analytical model for the radiation of baffled finite cylindrical ducts[*]

## 2.1 Introduction

An analytical model for the acoustic behavior of the MRI scanner and its gradient coil system must incorporate two aspects: the specific geometry of the scanner and its complex acoustic boundary conditions. As a first approximation, the geometry of the scanner can be modeled as being axisymmetric. Secondly, the boundary conditions can be approximated by assuming that only the inner wall of the gradient coil system can vibrate and thus radiate acoustic energy (see figure 1.2). But this is still too complex for an analytical acoustic model for the MRI scanner. Further model reduction can be achieved if the MRI scanner bore (central part with the gradient coil system) can be approximated as a finite cylindrical duct (constant cross-section) with infinite flanges. In this way, it is possible to use duct acoustics theory which receives considerable attention in the basic acoustic textbooks [Morse and Ingard, 1968; Skudrzyk, 1971; Pierce, 1981; Kinsler et al., 1982]. The theory presented in these books is, however, not sufficient to model the MRI scanner; it generally only deals with (semi-)infinite ducts with rigid walls or the plane wave approximation for the acoustic field inside the duct.

To the authors' knowledge, no studies have been reported in the literature dealing with the duct acoustics of a finite duct with vibrating walls. Models for the propagation and diffraction of sound inside semi-infinite and finite ducts, have been reported [e.g. Morfey, 1969; Doak, 1973; Zorumski, 1973; Wang and Tszeng, 1984; Hewlett et al., 1995] but they were mainly dealing with the radiation of (point) sources or propagation of sound inside hard-walled ducts, not including vibrating walls. Studies in the literature of the sound radiation of cylinders with vibrating walls [e.g. Sandman, 1976; Harari and Sandman, 1976; Filippi and Habault, 1989; Habault and Filippi, 1989; Grosh et al., 1994; Choi et al., 1996] all deal with external radiation. The results of these studies do not give a closed form solution to the internal radiation problem under consideration. Nevertheless, these models were useful as they provided the building blocks for an accurate and efficient acoustic model for the MRI scanner based on duct acoustics that will be presented here.

The model for the radiation of sound inside a baffled finite duct with vibrating walls, presented here, is an extension of the model presented by Doak [1973]. He modeled the radiation of sound by a distribution of sources inside a finite-length hard-walled duct with infinite flanges. This formulation was extended to handle vibrating walls inside the duct. The impedance boundary conditions in the duct at the flanges are handled by so-called

---

[*] This chapter was partly reproduced from Kuijpers et al. [1998a]

reflection coefficients [Zorumski, 1973]. In the model that will be presented here, which was first outlined by Rienstra [cf. Kuijpers et al., 1998a], special attention was paid to the computational efficiency of the model and therefore an alternative for the computation of these reflection coefficients was developed and implemented. The coupling between the reflection coefficients at the duct's exits and the sound field created in and propagated through the finite duct is expressed by two matrix equations that need to be solved simultaneously or iteratively.

## 2.2    Acoustics of finite cylindrical ducts with planar baffles

The acoustic model for a finite duct with vibrating walls and infinite flanges will be derived in this section. First, the general (infinite) duct acoustic theory, that is described in many textbooks [e.g. Morse and Ingard, 1968; Skudrzyk, 1971; Pierce, 1981], will be reviewed briefly. Then, step by step new features are introduced into the model, eventually leading to the desired model. First, a model will be derived that describes the acoustic response of the duct system due to a monopole source inside the duct wall. Then, it will be shown that the description of the acoustic field caused by the vibrating wall of the duct is a generalization of the monopole source model. At the end, the duct acoustics model incorporating wall vibration is coupled with a model for the reflection conditions for the baffle at the finite duct's exits. This results in a general model for the acoustics of finite cylindrical ducts with planar baffles and vibrating walls.

### 2.2.1    Acoustic equations for cylindrical ducts

Consider the sound field in an infinite cylindrical duct with radius $r = a$. If only harmonic solutions for the sound field are considered, the acoustic pressure $p$ and velocity $\boldsymbol{u}$ in the duct can be expressed as

$$\tilde{p}(r, \theta, z, t) = \text{Re}\left[p(r, \theta, z, \omega)e^{i\omega t}\right], \qquad \tilde{\boldsymbol{u}}(r, \theta, z, t) = \text{Re}\left[\boldsymbol{u}(r, \theta, z, \omega)e^{i\omega t}\right], \qquad (2.1)$$

with angular frequency $\omega$. This pressure field has to satisfy the continuity, momentum and state equations,

$$i\omega\rho + \rho_0 \boldsymbol{\nabla} \cdot \boldsymbol{u} = 0, \tag{2.2}$$

$$i\rho_0\omega\boldsymbol{u} + \boldsymbol{\nabla}p = 0, \tag{2.3}$$

$$p = \rho c_0^2, \tag{2.4}$$

with density $\rho$, speed of sound $c$, and the subscript $_0$ denoting the constant equilibrium quantity. These equations can be combined into the Helmholtz equation,

$$\nabla^2 p + k^2 p = 0, \tag{2.5}$$

with free field wavenumber $k = \omega/c_0$. The structure is also subject to a normal velocity boundary condition at the duct wall,

$$\boldsymbol{u}\big|_{\text{wall}} \cdot \boldsymbol{n} \equiv -u_r\big|_{r=a} = \eta(\theta, z), \tag{2.6}$$

with $\boldsymbol{n}$ the inward surface normal, $u_r$ the radial component of $\boldsymbol{u}$, $\eta$ the imposed duct wall velocity boundary condition, and the gradient and Laplace operators, respectively

$$\boldsymbol{\nabla} = \boldsymbol{e}_r\frac{\partial}{\partial r} + \boldsymbol{e}_\theta\frac{1}{r}\frac{\partial}{\partial \theta} + \boldsymbol{e}_z\frac{\partial}{\partial z}, \qquad \nabla^2 = \frac{\partial^2}{\partial r^2} + \frac{1}{r}\frac{\partial}{\partial r} + \frac{1}{r^2}\frac{\partial^2}{\partial \theta^2} + \frac{\partial^2}{\partial z^2}.$$

### 2.2.2  The acoustic field inside a hard-walled infinite duct

When the sound field in a hard-walled infinite duct ($\eta = 0$) is considered, the technique of separation of variables can be used. A solution of the kind $p = f(r)g(\theta)h(z)$ is assumed to satisfy the homogeneous Helmholtz equation (2.5). This solution exists if

$$\frac{\partial^2 f}{\partial r^2} + \frac{1}{r}\frac{\partial f}{\partial r} + (\alpha^2 - \frac{m^2}{r^2})f = 0, \tag{2.7a}$$

$$\frac{\partial^2 g}{\partial \theta^2} + m^2 g = 0, \tag{2.7b}$$

$$\frac{\partial^2 h}{\partial z^2} + (k^2 - \alpha^2)h = 0, \tag{2.7c}$$

so that $f(r) = J_m(\alpha_{m\mu}r)$, $\mu = 1, 2, \ldots$, where $J_m$ denotes the ordinary Bessel function of the first kind and $\alpha_{m\mu} = j'_{m\mu}/a$ the radial wavenumber, where $j'_{m\mu}$ is the $\mu$th nonnegative non-trivial zero of $J'_m$ (see appendix A). This solution satisfies the boundary condition at the duct wall: $df/dr|_{r=a} = 0$. The Bessel function of the second kind $Y_m$ is also a solution of equation (2.7a), but does not satisfy the condition at $r = 0$ where the pressure and its derivative should be finite. Also $g(\theta) = e^{-im\theta}$, $m = \ldots, -2, -1, 0, 1, 2, \ldots$, where use is made of the condition of continuity from $\theta = 2\pi$ to $\theta = 0$. Finally, $h(z) = e^{\mp ik_{m\mu}z}$, where $k_{m\mu} = \sqrt{(k^2 - \alpha_{m\mu}^2)}$ is the axial wavenumber, the square root being chosen such that $\mathrm{Re}(k_{m\mu}) \geq 0$ and $\mathrm{Im}(k_{m\mu}) \leq 0$. When at a certain free field wavenumber $k$, the axial wavenumber $k_{m\mu}$ is real, the function $h(z)$ is an oscillatory function, and the corresponding acoustic wave is called cut-on. If $k_{m\mu}$ is imaginary, the function $h(z)$ is exponentially decaying (in its propagation direction) and the associated wave is called cut-off (see appendix A).

The *modes*

$$p_{m\mu}^{\pm}(r, \theta, z) = J_m(\alpha_{m\mu}r)e^{-im\theta \mp ik_{m\mu}z} \tag{2.8}$$

form a complete basis [Watson, 1966] for the acoustic field in the duct (with the $+$ and $-$ superscript denoting a wave traveling in the positive or negative $z$-direction, respectively). Any field in the duct can thus be written by the principle of superposition as the following modal expansion:

$$p(r, \theta, z) = \sum_{m=-\infty}^{\infty}\sum_{\mu=1}^{\infty} J_m(\alpha_{m\mu}r)e^{-im\theta}(A_{m\mu}e^{-ik_{m\mu}z} + B_{m\mu}e^{ik_{m\mu}z}), \tag{2.9}$$

where the amplitudes $A_{m\mu}$ and $B_{m\mu}$ of the individual modes are determined by the boundary conditions. This modal expansion is the basis for general duct acoustics [e.g. Morse and Ingard, 1968; Skudrzyk, 1971; Pierce, 1981]. The plane wave is a special form of this general case with the $m = 0$, $\mu = 1$ mode only. In the following sections this modal expansion will be used to construct the acoustic field inside ducts with various boundary conditions.

### 2.2.3  Radiation from a point source in the wall of an infinite duct

Consider the field generated inside a hard-walled duct by a volume point source with strength $Q$ at location $\mathbf{x}_s = (r = r_s, \theta = \theta_s, z = z_s)$ defined by

$$i\omega\rho + \rho_0 \boldsymbol{\nabla} \cdot \boldsymbol{u} = \rho_0 Q\delta(\mathbf{x} - \mathbf{x}_s), \tag{2.10}$$
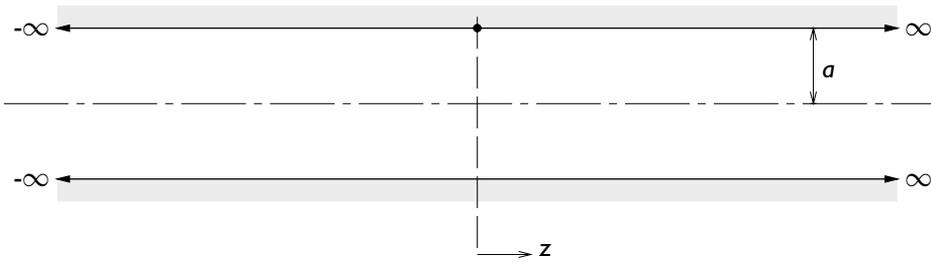
**figure 2.1** Acoustic source (•) at the wall of an infinite duct.

inside the duct (see figure 2.1). The source strength distribution is given by

$$Q\delta(\mathbf{x} - \mathbf{x}_s) = Q\delta(r - r_s)\delta(z - z_s)\frac{1}{r_s}\sum_{m=-\infty}^{\infty}\delta(\theta - 2\pi m - \theta_s). \tag{2.11}$$

From causality arguments the generated field should radiate away from the source. A Fourier transformation technique will now be applied to obtain a solution for the acoustic pressure and velocity field that are generated by the point source. When the source is located on the duct wall $r_s = a, \theta_s = 0, z_s = 0$, it can be represented elegantly by the (generalized Fourier transformed) boundary condition (2.6) at the duct wall:

$$\begin{aligned}
u_r\big|_{r=a} &= \frac{1}{-i\omega\rho_0}\frac{\partial p}{\partial r}\bigg|_{r=a} = \frac{-Q}{a}\delta(z)\sum_{m=-\infty}^{\infty}\delta(\theta - 2\pi m) \\
&= \frac{-Q}{a}\frac{1}{2\pi}\int_{-\infty}^{\infty}e^{-i\gamma z}d\gamma\frac{1}{2\pi}\sum_{m=-\infty}^{\infty}e^{-im\theta}.
\end{aligned} \tag{2.12}$$

The solution of the wave equation (2.5) can be found by Fourier transformation in $z$ and Fourier series expansion in $\theta$ of the pressure:

$$p(r, \theta, z) = \int_{-\infty}^{\infty}\sum_{m=-\infty}^{\infty}\hat{p}_m(r, \gamma)e^{-im\theta - i\gamma z}d\gamma, \tag{2.13}$$

$$\hat{p}_m(r, \gamma) = A_m(\gamma)J_m(\alpha(\gamma)r), \tag{2.14}$$

$$\alpha(\gamma)^2 = k^2 - \gamma^2. \tag{2.15}$$

Substituting the expression for the Fourier coefficients of the pressure equation (2.14) in the general expression for the boundary condition (2.12) at $r = a$, it follows that

$$\alpha A_m J'_m(\alpha a) = -\omega\rho_0 Q/a4\pi^2 i, \tag{2.16}$$

$$p(r, \theta, z) = \frac{-k\rho_0 c_0 Q}{4\pi^2 i}\sum_{m=-\infty}^{\infty}e^{-im\theta}\int_{-\infty}^{\infty}\frac{J_m(\alpha r)}{\alpha a J'_m(\alpha a)}e^{-i\gamma z}d\gamma. \tag{2.17}$$

The residue integration method [see e.g. Kreyszig, 1993, chap 15], is applied to compute the integral in equation (2.17). To satisfy causality, the integration contour is indented

above the poles $\gamma = k_{m\mu}$ and below the poles $\gamma = -k_{m\mu}$, and the contour closed through the lower half plane for positive $z$ and through the negative half plane for negative $z$ [see e.g. appendix B.1; Morse and Ingard, 1968, p.17; Skudrzyk, 1971, p.652]. The solution can be written as

$$p(r, \theta, z) = \frac{\rho_0 c_0}{2\pi} \sum_{m=-\infty}^{\infty} e^{-im\theta} \sum_{\mu=1}^{\infty} \frac{\alpha_{m\mu}^2 a^2}{\alpha_{m\mu}^2 a^2 - m^2} \frac{J_m(\alpha_{m\mu} r)}{J_m(\alpha_{m\mu} a)} \frac{kQ}{k_{m\mu} a^2} e^{-ik_{m\mu}|z|}, \qquad (2.18)$$

of which the plane wave component is

$$p(r, \theta, z) = \frac{\rho_0 c_0}{2\pi} \frac{Q}{a^2} e^{-ik_{m\mu}|z|}.$$

This result is an expression for the acoustic impulse response of the infinite duct valid for any non-resonant frequency ($k_{m\mu} \neq 0$). In the source plane $z = z_s = 0$, the series for $p$ is conditionally convergent. A series representation of the velocity $\mathbf{u}$ can be obtained by using equation (2.3). But, when trying to compute the actual velocity distribution with this series representation, one notes that the series is not convergent at all in the usual sense: it has to be interpreted as a generalized function, as might be expected from the $\delta$-type source.

Next, it will be shown that the Fourier transformation method, that is used here to obtain the pressure field that results from a point source on the duct wall, can also be used to obtain an expression for the pressure inside a duct with vibrating walls.

### 2.2.4 Radiation from a finite part of the wall inside an infinite duct

If a finite part (between $-L \leq z \leq L$) of the wall (at $r = a$) inside an infinite duct is vibrating and radiating sound (figure 2.2), the velocity at the wall can be described as

$$u_r(a, \theta, z) = -\eta(\theta, z) \ \text{ for } \ -L \leq z \leq L. \qquad (2.19)$$

For each frequency $\omega$, the solution of this problem can be found with the Fourier transformation method analogous to the method described for the simple source radiation. Again, from causality, the field should be radiating outward in the region $|z| > L$. The boundary condition at the duct wall can again be written as a Fourier sum:

$$
\begin{aligned}
u_r(r = a, \theta, z) &= -\frac{1}{i\omega\rho_0} \left. \frac{\partial p}{\partial r} \right|_{r=a} \\
&= -\frac{1}{2\pi} \sum_{m=-\infty}^{\infty} e^{-im\theta} \eta_m(z) \\
&= -\frac{1}{4\pi^2} \sum_{m=-\infty}^{\infty} e^{-im\theta} \int_{-\infty}^{\infty} \hat{\eta}_m(\gamma) e^{-i\gamma z} d\gamma,
\end{aligned}
\qquad (2.20)
$$

where the Fourier coefficients $\hat{\eta}_m(\gamma)$ of the wall velocity $\eta_m(\theta, z)$ are defined by

$$\hat{\eta}_m(\gamma) = \int_{-\infty}^{\infty} e^{i\gamma z} \int_0^{2\pi} \eta(\theta, z) e^{im\theta} d\theta dz = \int_{-L}^{L} \int_0^{2\pi} \eta(\theta, z) e^{im\theta + i\gamma z} d\theta dz. \qquad (2.21)$$
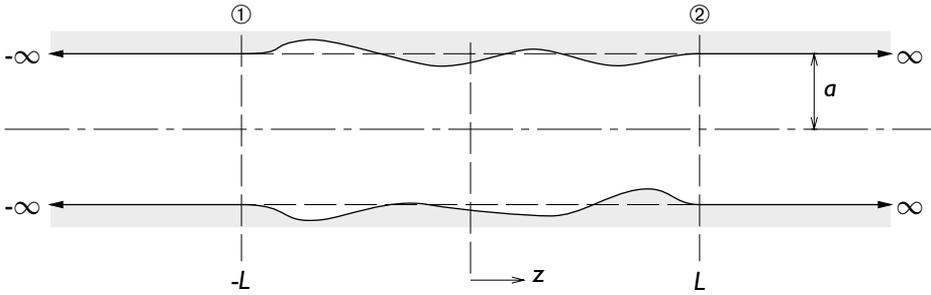
**figure 2.2** Vibrating walls inside an infinite duct.

For the pressure in the duct, the modal expansion from equations (2.13) – (2.15) can again be used here,

$$p(r, \theta, z) = \int\limits_{-\infty}^{\infty} \sum_{m=-\infty}^{\infty} \hat{p}_m(r, \gamma) e^{-im\theta - i\gamma z} d\gamma,$$

with

$$\hat{p}_m(r, \gamma) = A_m(\gamma) J_m(\alpha(\gamma) r), \qquad \alpha(\gamma)^2 = k^2 - \gamma^2.$$

Substituting this expansion in equation (2.20) for the boundary condition at the duct wall results in

$$\alpha A_m J'_m(\alpha a) = -\omega \rho_0 \hat{\eta}_m / 4\pi^2 i, \tag{2.22}$$

$$p(r, \theta, z) = -\frac{k\rho_0 c_0 a}{4\pi^2 i} \sum_{m=-\infty}^{\infty} e^{-im\theta} \int\limits_{-\infty}^{\infty} \frac{J_m(\alpha r)}{\alpha a J'_m(\alpha a)} \hat{\eta}_m(\gamma) e^{-i\gamma z} d\gamma$$

$$\tag{2.23}$$

$$= -\frac{k\rho_0 c_0 a}{4\pi^2 i} \sum_{m=-\infty}^{\infty} e^{-im\theta} \int\limits_{-L}^{L} \int\limits_{-\infty}^{\infty} \frac{J_m(\alpha r)}{\alpha a J'_m(\alpha a)} e^{-i\gamma(z-z')} d\gamma \, \eta_m(z') dz'.$$

Similar to the 'source in the hard-walled duct' case, the integral in this equation can be computed with the residue integration method, because $\hat{\eta}_m(\gamma)$ is analytic everywhere since it is defined as a finite integral. This results in

$$p(r, \theta, z) = \frac{\rho_0 c_0}{2\pi} \sum_{m=-\infty}^{\infty} e^{-im\theta} \sum_{\mu=1}^{\infty} \frac{\alpha_{m\mu}^2 a^2}{\alpha_{m\mu}^2 a^2 - m^2} \frac{J_m(\alpha_{m\mu} r)}{J_m(\alpha_{m\mu} a)} \frac{k}{k_{m\mu} a} \int\limits_{-L}^{L} \eta_m(z') e^{-ik_{m\mu}|z-z'|} dz',$$

$$\tag{2.24}$$

valid for any non-resonance frequency ($k_{m\mu} \neq 0$). This result denotes the convolution of the acoustic impulse response ,equation (2.18), and the circumferential Fourier coefficients of the wall velocity $\eta_m(z)$. A bit confusing may be the observation that the resulting series

for the radial velocity $u_r$,

$$u_r(r, \theta, z) = \frac{i}{2\pi} \sum_{m=-\infty}^{\infty} e^{-im\theta} \sum_{\mu=1}^{\infty} \frac{\alpha_{m\mu}^2 a^2}{\alpha_{m\mu}^2 a^2 - m^2} \frac{J'_m(\alpha_{m\mu}r)}{J_m(\alpha_{m\mu}a)} \frac{\alpha_{m\mu}}{k_{m\mu}a} \int_{-L}^{L} \eta_m(z') e^{-ik_{m\mu}|z-z'|} dz',$$

(2.25)

appears to be a sum of hard wall modes. Since every term in the radial velocity series vanishes at the wall (because $J'_m(\alpha_{m\mu}a) = 0$ by definition of $\alpha_{m\mu}$), it might *seem* that the series also vanishes at the wall, in contrast to the boundary condition! This is, however, only point wise, because the series does not converge uniformly near $r = a$ [see e.g. Kreyszig, 1993,chap. 14]. In any neighborhood of $r = a$, the series behaves according to the boundary condition. Furthermore, an order of magnitude estimate of the terms of the series shows that the series for $p$ converges absolutely, and for $u_r$ converges conditionally.

Next, it will be shown that the expression for the pressure in an infinite duct with partly vibrating walls can be extended to incorporate the effect of infinite flanges as duct terminations.

### 2.2.5 Radiation from a finite duct terminating in infinite flanges

The radiation from the walls of a finite duct terminating in rigid baffles (see figure 2.3) is considerably more complex than the former three situations. This is caused by the 'interface' impedances at the duct's exits. An acoustic wave that is incident to the plane of termination of the duct in a rigid baffle is partly transmitted and partly reflected. The reflection is rather complex because there generally is coupling between the radial modes of the incident and reflected acoustic field. Zorumski [1973] has described a method to compute the generalized radiation impedances and reflection coefficients of circular ducts. This is needed to impose the boundary conditions for the sound radiation model for baffled finite ducts. It will be shown that the model for the radiation of a vibrating wall in an infinite duct can be combined with the reflection coefficients to impose the boundary conditions at the duct's exits.

*Generalized radiation impedances*

Consider the radiation of sound from a cylindrical duct terminating in planar baffles (infinite flanges). The pressure and axial velocity at the duct's exits ($z = z_e = \pm L$, as in figure 2.3) can be written as a complete sum of duct modes in radial $r$ and circumferential $\theta$ direction:

$$p(r, \theta, z_e) = \sum_{m=-\infty}^{\infty} e^{-im\theta} \sum_{\mu=1}^{\infty} P_{m\mu} J_m(\alpha_{m\mu}r),$$

(2.26)

$$u_z(r, \theta, z_e) = \frac{1}{\rho_0 c_0} \sum_{m=-\infty}^{\infty} e^{-im\theta} \sum_{\mu=1}^{\infty} V_{m\mu} J_m(\alpha_{m\mu}r),$$

(2.27)

with modal coefficients $P_{m\mu}$ and $V_{m\mu}$ for the pressure and velocity, respectively. Zorumski [1973] has shown that, for $J'_m(\alpha_{m\mu}a) = 0$, these coefficients are coupled by so-called generalized radiation impedances (see appendix B.2)

$$P_{m\mu} = \sum_{\nu=1}^{\infty} Z_{m\mu\nu} V_{m\nu},$$

(2.28)
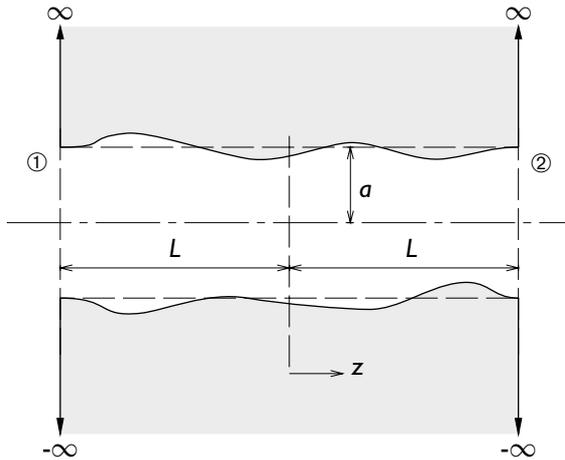
**figure 2.3** Vibrating walls inside a baffled finite duct.

where $\mu$ is the radial order of the incident mode, $\nu$ the radial order of the reflected mode, and

$$Z_{m\mu\nu} = \frac{1}{N^2_{m\mu}} \int_0^\infty \frac{\tau}{\sqrt{1-\tau^2}} D_{m\mu}(\tau) D_{m\nu}(\tau) \mathrm{d}\tau, \tag{2.29}$$

$$N^2_{m\mu} = \frac{1}{2}(a^2 - m^2/\alpha^2_{m\mu}) J_m(\alpha_{m\mu}a)^2, \tag{2.30}$$

$$D_{m\mu}(\tau) = \frac{\tau k^2 a}{\alpha^2_{m\mu} - \tau^2 k^2} J'_m(\tau ka) J_m(\alpha_{m\mu}a). \tag{2.31}$$

Equation (2.28) shows that energy from a single incident radial mode is transferred into all reflected (and transmitted) radial modes. Because of the oscillatory nature of the integrand in equation (2.29), the evaluation of this integral is not straightforward. This is discussed in appendix B.3.

*Accounting for planar baffles in a finite duct*

The problem of a vibrating duct wall that radiates sound into a finite duct terminating in planar baffles is an extension of the problem of a vibrating wall in an infinite duct. The baffle interface acts as an additional generalized impedance in the duct, where incident waves are partly transmitted and partly reflected. The total solution for the pressure has to satisfy both the boundary conditions at the duct wall and at the interface at the duct's exits. Since the boundary conditions at the wall are similar for the finite and infinite duct problems, it is convenient to use this solution (denoted as $p'$) and adding to this solution a homogeneous solution, i.e., a general duct acoustic pressure field $p''$ with vanishing velocity at the wall. This is possible because the equations are linear.

The pressure in the finite duct can be written as

$$p(r, \theta, z) = p'(r, \theta, z) + p''(r, \theta, z), \tag{2.32}$$

with

$$p'(r, \theta, z) = \frac{\rho_0 c_0}{2\pi} \sum_{m=-\infty}^{\infty} e^{-im\theta} \sum_{\mu=1}^{\infty} \frac{\alpha_{m\mu}^2 a^2}{\alpha_{m\mu}^2 a^2 - m^2} \frac{J_m(\alpha_{m\mu}r)}{J_m(\alpha_{m\mu}a)} \frac{k}{k_{m\mu}a} \int_{-L}^{L} \eta_m(z') e^{-ik_{m\mu}|z-z'|} dz',$$

(2.33)

$$p''(r, \theta, z) = \sum_{m=-\infty}^{\infty} e^{-im\theta} \sum_{\mu=1}^{\infty} J_m(\alpha_{m\mu}r)(A_{m\mu}'' e^{-ik_{m\mu}z} + B_{m\mu}'' e^{ik_{m\mu}z}), \qquad (2.34)$$

where $(\alpha_{m\mu}^2 a^2)/(\alpha_{m\mu}^2 a^2 - m^2) = 1$ if $m = 0$, $\mu = 1$. The total pressure $p$ has to satisfy the boundary condition

$$\frac{\partial p}{\partial r}\bigg|_{r=a} = \frac{\partial}{\partial r}(p' + p'')\bigg|_{r=a} = -i\omega\rho_0 u_r(r = a, \theta, z). \qquad (2.35)$$

The pressure field $p'$ already satisfies this boundary condition as defined in equation (2.20) thus for $p''$ the following boundary condition must hold:

$$\frac{\partial p''}{\partial r}\bigg|_{r=a} = 0. \qquad (2.36)$$

At first glance, it might seem that this condition is easily satisfied because every term in the series of $\partial p''/\partial r$ equals zero, because they all contain the portion $J_m'(\alpha_{m\mu}r)$ which equals zero for $r = a$. But the same holds for the series of $p'$ while for that series $\partial p'/\partial r \neq 0$, because the series does not converge uniformly. So, the fact that every term in the series for $\partial p''/\partial r$ equals zero, is not a sufficient condition to comply with equation (2.36). Therefore, an additional condition for $p''$ is necessary: the series sum for $\partial p''/\partial r$ should converge uniformly (which is the case for example if the series consists of a finite number of terms).

The uniform convergence condition for $p''$ is essential for the subdivision of $p$, but appears to be satisfied in practice. Hence, the sound field that is generated in the finite duct is a superposition of the sound field generated by the vibrating walls in an infinite duct and the homogeneous sound field satisfying the velocity boundary condition $u_r = 0$ at $r = a$. The modal coefficients $A_{m\mu}''$ and $B_{m\mu}''$ will be determined by the condition that the total solution has to satisfy the reflection boundary conditions at the duct's exits ($z = \pm L$). The total acoustic pressure can thus be written as

$$p(r, \theta, z) = \sum_{m=-\infty}^{\infty} \sum_{\mu=1}^{\infty} J_m(\alpha_{m\mu}r) e^{-im\theta} \left(A_{m\mu}(z)e^{-ik_{m\mu}z} + B_{m\mu}(z)e^{ik_{m\mu}z}\right), \qquad (2.37)$$

with

$$A_{m\mu}(z) = A_{m\mu}'' + \frac{\alpha_{m\mu}^2 a^2}{\alpha_{m\mu}^2 a^2 - m^2} \frac{1}{J_m(\alpha_{m\mu}a)} \frac{\rho_0 c_0 k}{2\pi a k_{m\mu}} \int_{-L}^{z} \eta_m(z') e^{ik_{m\mu}z'} dz', \qquad (2.38a)$$

$$B_{m\mu}(z) = B_{m\mu}'' + \frac{\alpha_{m\mu}^2 a^2}{\alpha_{m\mu}^2 a^2 - m^2} \frac{1}{J_m(\alpha_{m\mu}a)} \frac{\rho_0 c_0 k}{2\pi a k_{m\mu}} \int_{z}^{L} \eta_m(z') e^{-ik_{m\mu}z'} dz'. \qquad (2.38b)$$

At the interface, the generalized impedances defined in the previous section can be used to obtain a relationship between the modal coefficients of the pressure and velocity at the duct's exits. The value of the pressure, velocity and their modal coefficients at interfaces ① and ② in figure 2.3 are identified by superscripts ① and ②. At interface ①, $p'$ can be written as

$$p'(r, \theta, z = -L) = p'^{①} = \sum_{m=-\infty}^{\infty} \sum_{\mu=1}^{\infty} J_m(\alpha_{m\mu} r) e^{-im\theta} (H_{m\mu}^{①} e^{-ik_{m\mu} L}), \qquad (2.39)$$

with

$$H_{m\mu}^{①} = \frac{\alpha_{m\mu}^2 a^2}{\alpha_{m\mu}^2 a^2 - m^2} \frac{1}{J_m(\alpha_{m\mu} a)} \frac{\rho_0 c_0 k}{2\pi a k_{m\mu}} \int_{-L}^{L} \eta_m(z') e^{-ik_{m\mu} z'} dz'. \qquad (2.40)$$

Thus, the total pressure $p$ at interface ① is given by

$$p(r, \theta, z = -L) = p^{①} = \sum_{m=-\infty}^{\infty} \sum_{\mu=1}^{\infty} J_m(\alpha_{m\mu} r) e^{-im\theta} (A_{m\mu}'' e^{ik_{m\mu} L} + (H_{m\mu}^{①} + B_{m\mu}'') e^{-ik_{m\mu} L}).$$

$$(2.41)$$

The axial velocity $u_z(r, \theta, z)$ *in the negative z-direction* can be written as

$$u_z(r, \theta, z = -L) = u_z^{①} = \frac{1}{i\omega\rho_0} \frac{\partial p}{\partial z} \Big|_{z=-L}$$

$$= \sum_{m=-\infty}^{\infty} \sum_{\nu=1}^{\infty} J_m(\alpha_{m\nu} r) e^{-im\theta} \frac{k_{m\nu}}{\omega\rho_0} (A_{m\nu}'' e^{ik_{m\nu} L} - (H_{m\nu}^{①} + B_{m\nu}'') e^{-ik_{m\nu} L}). \quad (2.42)$$

The coefficients of the pressure and axial velocity at interface ① from equations (2.26) and (2.27), respectively, can be written as

$$P_{m\mu}^{①} = A_{m\mu}'' e^{ik_{m\mu} L} + (H_{m\mu}^{①} + B_{m\mu}'') e^{-ik_{m\mu} L}, \qquad (2.43)$$

$$V_{m\nu}^{①} = \frac{k_{m\nu}}{k} (-A_{m\nu}'' e^{ik_{m\nu} L} + (H_{m\nu}^{①} + B_{m\nu}'') e^{-ik_{m\nu} L}). \qquad (2.44)$$

These expressions can be substituted into equation (2.28) (which is allowed because the boundary conditions at the duct wall for $p'$ and $p''$ both satisfy $J'(\alpha_{m\mu} a) = 0$, although the series for $\partial p'/\partial r$ does not converge uniformly). This substitution gives

$$A_{m\mu}'' e^{ik_{m\mu} L} + (H_{m\mu}^{①} + B_{m\mu}'') e^{-ik_{m\mu} L} = \sum_{\nu=1}^{\infty} Z_{m\mu\nu}^{①} \frac{k_{m\nu}}{k} [(H_{m\nu}^{①} + B_{m\nu}'') e^{-ik_{m\nu} L} - A_{m\nu}'' e^{ik_{m\nu} L}],$$

$$(2.45)$$

or

$$\sum_{\nu=1}^{\infty} (Z_{m\mu\nu}^{①} \frac{k_{m\nu}}{k} + \delta_{\mu\nu}) A_{m\nu}'' e^{ik_{m\nu} L} = \sum_{\nu=1}^{\infty} (Z_{m\mu\nu}^{①} \frac{k_{m\nu}}{k} - \delta_{\mu\nu}) (H_{m\nu}^{①} + B_{m\nu}'') e^{-ik_{m\nu} L}. \qquad (2.46)$$

Upon introducing the variable

$$E_{m\nu}(z) = e^{-ik_{m\nu}z},$$ 
(2.47)

equation (2.46) can be written as

$$E_{m\mu}(-L)A''_{m\mu} = \sum_{\nu=1}^{\infty} R^{\text{①}}_{m\mu\nu}E_{m\nu}(L)(B''_{m\nu} + H^{\text{①}}_{m\nu}), \qquad \text{for} \quad \begin{aligned} &m = 0, \pm 1, \pm 2, \dots, \\ &\mu = 1, 2, 3, \dots. \end{aligned}$$ 
(2.48)

The terms $R^{\text{①}}_{m\mu\nu}$ are the reflection coefficients that can be related to the modal impedance $Z^{\text{①}}_{m\mu\nu}$ by the following *infinite* matrix equation. For a given circumferential order $m$, the reflection coefficient $R^{\text{①}}_{m\mu\nu}$ is element $(\mu, \nu)$ of reflection matrix $\mathbf{R}^{\text{①}}_m$ at interface ①:

$$\mathbf{R}^{\text{①}}_m = [\mathbf{Z}^{\text{①}}_m \mathbf{K}_m + \mathbf{I}]^{-1}[\mathbf{Z}^{\text{①}}_m \mathbf{K}_m - \mathbf{I}],$$ 
(2.49)

where $\mathbf{I}$ is the identity matrix, and $\mathbf{K}_m$ is a diagonal matrix which is, for *fixed* circumferential order $m$, given by

$$\mathbf{K}_m = \begin{bmatrix} k_{m1}/k & 0 & \dots & 0 & \dots \\ 0 & k_{m2}/k & \dots & 0 & \dots \\ \vdots & \vdots & \ddots & \vdots & \vdots \\ 0 & 0 & \dots & k_{m\nu}/k & \dots \\ \vdots & \vdots & \dots & \vdots & \ddots \end{bmatrix}.$$ 
(2.50)

Because $m$ is fixed, $\mathbf{K}_m$ is only valid for *one value* of the circumferential order at a time, and generally will be different for each value of $m$. Here, $\nu$ is the radial order of the reflected modes, where $1 \leq \nu \leq \infty$. The (generally non-symmetric) matrix of reflection coefficients is defined as

$$\mathbf{R}^{\text{①}}_m = \begin{bmatrix} R^{\text{①}}_{m11} & R^{\text{①}}_{m12} & \dots & R^{\text{①}}_{m1\nu} & \dots \\ R^{\text{①}}_{m21} & R^{\text{①}}_{m22} & \dots & R^{\text{①}}_{m2\nu} & \dots \\ \vdots & \vdots & \ddots & \vdots & \vdots \\ R^{\text{①}}_{m\mu1} & R^{\text{①}}_{m\mu2} & \dots & R^{\text{①}}_{m\mu\nu} & \dots \\ \vdots & \vdots & \dots & \vdots & \ddots \end{bmatrix},$$ 
(2.51)

where the impedance matrix is given by

$$\mathbf{Z}^{\text{①}}_m = \begin{bmatrix} Z^{\text{①}}_{m11} & Z^{\text{①}}_{m12} & \dots & Z^{\text{①}}_{m1\nu} & \dots \\ Z^{\text{①}}_{m21} & Z^{\text{①}}_{m22} & \dots & Z^{\text{①}}_{m2\nu} & \dots \\ \vdots & \vdots & \ddots & \vdots & \vdots \\ Z^{\text{①}}_{m\mu1} & Z^{\text{①}}_{m\mu2} & \dots & Z^{\text{①}}_{m\mu\nu} & \dots \\ \vdots & \vdots & \dots & \vdots & \ddots \end{bmatrix}.$$ 
(2.52)

Expression (2.48) for the reflection at interface ① can be written as a matrix equation,

$$\mathbf{E}_m(-L)\mathbf{a}_m = \mathbf{R}^{\text{①}}_m \mathbf{E}_m(L)(\mathbf{b}_m + \mathbf{h}^{\text{①}}_m),$$ 
(2.53)

with

$$\boldsymbol{E}_m(z) = \begin{bmatrix} e^{-ik_{m1}z} & 0 & \dots & 0 & \dots \\ 0 & e^{-ik_{m2}z} & \dots & 0 & \dots \\ \vdots & \vdots & \ddots & \vdots & \vdots \\ 0 & 0 & \dots & e^{-ik_{m\nu}z} & \dots \\ \vdots & \vdots & \dots & \vdots & \ddots \end{bmatrix}, \tag{2.54}$$

and

$$\boldsymbol{a}_m = \begin{bmatrix} A''_{m1} & A''_{m2} & \dots & A''_{m\nu} & \dots \end{bmatrix}^{\mathrm{T}}, \tag{2.55}$$

$$\boldsymbol{b}_m = \begin{bmatrix} B''_{m1} & B''_{m2} & \dots & B''_{m\nu} & \dots \end{bmatrix}^{\mathrm{T}}, \tag{2.56}$$

$$\boldsymbol{h}_m^{①} = \begin{bmatrix} H_{m1}^{①} & H_{m2}^{①} & \dots & H_{m\nu}^{①} & \dots \end{bmatrix}^{\mathrm{T}}. \tag{2.57}$$

Similarly, at interface ② the matrix equation

$$\boldsymbol{E}_m(-L)\boldsymbol{b}_m = \boldsymbol{R}_m^{②}\boldsymbol{E}_m(L)(\boldsymbol{a}_m + \boldsymbol{h}_m^{②}), \tag{2.58}$$

can be derived, with

$$\boldsymbol{R}_m^{②} = [\boldsymbol{Z}_m^{②}\boldsymbol{K}_m + \boldsymbol{I}]^{-1}[\boldsymbol{Z}_m^{②}\boldsymbol{K}_m - \boldsymbol{I}]. \tag{2.59}$$

From equations (2.53) and (2.58) the still unknown coefficients $A''_{m\mu}$ and $B''_{m\mu}$ can be solved according to the generalized impedance boundary conditions at both exits of the duct. In the next section it will be shown how these infinite matrix equations can be implemented in an acoustic tool.

## 2.3   Numerical implementation

The numerical implementation of the analytical formulation for the acoustic radiation of baffled finite ducts with vibrating walls is not straightforward. The matrices in equations (2.53) and (2.58) are infinite in size and can therefore not be readily manipulated numerically. In general, an approximate solution can be obtained by truncating the infinite matrices a maximum $\nu = N$, and a set of $2N$ equations with $2N$ unknowns (the elements of $\boldsymbol{a}_m$ and $\boldsymbol{b}_m$) is obtained for every circumferential order $m$. When this system is solved, an explicit (approximate) *semi*-analytical expression for $p''$ is obtained and this leads to a closed form solution for the total pressure,

$$p(r,\theta,z) = \sum_{m=-\infty}^{\infty} \sum_{\mu=1}^{N} J_m(\alpha_{m\mu}r)e^{-im\theta}\left(A_{m\mu}(z)e^{-ik_{m\mu}z} + B_{m\mu}(z)e^{ik_{m\mu}z}\right), \tag{2.60}$$

with amplitudes $A_{m\mu}(z)$ and $B_{m\mu}(z)$ as in equation (2.38). After truncation, two problems remain to be solved: calculation of the integrals in equation (2.38) and solving the coupled truncated matrix equations (2.53) and (2.58). The implementation details of a solution to these problems will be presented next.

### 2.3.1 Fourier integral calculation

In order to use the proposed formulation for the pressure in a (planar) baffled finite duct, the convolution between the Fourier coefficients (with respect to the circumferential direction) of the wall velocity $\eta_m(z)$ and the function $e^{-ik_{m\mu}|z|}$ needs to be computed:

$$I = \int_{-L}^{L} \eta_m(z') e^{-ik_{m\mu}|z-z'|} dz'. \tag{2.61}$$

This integral has to be computed for every circumferential mode $m$ and every radial mode $\mu$. The integral can be split into the ranges $[-L, z]$ and $[z, L]$. Then, the absolute value operator in the exponential function can be removed:

$$I = \int_{-L}^{z} \eta_m(z') e^{-ik_{m\mu}(z-z')} dz' + \int_{z}^{L} \eta_m(z') e^{-ik_{m\mu}(z'-z)} dz'. \tag{2.62}$$

Since both integrals are bounded for all $z$, numerical integration is rather straightforward. When $k_{m\mu}$ is real, the duct wall normal velocity is multiplied with an oscillating function yielding a oscillating integrand. Therefore, the trapezoidal rule or Romberg integration should be used because these methods have a better convergence than Gauss-Legendre integration for oscillating integrands. When $k_{m\mu}$ is imaginary (and thus negative by definition), the normal velocity is multiplied with an exponentially decaying function, yielding an exponentially decaying integrand. This type of integrand can also be integrated efficiently with the trapezoidal rule or Romberg integration.

### 2.3.2 Matrix equation solution

After truncation of matrix equations (2.53) and (2.58), the coupled matrix equations

$$\boldsymbol{R}^{①}\boldsymbol{E}(L)(\boldsymbol{a} + \boldsymbol{h}^{①}) = \boldsymbol{E}(-L)\boldsymbol{b}, \tag{2.63a}$$

$$\boldsymbol{R}^{②}\boldsymbol{E}(L)(\boldsymbol{b} + \boldsymbol{h}^{②}) = \boldsymbol{E}(-L)\boldsymbol{a}, \tag{2.63b}$$

(where subscript $m$ has been suppressed for clarity) need to be solved simultaneously to obtain values for the amplitudes $A''_{m\mu}$ and $B''_{m\mu}$, which are the elements of vectors $\boldsymbol{a}$ and $\boldsymbol{b}$, respectively. The main problem in obtaining this solution are the low condition numbers of matrices $\boldsymbol{R}^{①}$, $\boldsymbol{R}^{②}$ and $\boldsymbol{E}(\pm L)$, so the solution of the system is not straightforward.

Since both ends of the duct are similar (but mirrored), the reflection behavior of the sound waves is also similar. Therefore, the reflection matrices at both ends are the same: $\boldsymbol{R}^{①} = \boldsymbol{R}^{②} = \boldsymbol{R}$. Equations (2.63a) and (2.63b) are then summed up and $\boldsymbol{r}_+ = \boldsymbol{a} + \boldsymbol{b}$ is introduced, to obtain

$$[\boldsymbol{I} - \boldsymbol{E}(L)\boldsymbol{R}\boldsymbol{E}(L)]\,\boldsymbol{r}_+ = \boldsymbol{E}(L)\boldsymbol{R}\boldsymbol{E}(L)\left[\boldsymbol{h}^{②} + \boldsymbol{h}^{①}\right]. \tag{2.64a}$$

Equation (2.63b) subtracted from equation (2.63a) and introducing $\boldsymbol{r}_- = \boldsymbol{a} - \boldsymbol{b}$ yields

$$[\boldsymbol{I} + \boldsymbol{E}(L)\boldsymbol{R}\boldsymbol{E}(L)]\,\boldsymbol{r}_- = \boldsymbol{E}(L)\boldsymbol{R}\boldsymbol{E}(L)\left[\boldsymbol{h}^{②} - \boldsymbol{h}^{①}\right]. \tag{2.64b}$$

Both equations can now be solved separately for $r_+$ and $r_-$. The vectors $a$ and $b$ are simply related to these vectors:

$$a = \frac{1}{2}(r_+ + r_-),\tag{2.65a}$$

$$b = \frac{1}{2}(r_+ - r_-).\tag{2.65b}$$

Using this solution strategy is advantageous over direct substitution of equation (2.63b) in equation (2.63a), because in that case the matrix product $E(L)^2$ is introduced which leads to numerical underflow errors for large values of $L$.

The coupled matrix equations (2.63) can also be solved iteratively by using the recurrent relationship

$$a_{i+1} = E(L)RE(L)\left[b_i + h^{①}\right],\tag{2.66a}$$

$$b_{i+1} = E(L)RE(L)\left[a_i + h^{②}\right],\tag{2.66b}$$

and starting the recursion with $a_0 = 0$, $b_0 = 0$. A good measure for the convergence of the iteration is the relative difference in the sound power radiated out of the baffled duct between two subsequent iterations,

$$\bar{P} = \bar{P}_z(L) - \bar{P}_z(-L),\tag{2.67}$$

with $\bar{P}_z(z)$ as the power flow in positive $z$-direction at a cross-section:

$$\bar{P}_z(z) = \sum_{m=-\infty}^{\infty}\sum_{\mu=1}^{\infty}\frac{\pi N_{m\mu}^2}{\rho_0 c_0 k}\times$$

$$\left\{\text{Re}(k_{m\mu})\left[|A_{m\mu}(z)|^2 - |B_{m\mu}(z)|^2\right] + 2\,\text{Im}(k_{m\mu})\,\text{Im}\left[A_{m\mu}^*(z)B_{m\mu}(z)\right]\right\}.\tag{2.68}$$

and with $N_{m\mu}^2$ from equation (2.30) (see appendix B.4 for the derivation of the power relations).

## 2.4    Summary and discussion

A semi-analytical model for the acoustic radiation of vibrating walls inside a baffled finite duct was presented. The model originates from general duct acoustics theory. From this general theory, a description of the acoustic radiation of point sources in infinite ducts was derived. This solution represents the acoustic impulse response of the infinite duct. It was shown that the radiation of a finite part of the wall of an infinite duct is merely a convolution of the mentioned impulse response and the wall vibration distribution. To account for the planar baffles at the duct's exits, so-called generalized radiation impedances were used. To compute these impedances, a new algorithm was developed. The pressure solution of the acoustic problem was shown to be a superposition of a particular solution to the wall vibration distribution and a homogeneous solution satisfying a rigid wall boundary condition. With these, two matrix equations were formulated, one for each side of the duct, which constitute a closed form solution for the acoustic radiation of the wall inside a finite baffled duct.

The mathematical formulation of the semi-analytical model that is presented here offers direct physical insight into the acoustics of baffled finite ducts. For example, the relationship between duct radius $a$ and the axial wavenumber $k_{m\mu}$ reveals that cut-on phenomena, which are well-known from the general duct acoustics, also play a role in these baffled finite ducts with vibrating walls. Furthermore, the subdivision of $p$ in a particular solution $p'$ and a homogeneous solution $p''$, see equation (2.32) and following, reveals that the former solution results directly from the wall vibration, while the latter is due to the reflection of duct modes by the generalized impedance boundary condition at the duct's exits. The convolution integral indicates that a certain duct mode will only be excited directly at a particular frequency if the wave content of the excitation matches the axial wavenumber of that particular duct mode. By examining the values of the reflection coefficients for the duct modes, one can easily determine for each duct mode, what part of the mode is transmitted outside the duct, and what part is reflected back into the duct. In brief, the semi-analytical model presented here establishes various important radiation characteristics of baffled finite ducts that can hardly be obtained by discretization methods like the finite element method or the boundary element method.

The formulation that was presented here was implemented in the acoustic code bArd [1998]. The application of this model for the acoustic design of MRI scanners will be shown in chapters 5 and 6.

# 3 An improved Fourier boundary element method for the radiation of axisymmetric structures[*]

## 3.1 Introduction

The two most commonly used discretization methods in acoustics are the acoustic finite element method (FEM) and the acoustic boundary element method (BEM). The FEM is often used for interior radiation problems because it is more efficient than BEM for those problems. For exterior radiation problems the BEM is preferred because then only the bounds of the acoustic domain have to be discretized (and not the domain itself as for the FEM) and also the Sommerfeld radiation condition (or causality condition) at infinity is automatically satisfied [Ciskowski and Brebbia, 1991]. So-called wave-envelope elements [Astley and Eversman, 1988; Cremers et al., 1994; Astley et al., 1998] remove some of the disadvantages of the FEM for exterior radiation problems, but their application is not yet widespread.

A major drawback of the BEM is its numerically less attractive implementation which requires assembling and solving full, complex, non-symmetric system matrices. This seriously hampers the numerical efficiency of the BEM. However, for axisymmetric structures like the MRI scanner, the efficiency of the BEM can be improved significantly with the Fourier BEM method as will be explained next.

Conceptually, the acoustic Fourier boundary element method (Fourier BEM) applies a Fourier series expansion in the angular coordinate of the acoustic variables in the problem. As a result, the surface integral in the boundary integral equations reduces to a line integral and an integral over the angle of revolution (circumferential integral). The advantages of this approach are evident. Discretization of the body requires only meshing of the generator of the body with line elements. Also, the computational effort for solving the system of equations is reduced because of a substantial decrease in the number of unknowns.

Traditionally, the computation time required for an acoustic analysis with the Fourier BEM is linearly dependent on the number of Fourier harmonics in the boundary conditions because a complete BEM calculation has to be done for every Fourier harmonic that is present in the boundary conditions. For complex boundary conditions with a lot of harmonics, this seriously deteriorates the better performance of the Fourier BEM compared to 3-dimensional BEM calculations. In the improved Fourier BEM formulation that will be

---

[*] This chapter was partly reproduced from Kuijpers et al. [1997]

presented here, this problem is tackled by performing the most time-consuming integrations in the Fourier BEM formulation simultaneously, by deploying efficient fast Fourier transform algorithms.

## 3.2  Acoustic Fourier boundary integral equations

Consider a simple axisymmetric body $B$ (see figure 3.1). When harmonic solutions for the sound field with angular frequency are considered, the acoustic pressure $p$ and velocity $\boldsymbol{u}$ can be expressed as

$$\tilde{p}(r, \theta, z, t) = \mathrm{Re}\left[p(r, \theta, z, \omega)\mathrm{e}^{i\omega t}\right], \qquad \tilde{\boldsymbol{u}}(r, \theta, z, t) = \mathrm{Re}\left[\boldsymbol{u}(r, \theta, z, \omega)\mathrm{e}^{i\omega t}\right]. \qquad (3.1)$$

The harmonic acoustic pressure satisfies the homogeneous Helmholtz equation (see equation (2.5)):

$$\nabla^2 p(\boldsymbol{y}) + k^2 p(\boldsymbol{y}) = 0, \qquad (3.2)$$

with harmonic pressure $p(\boldsymbol{y})$ at a point $\boldsymbol{y}$, free field wavenumber $k = \omega/c_0$, speed of sound $c_0$, and where the gradient operator $\nabla$ is applied with respect to point $\boldsymbol{y}$, throughout this chapter. Additionally, the Green's function $G(\boldsymbol{x}, \boldsymbol{y})$ is introduced, which by definition satisfies the inhomogeneous Helmholtz equation

$$\nabla^2 G(\boldsymbol{x}, \boldsymbol{y}) + k^2 G(\boldsymbol{x}, \boldsymbol{y}) = -Q\delta(\boldsymbol{x} - \boldsymbol{y}), \qquad (3.3)$$

with a unit point source at $\boldsymbol{y} = \boldsymbol{x}$. For a 3-dimensional infinite domain, the Green's function is given by

$$G(\boldsymbol{x}, \boldsymbol{y}) = \frac{\mathrm{e}^{-ikR(\boldsymbol{x}, \boldsymbol{y})}}{4\pi R(\boldsymbol{x}, \boldsymbol{y})}, \qquad (3.4)$$

with the distance $R$ between the points $\boldsymbol{x}$ and $\boldsymbol{y}$ being defined as $R(\boldsymbol{x}, \boldsymbol{y}) = |\boldsymbol{x} - \boldsymbol{y}|$. Now equation (3.2) is multiplied by $G(\boldsymbol{x}, \boldsymbol{y})$ and subtracted from equation (3.3) multiplied by $p(\boldsymbol{y})$. The resulting equation is then integrated over the acoustic volume $V$ which yields

$$\int_V \left(p(\boldsymbol{y})\nabla^2 G(\boldsymbol{x}, \boldsymbol{y}) - G(\boldsymbol{x}, \boldsymbol{y})\nabla^2 p(\boldsymbol{y})\right) \mathrm{d}V(\boldsymbol{y}) = -\int_V p(\boldsymbol{y})\delta(\boldsymbol{x} - \boldsymbol{y})\mathrm{d}V(\boldsymbol{y}). \qquad (3.5)$$

When both Green's theorem

$$\int_V \left(\Psi\nabla^2\Phi - \Phi\nabla^2\Psi\right)\mathrm{d}V = -\int_S (\Psi\nabla\Phi - \Phi\nabla\Psi)\cdot\boldsymbol{n}\,\mathrm{d}S \qquad (3.6)$$

with *inward* surface normal vector $\boldsymbol{n}$, and the sampling property of the $\delta$-function,

$$\int f(x)\delta(x - x_0)\mathrm{d}x = f(x_0), \qquad (3.7)$$

are applied to equation (3.5), the Kirchhoff-Helmholtz integral equation for the acoustic pressure $p(\boldsymbol{x})$ at an observer point $\boldsymbol{x}$ is obtained,

$$C(\boldsymbol{x})\cdot p(\boldsymbol{x}) = \int_S [p(\boldsymbol{y})\nabla G(\boldsymbol{x}, \boldsymbol{y})\cdot\boldsymbol{n}(\boldsymbol{y}) - G(\boldsymbol{x}, \boldsymbol{y})\nabla p(\boldsymbol{y})\cdot\boldsymbol{n}(\boldsymbol{y})]\,\mathrm{d}S(\boldsymbol{y}), \qquad (3.8)$$

**figure 3.1** Simple axisymmetric body *B*.
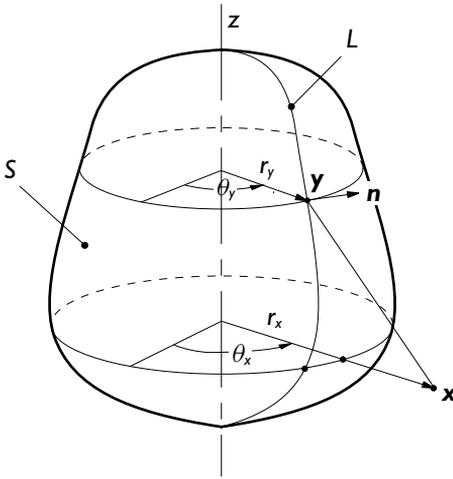
$S$:  surface
$L$:  body generator
$\boldsymbol{x}$:  observer point with cylindrical coordinates $(r_x, \theta_x, z_x)$
$\boldsymbol{y}$:  surface point with cylindrical coordinates $(r_y, \theta_y, z_y)$
$\boldsymbol{n}$:  surface normal

or with help of the momentum equation, $i\rho_0\omega\boldsymbol{u} + \nabla p = \boldsymbol{0}$,

$$C(\boldsymbol{x}) \cdot p(\boldsymbol{x}) = \int_S [p(\boldsymbol{y})\nabla G(\boldsymbol{x}, \boldsymbol{y}) \cdot \boldsymbol{n}(\boldsymbol{y}) + ik\rho_0 c_0 G(\boldsymbol{x}, \boldsymbol{y})v(\boldsymbol{y})]\, dS(\boldsymbol{y}), \qquad (3.9)$$

with surface normal velocity $v = \boldsymbol{u} \cdot \boldsymbol{n}$, acoustic fluid density $\rho_0$, and $C(\boldsymbol{x})$ as a coefficient depending on the position of $\boldsymbol{x}$ [Ciskowski and Brebbia, 1991]:

$$C(\boldsymbol{x}) = \begin{cases} 0, & \text{for } \boldsymbol{x} \text{ outside the acoustic medium } V, \\ 1, & \text{for } \boldsymbol{x} \text{ inside the acoustic medium } V, \\ \frac{1}{2}, & \text{for } \boldsymbol{x} \text{ on the smooth surface } S \text{ of the acoustic medium.} \end{cases} \qquad (3.10)$$

For any other position of $\boldsymbol{x}$ on $S$ for which there is no unique surface normal, for example when $\boldsymbol{x}$ is on an edge or a corner, the value of $C(\boldsymbol{x})$ is given by

$$C(\boldsymbol{x}) = \begin{cases} 1 + \dfrac{1}{4\pi} \displaystyle\int_S \nabla \dfrac{1}{R(\boldsymbol{x}, \boldsymbol{y})} \cdot \boldsymbol{n}(\boldsymbol{y})\, dS(\boldsymbol{y}), & \text{for the exterior acoustic problem,} \\ -\dfrac{1}{4\pi} \displaystyle\int_S \nabla \dfrac{1}{R(\boldsymbol{x}, \boldsymbol{y})} \cdot \boldsymbol{n}(\boldsymbol{y})\, dS(\boldsymbol{y}), & \text{for the interior acoustic problem.} \end{cases}$$

$$(3.11)$$

The geometry of an axisymmetric body with arbitrary boundary conditions can be described using a cylindrical coordinate system $(r, \theta, z)$. All variables then become functions of the cylindrical coordinates $r$, $\theta$, and $z$, i.e.,

$$p(\boldsymbol{x}) = p(r_x, \theta_x, z_x),$$
$$p(\boldsymbol{y}) = p(r_y, \theta_y, z_y),$$
$$G(\boldsymbol{x}, \boldsymbol{y}) = G(r_x, \theta_x, z_x; r_y, \theta_y, z_y),$$
$$dS(\boldsymbol{y}) = r_y\, d\theta_y\, dL_y,$$

with $(r_x, \theta_x, z_x)$ and $(r_y, \theta_y, z_y)$ as the coordinates of the observer point $\boldsymbol{x}$ and the surface point $\boldsymbol{y}$, respectively, and $\mathrm{d}L_y$ as the differential length of the generator $L$ of the body at $\boldsymbol{y}$. Because of the axisymmetric properties of the body $B$ the variables can be expanded in Fourier series. This Fourier series can be written with the complex exponential notation, but here it is chosen to follow the derivation of Soenarko [1993], who used

$$p(\boldsymbol{y}) = \sum_{m=0}^{\infty} \left[ p_m^s \sin(m\theta_y) + p_m^c \cos(m\theta_y) \right], \tag{3.12}$$

$$p^\circ(\boldsymbol{x}) = \sum_{m=0}^{\infty} \left[ p_m^{s,\circ} \sin(n\theta_x) + p_m^{c,\circ} \cos(m\theta_x) \right], \tag{3.13}$$

with superscript $^\circ$ to discern the Fourier coefficients for the surface point $\boldsymbol{y}$ and observer point $\boldsymbol{x}$. Note that the Fourier coefficients still depend on the coordinates $r$ and $z$, but the dependence of pressure $p$ on coordinate $\theta$ is expressed through the sine and cosine terms of the Fourier expansion. The other functions of equation (3.9) can be expanded likewise:

$$G(\boldsymbol{x}, \boldsymbol{y}) = \sum_{m=0}^{\infty} \left[ G_m^s \sin(m\theta_y) + G_m^c \cos(m\theta_y) \right], \tag{3.14}$$

$$v(\boldsymbol{y}) = \sum_{m=0}^{\infty} \left[ v_m^s \sin(m\theta_y) + v_m^c \cos(m\theta_y) \right], \tag{3.15}$$

$$\nabla G(\boldsymbol{x}, \boldsymbol{y}) \cdot \boldsymbol{n} \equiv G'(\boldsymbol{x}, \boldsymbol{y}) = \sum_{m=0}^{\infty} \left[ G'^s_m \sin(m\theta_y) + G'^c_m \cos(m\theta_y) \right]. \tag{3.16}$$

The Fourier coefficients in these equations are independent of $\theta_y$ but still dependent on the $r_y$ and $z_y$. Observe that the Fourier coefficients of the expansions of the Green's function and its normal derivative (i.e., $G_m^s$, $G_m^c$, $G'^s_m$, and $G'^c_m$) are also dependent on all the cylindrical coordinates of point $\boldsymbol{x}$: $r_x$, $\theta_x$, and $z_x$.

With the Fourier series description for the circumferential dependence of the acoustic variables, a modified form of the Kirchhoff-Helmholtz integral equation can be obtained. To that end, it is convenient to reformulate the Fourier coefficients of the Green's function and its derivative. The coefficients are determined by the standard Fourier transformation rules, for instance,

$$G_m^s = \frac{1}{\pi} \int_0^{2\pi} \frac{e^{-ikR(\boldsymbol{x}, \boldsymbol{y})}}{4\pi R(\boldsymbol{x}, \boldsymbol{y})} \sin(m\theta_y)\, \mathrm{d}\theta_y, \qquad m = 0, 1, 2, \ldots \tag{3.17}$$

For brevity, the addition $m = 0, 1, 2, \ldots$ will be omitted further. By defining $\theta \equiv \theta_y - \theta_x$ such that $\mathrm{d}\theta = \mathrm{d}\theta_y$ equation (3.17) can be written as

$$G_m^s = \frac{1}{\pi} \int_0^{2\pi} \frac{e^{-ikR(\boldsymbol{x}, \boldsymbol{y})}}{4\pi R(\boldsymbol{x}, \boldsymbol{y})} \sin(m(\theta + \theta_x))\, \mathrm{d}\theta, \tag{3.18}$$

With the aid of a trigonometric identity, equation (3.18) can be rewritten as

$$G_m^s = \frac{1}{\pi} \int_0^{2\pi} \frac{e^{-ikR(\mathbf{x},\mathbf{y})}}{4\pi R(\mathbf{x},\mathbf{y})} \sin(m\theta)\cos(m\theta_x)\, d\theta + \frac{1}{\pi} \int_0^{2\pi} \frac{e^{-ikR(\mathbf{x},\mathbf{y})}}{4\pi R(\mathbf{x},\mathbf{y})} \cos(m\theta)\sin(m\theta_x)\, d\theta.$$

(3.19)

Because $\sin(m\theta)$ is an odd function of $\theta = \pi$ and the remainder of the integrand is symmetric around $\theta = \pi$ in the interval $[0, 2\pi]$, the first integral of equation (3.19) vanishes. Introducing

$$H_m = \int_0^{2\pi} \frac{e^{-ikR(\mathbf{x},\mathbf{y})}}{4\pi R(\mathbf{x},\mathbf{y})} \cos(m\theta)\, d\theta,$$

(3.20)

equation (3.19) becomes

$$G_m^s = \frac{1}{\pi} H_m \sin(m\theta_x).$$

(3.21)

The cosine coefficients $G_m^c$ of equation (3.14) can be derived in a similar manner:

$$G_m^c = \frac{1}{\pi} H_m \cos(m\theta_x).$$

(3.22)

The Fourier coefficients of equation (3.16) can also be determined analogously. Using

$$H_m' = \int_0^{2\pi} \nabla\left(\frac{e^{-ikR(\mathbf{x},\mathbf{y})}}{4\pi R(\mathbf{x},\mathbf{y})}\right) \cdot \mathbf{n} \cos(m\theta)\, d\theta,$$

(3.23)

they can be written as

$$G_m'^s = \frac{1}{\pi} H_m' \sin(m\theta_x), \qquad G_m'^c = \frac{1}{\pi} H_m' \cos(m\theta_x).$$

(3.24)

The Fourier coefficients in equations (3.12), (3.13), and (3.15) can be expressed similarly, for instance,

$$p_m^s(\mathbf{y}) = \frac{1}{\pi} \int_0^{2\pi} p(\mathbf{y}) \sin(m\theta_y)\, d\theta_y,$$

(3.25)

and similar expressions for $p_m^c(\mathbf{y})$, $p_m^{s\,\circ}(\mathbf{x})$, $p_m^{c\,\circ}(\mathbf{x})$, $v_m^s(\mathbf{y})$, and $v_m^c(\mathbf{y})$. By expanding all variables in Fourier series, equation (3.9) takes the form (where the index in some of the

summations is taken *n* for clarity)

$$C(\mathbf{x}) \left\{ \sum_{m=0}^{\infty} \left[ p_m^{s\,\circ} \sin(m\theta_x) + p_m^{c\,\circ} \cos(m\theta_x) \right] \right\}$$

$$= \int_L \int_0^{2\pi} \left\{ \sum_{n=0}^{\infty} \left[ p_n^s \sin(n\theta_y) + p_n^c \cos(n\theta_y) \right] \right\} \times$$

$$\left\{ \sum_{m=0}^{\infty} \frac{1}{\pi} H_m' [\sin(m\theta_x)\sin(m\theta_y) + \cos(m\theta_x)\cos(m\theta_y)] \right\} r_y \, d\theta_y \, dL_y \qquad (3.26)$$

$$+ ik\rho_0 c_0 \int_L \int_0^{2\pi} \left\{ \sum_{n=0}^{\infty} \left[ v_n^s \sin(n\theta_y) + v_n^c \cos(n\theta_y) \right] \right\} \times$$

$$\left\{ \sum_{m=0}^{\infty} \frac{1}{\pi} H_m [\sin(m\theta_x)\sin(m\theta_y) + \cos(m\theta_x)\cos(m\theta_y)] \right\} r_y \, d\theta_y \, dL_y.$$

Matching the terms on the left- and right-hand sides of equation (3.26) and using the orthogonality properties for integrals involving $\sin(m\theta_y)\sin(n\theta_y)$, $\sin(m\theta_y)\cos(n\theta_y)$, and $\cos(m\theta_y)\cos(n\theta_y)$, the following expressions can be obtained after integration over $d\theta_y$:

$$C(\mathbf{x})p_m^{s\,\circ}(\mathbf{x}) = \int_L \left[ p_m^s H_m' + ik\rho_0 c_0 v_m^s H_m \right] r_y \, dL_y, \qquad (3.27)$$

$$C(\mathbf{x})p_m^{c\,\circ}(\mathbf{x}) = \int_L \left[ p_m^c H_m' + ik\rho_0 c_0 v_m^c H_m \right] r_y \, dL_y. \qquad (3.28)$$

All functions in equations (3.27) and (3.28) are no longer explicitly dependent on angle $\theta$, but still depend on the coordinates along $L$. When the Fourier coefficients of surface pressure $p_m^s$, $p_m^c$ and its normal derivative $p'^s_m$, $p'^c_m$ are known, the acoustic pressure at any observer point $\mathbf{x}$ inside, outside or on body $B$ can be expressed as (see equation (3.13))

$$C(\mathbf{x})p^{\circ}(\mathbf{x}) = \int_L \sum_{m=0}^{\infty} \left\{ \left[ p_m^s H_m' + ik\rho_0 c_0 v_m^s H_m \right] \sin(m\theta_x) \right.$$

$$\left. + \left[ p_m^c H_m' + ik\rho_0 c_0 v_m^c H_m \right] \cos(m\theta_x) \right\} r_y dL_y. \quad (3.29)$$

When observer point $\mathbf{x}$ is on the surface of body $B$, equations (3.27) and (3.28) can be rewritten as

$$C(\mathbf{x})p_m^s(\mathbf{x}) = \int_L \left[ p_m^s H_m' + ik\rho_0 c_0 v_m^s H_m \right] r_y \, dL_y, \qquad (3.30)$$

$$C(\mathbf{x})p_m^c(\mathbf{x}) = \int_L \left[ p_m^c H_m' + ik\rho_0 c_0 v_m^c H_m \right] r_y \, dL_y \qquad (3.31)$$

(where the superscript $\circ$ has disappeared). These modified Kirchhoff-Helmholtz integral equations constitute an implicit formulation for the surface pressure and its normal derivative. It can be used to determine the boundary values of $p$ when $v$ is known and vice versa.

## 3.3    Implementation of acoustic Fourier BEM

The solution of the Kirchhoff-Helmholtz equation for axisymmetric structures, given in equation (3.29), can be obtained numerically by solving equations (3.30) and (3.31) using standard boundary element procedures. The generator $L$ of the axisymmetric body is discretized and the geometry and acoustic variables $p$ and $v$ are assumed to vary according to isoparametric shape functions on the surface of the body. The discretization of the body involves only line elements.

In this acoustic Fourier BEM formulation, two issues are very important: the evaluation of the integrals (3.11), (3.20), and (3.23) over the angular coordinate $\theta$, and the non-uniqueness problem. For acoustic Fourier BEM, these issues have received considerable attention in the literature the past decade [Akyol, 1986; Soenarko, 1993; Juhl, 1993; Wang et al., 1997; Kuijpers et al., 1997].

### 3.3.1    Circumferential integral evaluation

The computation of the circumferential integrals (3.11), (3.20), and (3.23) causes considerable numerical problems in implementation of the Fourier BEM. The integrand of these integrals can be singular and oscillatory. Numerical values for these integrals were obtained using trapezoidal rule quadrature by Akyol [1986]. This method provided accurate results, but it was pointed out that the efficiency of the integral computation needed further investigation. A different method for the computation of the integrals was proposed by Soenarko [1993] and Juhl [1993] and employed by Wang et al. [1997], who reformulated the integrand and employed a series of elliptic integrals for the singular part of the integral and Gaussian quadrature for the regular part. Matviyenko [1995] proposed a recurrence relation for these integrals and unfoundedly claimed its superior efficiency.

The possible singularities in the circumferential integrands of equations (3.20) and (3.23) are not the only difficulties in their computation. The cosine function in the expressions for $H_m$ and $H'_m$ causes the total integrand to oscillate rapidly for high Fourier harmonic numbers $n$. Moreover, the $R(\boldsymbol{x}, \boldsymbol{y})^{-1}$ function in these integrals causes a steep slope of the integrand near $\theta = 0$ and $\theta = 2\pi$, when the distance between $\boldsymbol{x}$ and $\boldsymbol{y}$ is relatively small. Therefore, special attention should be paid to the evaluation of these integrals.

Calculation of the circumferential integrals consumes a major portion of the total amount of computation time that is required for an acoustic analysis with the Fourier BEM. The integrals need to be computed often, and the calculation itself is computationally expensive. In general, the line integrals from equations (3.30) or (3.31) need to be computed numerically for each Fourier harmonic $m$, for a number of observer points $\boldsymbol{x}$. This requires a value for $H_m$ and $H'_m$ and thus two circumferential integral evaluations on each integration point of the line integral, for each Fourier harmonic number $m$. In addition, applying fixed point numerical integration for the (regular part of the) Fourier integrals, like Gaussian or trapezoidal rule quadrature, requires a large number of integration points in circumferential direction to obtain sufficiently accurate results [Akyol, 1986]. This is particularly true for a high Fourier harmonic number $m$, where the integrand evinces an oscillatory behavior. The long computation times resulting from the application of fixed point integration schemes, as proposed by Akyol [1986], Soenarko [1993], and Juhl [1993], weaken the advantages of the Fourier BEM compared to the 3-dimensional BEM. Kuijpers et al. [1997] showed that an integral evaluation based on Fast Fourier Transform (FFT) is numerically more attractive when multiple Fourier harmonics are present in the boundary conditions.

*Implementation of an integration algorithm based on fast Fourier transform*

For a sufficiently *accurate* and *efficient* evaluation of the integrals (3.20) and (3.23) for $H_m$ and $H'_m$, respectively, a new method based on fast Fourier transform (FFT) was developed. The integrands in the expressions for $H_m$ and $H'_m$ consist of a reasonable smooth (but possibly singular) function multiplied by a cosine function. The integrand without the cosine function is an even periodic function around $\theta = 0$ with a period equal to $2\pi$. Given an even periodic function $h(x)$ with period $2T$, the Fourier coefficients $H_m$ of this function are given by [Kreyszig, 1993]

$$H_m = \frac{1}{T} \int_{-T}^{T} h(x) \cos\left(\frac{m\pi}{T}x\right) dx = \frac{1}{T} \int_{0}^{2T} h(x) \cos\left(\frac{m\pi}{T}x\right) dx. \tag{3.32}$$

With $x \equiv \theta$ and $T = \pi$, this shows that equations (3.20) and (3.23) are valid expressions of the Fourier coefficients $H_m$ and $H'_m$ of the complex even functions (for fixed $r_x$, $z_x$, $r_y$, and $z_y$)

$$h(\theta) = \frac{e^{-ikR(\theta)}}{4R(\theta)} \tag{3.33}$$

and

$$h'(\theta) = \nabla\left(\frac{e^{-ikR(\theta)}}{4R(\theta)}\right) \cdot \boldsymbol{n}, \tag{3.34}$$

respectively, which are in fact slightly modified forms of the 3-dimensional free-space Green's function from equation (3.4) and its normal derivative. Hence, to compute the integrals in the expressions for $H_m$ and $H'_m$, the $m$th Fourier coefficient of the complex functions $h$ and $h'$, respectively, can be used.

In numerical mathematics, the algorithm normally used for an efficient computation of the Fourier coefficients of a (complex) function is fast Fourier transform (FFT). FFT algorithms are optimized for speed while their accuracy is unaffected. Therefore, they are a good alternative for computing the integrals $H_m$ and $H'_m$, but generally they are more expensive than most fixed point numerical integration routines. However, a significant advantage of the proposed method is that by one FFT, the Fourier coefficients of many Fourier harmonics are calculated, whereas the fixed point integration methods required an integral evaluation for every Fourier harmonic number $m$.

An algorithm for the evaluation of the integrals in equations (3.20) and (3.23) using FFT requires the following actions:

1. Determination of the number of samples $n_{FFT}$ needed for computation of integrals $H_m$ and $H'_m$ with a desired accuracy.

2. Evaluation of the functions $h$, equation (3.33), and $h'$, equation (3.34), on $n_{FFT}$ equidistant values of the parameter $\theta$ in the interval $[0, 2\pi]$.

3. Fast Fourier transformation of the $n_{FFT}$ computed function values.

4. Selection of the $m$th terms of the calculated Fourier spectrums which are numerical values for the integrals $H_m$ and $H'_m$.

Numerical problems can occur when $x$ coincides with $y$ because the functions $h$ and $h'$ cannot be evaluated due to the $R^{-1}$ singularity in equations (3.33) and (3.34). This problem can be circumvented by taking surface integration points $y$ that do not coincide with the observer point $x$ when the line integrals (3.30) and (3.31) are computed. Gauss–log integration [Lean and Wexler, 1985] should then be applied for the line integrals because the functions $h$ and $h'$ have logarithmic behavior near the singularity.

Other methods proposed in the literature to handle a singular integrand use a technique of subtracting and adding up the singular part of the integrand from the regular part, resulting in a regular and singular (surface) integral. Then, special (analytical) integration techniques [Guiggiani and Casalini, 1987; Liao and Xu, 1992] are used for the singular integral, and ordinary (Gauss–Legendre) integration techniques are used for the regular part. To apply this technique here, a special integration technique should be developed for the integral over a ring-shaped surface which contains the $R^{-1}$ singularity. The integration region can be split up in an integral over the circumference and an integral over a generator segment of the vibrating body. The circumferential integral yields elliptic integrals of the first and second kind [Soenarko, 1993], but an analytical solution for the integration of these elliptic integrals over the generator segment is not available. Therefore, this regularization method cannot be used here. It should however be noted that this is not a consequence of the proposed FFT method but a general result for all Fourier BEM implementations.

The application of the method of computing the circumferential integrals using FFT techniques is not limited to acoustic problems governed by the Helmholtz equation. In like manner, the new method is usable in non-acoustic Fourier BEM applications. The only condition to be fulfilled for the kernel is that it has to be a periodic function of $\theta$.

*Efficiency of the FFT method*

Regarding efficiency, it is preferable that the number of evaluations of the functions $h(\theta)$ and $h'(\theta)$ can be chosen as low as possible, because this number is directly related to the cost of the FFT algorithm in particular and the cost of the total method in general. The number of required evaluations of these functions is determined by the desired accuracy of the FFT process. Signal leakage and aliasing in the Fourier transform process should be taken into account. This means that precisely an integer number of periods of the periodic functions $h(\theta)$ and $h'(\theta)$ should be sampled, and that the sampling frequency should at least be twice the highest frequency present in the functions. The first requirement is easily met because the period of the functions $h(\theta)$ and $h'(\theta)$ is known to be exactly $2\pi$ for axisymmetric structures. To satisfy the requirements for aliasing, however, the frequency content of functions $h(\theta)$ and $h'(\theta)$ needs to be predicted because it is not known beforehand. This is the topic of the remaining part of this section. For numerical efficiency it is desirable that the number of Fourier transform points can be written as $2^f$ with $f$ as a positive integer number.

A closer look at the functions $h$ and $h'$ that are Fourier transformed is illustrative to establish a reasonable expression for the minimum number of Fourier transform points $n_{\text{FFT}}$ required for each integral evaluation. A representative picture of the function $h$ is plotted in figure 3.2.

The steepness of the curve close to $\theta = 0$ and $\theta = 2\pi$ is determined by the ratio of the minimum and maximum $R$ (distance between the points $x$ and $y$), because of the factor
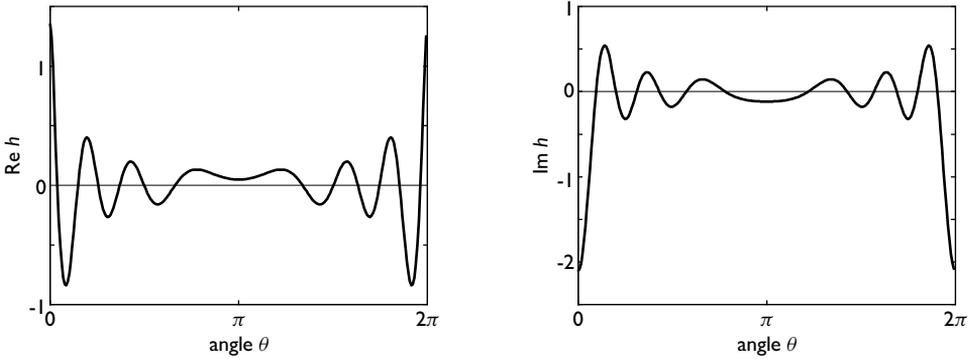
**figure 3.2** Function $h$ for $\mathbf{x} = (1, 0, 0)$, $\mathbf{y} = (1, 0, 0.1)$ and $k = 10$.

$R^{-1}$ in equation (3.33) for $h$. The ratio $R_{max}/R_{min}$ can serve as a dimensionless scale factor for the problem's geometry. The rapid change in steepness of the curve for large values of this ratio causes nonzero high harmonic number components in the Fourier transform of the function $h$. Therefore, a sufficiently high number of Fourier points has to be used. Hence, a criterion for the minimum number of Fourier points needed should be a function of a steepness parameter:

$$c_s = R_{max}/R_{min}. \tag{3.35}$$

The oscillations in the curves for the real and imaginary part are caused by the term $e^{-ikR(\theta)} = \cos(kR) - i\sin(kR)$ for large numbers of $k$ and/or a large difference between the minimum and maximum value for $R$. Thus, the criterion for the minimum number of Fourier points should also be a function of an oscillation parameter:

$$c_o = k(R_{max} - R_{min}). \tag{3.36}$$

Similar considerations can be made for the Fourier transform of $h'$, leading to identical parameters $c_s$ and $c_o$.

An expression for the minimum number of Fourier points is dependent on the characteristics of the integrands $h$ and $h'$ which can be described by the parameters $c_s$ and $c_o$. So an expression for $n_{FFT}$ can be expressed as a function of those parameters:

$$n_{FFT} = n_{FFT}(c_s, c_o) = n_{FFT}(R_{max}, R_{min}, k) = n_{FFT}(\mathbf{x}, \mathbf{y}, k). \tag{3.37}$$

For an efficient application of the FFT method, an expression for $n_{FFT}$ can be developed for a desired accuracy. The expression that can be derived is generally applicable for efficiently computing integrals in equations (3.20) and (3.23) with FFT integration. For efficiency, it is also important to obtain a relatively simple expression $n_{FFT}$, because it must be used for each FFT based integral evaluation separately. Fortunately, a simple expression can be derived for practical application, as is illustrated next.

For the FFT method, an expression for the minimum number of Fourier points $n_{FFT}$ was developed. For a large number of parameter values $c_s$ in the range $[1, 2000]$ and $c_o$ in the range $[0, 100]$, the integrals (3.20) and (3.23) were computed with the proposed method until convergence was achieved. Each parameter pair $c_s$ and $c_o$ has a specific minimum

**(a)** Sphere radiation.                    **(b)** Cylinder radiation.
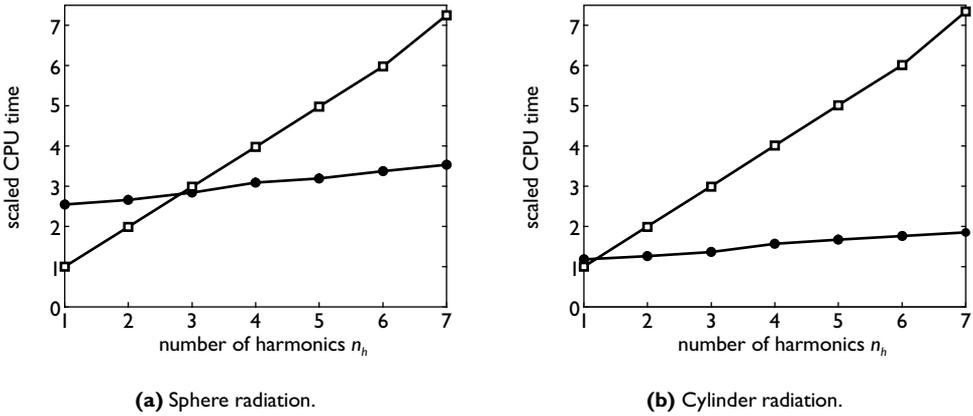
**figure 3.3** Scaled computation times for Fourier BEM calculations, with increasing number of harmonics $n_h$ in the boundary conditions, computed with different integration algorithms in circumferential direction (derived from Kuijpers et al. [1997]). —□— : Gauss integration; —●— : FFT integration.

number of Fourier points $n_{FFT}$ for the integrals to converge where the relative error in the computed value for the integrals did not exceed $10^{-3}$. These pairs of $c_s$, $c_o$ and related $n_{FFT}$ were then used in a curve-fitting procedure to obtain the relationship

$$n_{FFT}(c_s, c_o) = 14 \left( c_s + \frac{c_o}{2\pi} \right)^{0.9} .$$

In the BEM code the expression for $n_{FFT}$ was implemented and its value is computed for each circumferential integral evaluation separately based on values for $c_s$ and $c_o$ for that integral. Its value is rounded to the nearest subsequent power of 2, to enable the use of a fast radix-2 FFT algorithm. In Kuijpers et al. [1997], it is shown that this method was in general more efficient than 'traditional' Gauss-Legendre integral evaluation for problems with more than one Fourier harmonic: For Gauss-Legendre integration the characteristic total CPU time is the computation time per harmonic multiplied by the number of harmonics, while for the FFT base algorithm the total CPU time is the (somewhat larger) computation time for *one* harmonic (see figure 3.3). For comparison, similar calculations with a 3-dimensional BEM code [Sysnoise, 1996] would yield a computation time which is at least 50 times larger, but is independent of the number of harmonics.

### 3.3.2  Handling the non-uniqueness problem

Besides the integral evaluations, another important issue in the implementation of a BEM formulation is the non-uniqueness problem. The non-uniqueness problem is the well-known failure of certain integral equations, when applied to exterior radiation problems, to yield a unique solution at certain characteristic (eigen)frequencies of the interior acoustic problem. Schenck [1968] proposed a method to remove this problem by adding some additional Kirchhoff-Helmholtz equations that are evaluated in the interior domain. This method, known as the CHIEF (Combined Helmholtz Integral Equation Formulation) leads to an overdetermined system of equations for the surface pressures. A potential problem with the CHIEF method is the choice of the location of the points in the interior domain

for the additional equations. For the method to be effective, it is important for the interior points, not to be on a nodal surface of the interior eigenmode. However, in practice this seldomly proves to be a problem [Seybert and Rengarajan, 1987; Benthien and Schenck, 1997].

Another method to remove the non-uniqueness problem is the so-called Burton-Miller approach. Burton and Miller [1971] introduced an acoustic integral equation that was valid for all wavenumbers by forming a linear combination of the Kirchhoff-Helmholtz integral equation and its normal derivative. A major problem with this formulation is the occurrence of hypersingular integrals in the formulation which have to be treated with special integration algorithms. It should be noted that with this approach the number of system matrices for the discretization is doubled. Akyol [1986] and Wang et al. [1997] have successfully implemented Fourier BEM formulations with this approach.

In the Fourier BEM method that is presented here, the CHIEF method was chosen for two reasons. Firstly, the implementation of the method is trivial compared to the implementation of the Burton-Miller approach. Secondly, and more important, the CHIEF method is numerically much more efficient than the Burton-Miller approach. The Burton-Miller approach requires assembling twice as much complete system matrices, and since the assembly time is critical in most BEM formulations this will in practice double the computational effort. Using the CHIEF method means that a few more system equations are added and that a least-squares solution of the overdetermined system of equations should be computed. This augments the computation times for the normal Fourier BEM formulation only minimally.

### 3.3.3 Discretization process

The boundary element method is applied for the discretization of the modified Kirchhoff-Helmholtz integral equations (3.30) and (3.31) as follows. Assume that the generator $L$ of body $B$ can be discretized with $n_e$ line elements and that each line element $i_e$ has $n_n$ nodes. The total number of nodes is denoted as $n_{nd}$. Thus the coordinates $r$ and $z$ can be expressed in terms of the coordinates $r_{i_n}$ and $z_{i_n}$ of element node $i_n$ using a piecewise polynomial approximation:

$$r(\xi) = \sum_{i_n=1}^{n_n} \phi_{i_n}^{n_n}(\xi) r_{i_n}, \qquad z(\xi) = \sum_{i_n=1}^{n_n} \phi_{i_n}^{n_n}(\xi) z_{i_n}, \tag{3.38}$$

where $\phi_{i_n}^{n_n}(\xi)$ are the $(n_n - 1)$th order shape functions, $\xi$ is the local element coordinate and $i_n$ is the local node number. The isoparametric approach was chosen, so the boundary variables $p_m^s$, $p_m^c$, $v_m^s$, and $v_m^c$ are also approximated using the same shape functions as for the coordinates. Thus, on element $i_e$,

$$\gamma_{i_e}(\xi) = \sum_{i_n=1}^{n_n} \phi_{i_n}^{n_n}(\xi) \gamma_{i_e\,i_n}, \tag{3.39}$$

where any of the boundary variables can be substituted for $\gamma_{i_e}(\xi)$, and $\gamma_{i_e\,i_n}$ is the value of the corresponding variable on local node $i_n$ of element $i_e$. Using this approximation in, for

instance, equation (3.30), yields

$$C(\boldsymbol{x})p_m^s(\boldsymbol{x}) = \sum_{i_e=1}^{n_e}\left\{\sum_{i_n=1}^{n_n} p_{m\,i_e\,i_n}^s \int_{-1}^{1} \phi_{i_n}^{n_n}(\xi)H_m'(\xi)r(\xi)J_{i_e}(\xi)\,\mathrm{d}\xi \right.$$

$$\left. + \mathrm{i}k\rho_0 c_0 \sum_{i_n=1}^{n_n} v_{m\,i_e\,i_n}^s \int_{-1}^{1} \phi_{i_n}^{n_n}(\xi)H_m(\xi)r(\xi)J_{i_e}(\xi)\,\mathrm{d}\xi \right\}, \qquad (3.40)$$

where $p_{m\,i_e\,i_n}^s$ is the value of $p_m^s$ at local node $i_n$ of element $i_e$ and $J_{i_e}(\xi)$ the Jacobian of the transformations given by equation (3.38), for element $i_e$:

$$J_{i_e}(\xi) = \left[ \left(\frac{\mathrm{d}r}{\mathrm{d}\xi}\right)^2 + \left(\frac{\mathrm{d}z}{\mathrm{d}\xi}\right)^2 \right]^{\frac{1}{2}}. \qquad (3.41)$$

Expressions similar to equation (3.40) can be obtained for the other boundary values using equation (3.31).

For the solution process, a collocation scheme is applied. The observer points $\boldsymbol{x}$ on the boundary are chosen successively to coincide with each global node $i_{nd}$ and $\boldsymbol{y}$ is the (surface) point of integration, now explicitly a function of $\xi$ through equation (3.38). This collocation method results in a set of $n_{nd}$ linear algebraic equations in terms of the unknown $p_m$, when $v_m$ is given on each node, and vice versa. The resulting equations may be written in the following matrix form:

$$\boldsymbol{A}_m\boldsymbol{p}_m^s = \boldsymbol{B}_m\boldsymbol{v}_m^s, \qquad (3.42)$$

where $\boldsymbol{p}_m^s$ and $\boldsymbol{v}_m^s$ are the column vectors containing the $n_{nd}$ nodal values of $p_m^s$ and $v_m^s$, respectively. $\boldsymbol{A}_m$ and $\boldsymbol{B}_m$ are square matrices with the various integrals as in equation (3.40) as their elements. For the cosine terms of the Fourier series, a similar matrix equation can be derived:

$$\boldsymbol{A}_m\boldsymbol{p}_m^c = \boldsymbol{B}_m\boldsymbol{v}_m^c, \qquad (3.43)$$

where $\boldsymbol{p}_m^c$ and $\boldsymbol{v}_m^c$ are the column vectors containing the $n_{nd}$ nodal values of $p_m^c$ and $v_m^c$. Thus, two matrix equations result, relating the terms of the Fourier expansion of the unknown variables to the Fourier coefficients of the boundary conditions. The matrix equations that describe the acoustic radiation have to be formed for every Fourier harmonic number $m$ that is present in the Fourier expansion of the boundary conditions.

When the solution for all boundary values is computed, the value of the Fourier terms of the pressure and its derivative for any surface or exterior point can easily be obtained by applying an equation similar to equation (3.40) for $p_m^{s,\circ}$, and $p_m^{c,\circ}$, substituting the calculated values for $p_{m\,i_e\,i_n}^s$, $p_{m\,i_e\,i_n}^c$, $v_{m\,i_e\,i_n}^s$ and $v_{m\,i_e\,i_n}^c$. The resulting equation is an explicit relationship between the acoustic variables on the surface of the radiating body and the acoustic variables at any other position in the acoustic medium.

## 3.4    Summary

An improved formulation for acoustic boundary element analysis with Fourier elements was presented. In this formulation, that can be used for axisymmetric geometries with non-axisymmetric boundary conditions, the dependence of the acoustic variables in circumferential direction is described with Fourier series expansions. In this way, the dimensionality of the problem is reduced by one.

The novelty in the formulation is the way that the Fourier integrals of the kernel functions are handled. In the formulation that was proposed here, this is done with an integration algorithm which deploys efficient fast Fourier transform routines. The efficiency of this approach compared to other Fourier BEM formulations is especially apparent when complex boundary conditions with more than one Fourier harmonic are imposed. With the fast Fourier transform integration algorithm the speedup factor of at least 50, for Fourier BEM compared to 3-dimensional BEM can be maintained irrespective of the number of Fourier harmonics in the boundary condition Fourier series.

Other important implementation aspects of any BEM method are the computation of (nearly) singular integrals and the handling of the non-uniqueness problem for exterior radiation problems. In the formulation that was proposed here, these are handled with Gauss-Log integration and the CHIEF method, respectively. The complete Fourier BEM formulation that was presented here was implemented in the acoustic code b*Ard* [1998]. The application of the Fourier BEM formulation to analyze the acoustics of various MRI scanner models will be shown in chapters 5 and 6.

# 4 The radiation modes formulation for subsystems

## 4.1 Introduction

The radiation modes formulation is a rather new technique to characterize structural vibrations from an acoustical perspective. The radiation modes formulation is a technique to determine a unique basis for the vibrations of a structure, which is orthonormal with respect to the acoustically radiated power. The basis functions of this velocity basis are called the radiation modes. Compared with the structural modes, well-known from the structural dynamics field, some fundamental differences exist. Unlike structural modes, the radiation modes do not depend on the structural behavior of a structure, but only on the geometry and on the frequency. The radiation modes contribute independently to the total sound power. Furthermore, with the radiation modes formulation, it is quite simple to decompose the vibration field into efficiently radiating and non-radiating (evanescent) components. Hence, the radiation modes can offer valuable insights for the acoustic engineer.

In the literature, the introduction of the radiation modes concept dates from the beginning of this decade. Borgiotti [1990] and Photiadis [1990] showed that an orthonormal basis of the surface normal velocity can be found by singular value decomposition (SVD) of a quadratic expression for the radiated power and also by SVD of a radiation operator which relates surface vibration to far field pressure. The individual modes of the orthonormal basis resulting from the SVD were called 'singular velocity patterns' or 'surface velocity filters'. Their corresponding singular values were shown to be directly related to the radiation efficiency. In this way, the surface velocity field can be easily divided into radiating and non-radiating components. Sarkissian [1991] showed that the same modes can be found by an eigenvalue analysis of the real part of the surface impedance operator. Cunefare [1991] derived a modal representation from the expression for radiation efficiency and showed the analogy of this representation with the Rayleigh quotient in structural dynamics. In subsequent articles [Cunefare and Currey, 1994; Currey and Cunefare, 1995], the eigenvectors of the basis were called 'radiation modes' and their bounding, convergence and sensitivity characteristics were investigated. Later, Chen and Ginsberg [1995] introduced yet another form of 'radiation modes', derived from the complex power expression. These modes incorporate more elegantly the surface interaction mechanism between surface pressure and normal velocity and are therefore well suited for structures submerged in heavy acoustic fluids.

Examples of the application of the radiation modes concept can be found in the field of acoustic holography [Borgiotti, 1990; Photiadis, 1990; Sarkissian, 1991], acoustic design

sensitivity and optimization [Naghshineh et al., 1992; Shephard and Cunefare, 1997], coupled structural-acoustic modeling [Chen and Ginsberg, 1995; Chen, 1997], and in the field of active structural-acoustic control (ASAC) [Baumann et al., 1992; Elliott and Johnson, 1993; Naghshineh and Koopmann, 1993; Borgiotti and Jones, 1994; Naghshineh et al., 1998]. These papers have in common, that they offer a unique perspective on the radiation characteristics of structures, much like the vibration eigenmodes in the structural dynamics field.

In this thesis, the radiation modes formulation is enhanced to enable the determination of the radiation modes of acoustic systems with partly passive boundary conditions (e.g. a partly rigid surface). The resulting radiation modes formulation for subsystems is not only used to increase the insight into the acoustic radiation of a structure, but also as a 'black box' reduction technique for numerical acoustics, which is especially valuable in an acoustic design optimization environment.

## 4.2   Theory of radiation modes

### 4.2.1   Radiation modes formulation

Consider a structure that is radiating sound into free space due to a harmonically vibrating surface $S$. The acoustic pressure $\tilde{p}$ and velocity $\tilde{u}$ for any point $x_S$ at surface $S$ can then be expressed as

$$\tilde{p}(x_S, t) = \mathrm{Re}\left[p(x_S, \omega)e^{i\omega t}\right], \quad \tilde{u}(x_S, t) = \mathrm{Re}\left[u(x_S, \omega)e^{i\omega t}\right], \tag{4.1}$$

with $\omega$ as the angular frequency of the excitation. This acoustic pressure field has to satisfy the Helmholtz equation (see equation (2.5)),

$$\nabla^2 p + k^2 p = 0, \tag{4.2}$$

with free field wavenumber $k = \omega/c_0$. The structure is also subject to a normal velocity boundary condition at its surface,

$$u \cdot n \equiv v = \eta, \tag{4.3}$$

with $n$ the surface normal, $v$ the surface normal component of $u$, and $\eta$ the given surface velocity boundary condition.

Regardless of the acoustic analysis method, the relationship between surface pressure $p$ and normal velocity $v$ can be expressed with a complex linear operator form as

$$\mathcal{L}_p(p) = \mathcal{L}_v(v). \tag{4.4}$$

To compute the time-averaged power radiated by the structure, the time-averaged acoustic normal intensity $\bar{I} \cdot n$ has to be integrated over surface $S$,

$$\bar{P} = \int_S \bar{I} \cdot n \, dS, \tag{4.5}$$

with $\bar{I} = p\,u^*$ as the acoustic energy flux vector, and where $*$ denotes the complex conjugate. The bar notation $^-$ denotes the time average. Using the definition for the

normal velocity (4.3), the time-averaged radiated acoustic power can be expressed as

$$\bar{P} = \frac{1}{2} \operatorname{Re} \int_S pv^* dS. \tag{4.6}$$

The acoustic pressure $p$ can be solved from equation (4.4) and substituted in the power relation (4.6) to obtain

$$\bar{P} = \frac{1}{2} \operatorname{Re} \int_S \mathcal{L}_p^{-1} \mathcal{L}_v(v) v^* dS. \tag{4.7}$$

It is common in acoustic analysis methods that the acoustic quantities at the surface of the radiating structure are written as a sum of preselected basis functions, which are denoted in vector form as $\boldsymbol{\phi} = [\phi_1, \phi_2, \ldots, \phi_j, \ldots]^{\mathsf{T}}$. With use of so-called generalized degrees of freedom for the pressure $\boldsymbol{p} = [p_1, p_2, \ldots, p_j, \ldots]^{\mathsf{T}}$, and normal velocity $\boldsymbol{v} = [v_1, v_2, \ldots, v_j, \ldots]^{\mathsf{T}}$, the pressure and normal velocity can be discretized as

$$p(\boldsymbol{x}_S) = \sum_j \phi_j(\boldsymbol{r}_s) p_j = \boldsymbol{\phi}^{\mathsf{T}} \boldsymbol{p}, \tag{4.8}$$

$$v(\boldsymbol{x}_S) = \sum_j \phi_j(\boldsymbol{r}_s) v_j = \boldsymbol{\phi}^{\mathsf{T}} \boldsymbol{v}. \tag{4.9}$$

With this series expansion, the relation between pressure and normal velocity (4.4) can be written in discretized form as

$$\boldsymbol{A}\boldsymbol{p} = \boldsymbol{B}\boldsymbol{v}. \tag{4.10}$$

The expression for the radiated acoustic power (4.6) can also be discretized,

$$\bar{P} = \frac{1}{2} \operatorname{Re} \int_S \boldsymbol{p}^{\mathsf{T}} \boldsymbol{\phi} \boldsymbol{\phi}^{\mathsf{T}} \boldsymbol{v}^* dS$$

$$= \frac{1}{2} \operatorname{Re} \left[ \boldsymbol{p}^{\mathsf{T}} \boldsymbol{N} \boldsymbol{v}^* \right]. \tag{4.11}$$

The discretization of the operator expression for the radiated acoustic power leads to

$$\bar{P} = \frac{1}{2} \operatorname{Re} \int_S \boldsymbol{v}^{\mathsf{T}} \mathcal{L}_p^{-1} \mathcal{L}_v(\boldsymbol{\phi}) \boldsymbol{\phi}^{\mathsf{T}} \boldsymbol{v}^* dS$$

$$= \frac{1}{2} \operatorname{Re} \left[ \boldsymbol{v}^{\mathsf{T}} (\boldsymbol{A}^{-1} \boldsymbol{B})^{\mathsf{T}} \boldsymbol{N} \boldsymbol{v}^* \right] = \frac{1}{2} \operatorname{Re} \left[ \boldsymbol{v}^{\mathsf{T}} \boldsymbol{Z} \boldsymbol{v}^* \right]. \tag{4.12}$$

The properties of the complex power coupling matrix $\boldsymbol{Z}$ can be understood by using the reciprocity principle [Pierce, 1981; Kinsler et al., 1982]. Considering two acoustic fields, denoted by the subscripts $a$ and $b$, that result from differing vibrations of the structure, the reciprocity principle,

$$\nabla \cdot (p_a \boldsymbol{u}_b - p_b \boldsymbol{u}_a) = 0, \tag{4.13}$$

integrated over the structure's volume $V$, after application of Gauss' theorem yields

$$\int_S (p_a \boldsymbol{u}_b - p_b \boldsymbol{u}_a) \cdot \boldsymbol{n} \, dS = 0. \tag{4.14}$$

Using the operator expression (4.4) for $p$, the reciprocity principle can be rewritten as

$$\int_S \mathcal{L}_p^{-1} \mathcal{L}_v(v_a) v_b dS = \int_S \mathcal{L}_p^{-1} \mathcal{L}_v(v_b) v_a dS, \tag{4.15}$$

or in discretized form,

$$\boldsymbol{v}_a^\mathsf{T} \boldsymbol{Z} \boldsymbol{v}_b = \boldsymbol{v}_b^\mathsf{T} \boldsymbol{Z} \boldsymbol{v}_a. \tag{4.16}$$

This implies that $\boldsymbol{Z}$ is symmetric. Because of the symmetry property of $\boldsymbol{Z}$, only its real part contributes to the radiated acoustic power. This is illustrated by the following derivation adapted from Chen and Ginsberg [1995]. The complex power coupling matrix can be split up in a real part $\boldsymbol{C}$ and an imaginary part $\boldsymbol{D}$,

$$\boldsymbol{Z} = \boldsymbol{C} + i\boldsymbol{D}, \tag{4.17}$$

where both $\boldsymbol{C}$ and $\boldsymbol{D}$ are real symmetric matrices. With these, the complex power $\bar{P}_c$ and its complex conjugate $\bar{P}_c^*$ can be computed,

$$\bar{P}_c = \frac{1}{2}\boldsymbol{v}^\mathsf{T} \boldsymbol{C} \boldsymbol{v}^* + \frac{i}{2}\boldsymbol{v}^\mathsf{T} \boldsymbol{D} \boldsymbol{v}^*, \qquad \bar{P}_c^* = \frac{1}{2}\boldsymbol{v}^\mathsf{T} \boldsymbol{C} \boldsymbol{v}^* - \frac{i}{2}\boldsymbol{v}^\mathsf{T} \boldsymbol{D} \boldsymbol{v}^*. \tag{4.18}$$

The radiated acoustic power can be computed with

$$\bar{P} = \mathrm{Re}(\bar{P}_c) = \frac{1}{2}(\bar{P}_c + \bar{P}_c^*) = \frac{1}{2}\boldsymbol{v}^\mathsf{T} \boldsymbol{C} \boldsymbol{v}^*, \tag{4.19}$$

which shows that the quadratic sum described by each part is a real value, and that only the real part of the matrix $\boldsymbol{Z}$ contributes to the radiated power. With this knowledge, equation (4.12) can be rewritten as

$$\bar{P} = \frac{1}{2}\boldsymbol{v}^\mathsf{T} \mathrm{Re}\left[(\boldsymbol{A}^{-1}\boldsymbol{B})^\mathsf{T}\boldsymbol{N}\right]\boldsymbol{v}^* = \frac{1}{2}\boldsymbol{v}^\mathsf{T} \boldsymbol{C} \boldsymbol{v}^*. \tag{4.20}$$

Matrix $\boldsymbol{C}$ may be interpreted as a power coupling matrix between individual elements of $\boldsymbol{v}$, and because the radiated power is always a positive quantity, matrix $\boldsymbol{C}$ is positive definite.

An important acoustic characteristic of a radiating source is its radiation efficiency. The radiation efficiency $\sigma$ of an acoustic source is defined as the ratio of the power per unit area radiated by the source, and the power radiated by a reference source radiating plane waves; e.g. an infinite plate, vibrating uniformly with the same mean square velocity as the source,

$$\sigma \equiv \frac{\bar{P}/S}{\rho_0 c_0 \langle \overline{v^2} \rangle}, \tag{4.21}$$

where $\bar{P}/S$ is the power per unit area radiated by the source and $\rho_0 c_0 \langle v^2 \rangle$ is the power per unit area radiated by the reference source. The $\langle \ \rangle$ notation represents the spatial average of a quantity, i.e.,

$$\langle \gamma \rangle = \frac{1}{S} \int_S \gamma \, dS. \tag{4.22}$$

Since the radiation efficiency is not strictly defined as the ratio of in- and outgoing energies, its value can exceed one. Using the discretized form for pressure and normal velocity, equation (4.21) can be written as

$$\sigma = \frac{1}{\rho_0 c_0} \frac{\text{Re}\left[\boldsymbol{p}^\mathsf{T} \boldsymbol{N} \boldsymbol{v}^*\right]}{\text{Re}\left[\boldsymbol{v}^\mathsf{T} \boldsymbol{N} \boldsymbol{v}^*\right]} = \frac{1}{\rho_0 c_0} \frac{\boldsymbol{v}^\mathsf{H} \boldsymbol{C} \boldsymbol{v}}{\boldsymbol{v}^\mathsf{H} \boldsymbol{N} \boldsymbol{v}}. \tag{4.23}$$

The expression obtained in this way has quadratic forms in its numerator and denominator. It can be interpreted as a Rayleigh quotient for the generalized eigenvalue problem

$$\boldsymbol{C} \boldsymbol{v} = \lambda \boldsymbol{N} \boldsymbol{v}, \text{ with } \sigma = \lambda/(\rho_0 c_0). \tag{4.24}$$

The generalized eigenvalue problem (4.24) yields real eigenvalues $\lambda_k$ and real eigenvectors $\boldsymbol{\psi}_k$. The corresponding eigenfunctions

$$\psi_k(\boldsymbol{x}_S) = \sum_j \phi_j(\boldsymbol{r}_s) \psi_{jk} = \boldsymbol{\phi}^\mathsf{T} \boldsymbol{\psi}_k, \tag{4.25}$$

are called (velocity) radiation modes and their eigenvalues, divided by the specific acoustic impedance $z_0 = \rho_0 c_0$ are their radiation efficiencies,

$$\sigma_k = \frac{\lambda_k}{z_0}. \tag{4.26}$$

The eigenvalues and eigenvectors are real because the matrices $\boldsymbol{C}$ and $\boldsymbol{N}$ are real and symmetric. It is customary to normalize the eigenvectors with respect to the matrix $\boldsymbol{N}$, which results in

$$\boldsymbol{\Psi}^\mathsf{H} \boldsymbol{N} \boldsymbol{\Psi} = \boldsymbol{I}, \qquad \boldsymbol{\Psi}^\mathsf{H} \boldsymbol{C} \boldsymbol{\Psi} = \boldsymbol{\Lambda} \tag{4.27}$$

with $\boldsymbol{\Psi} = [\boldsymbol{\psi}_1, \ \boldsymbol{\psi}_2, \ \dots \ \boldsymbol{\psi}_k, \ \dots]$, $\boldsymbol{\Lambda}$ a diagonal matrix of the eigenvalues, and $\boldsymbol{I}$ as the identity matrix.

The radiation modes simultaneously diagonalize the radiated acoustic power of the regarded source and the reference source. Because the matrices $\boldsymbol{C}$ and $\boldsymbol{N}$ are only dependent on frequency and the geometry of the radiating surface, the radiation modes are only dependent on those properties; they do not depend on the structural behavior of the radiator.

The set of radiation modes $\psi_k(\boldsymbol{r}_s)$ can serve as a basis for the normal velocity distribution $v(\boldsymbol{r}_s)$. The generalized degrees of freedom $\boldsymbol{v}$ of this velocity distribution $v(\boldsymbol{r}_s)$ can be written as a superposition of the generalized degrees of freedom of the radiation modes such that

$$\boldsymbol{v} = \sum_k \boldsymbol{\psi}_k \zeta_k = \boldsymbol{\Psi} \boldsymbol{\zeta}. \tag{4.28}$$

The velocity distribution can then be written as

$$v(\mathbf{r}_s) = \sum_k \zeta_k \psi_k(\mathbf{r}_s) = \sum_k \sum_j \phi_j(\mathbf{r}_s) \psi_{jk} \zeta_k = \boldsymbol{\phi}^{\mathsf{T}} \boldsymbol{\Psi} \boldsymbol{\zeta}. \tag{4.29}$$

The vector of modal contribution coefficients $\boldsymbol{\zeta}$ can be computed from equation (4.28) by pre-multiplying this equation with $\boldsymbol{\Psi}^{\mathsf{H}} \mathbf{N}$ and using the orthogonality property for the eigenvectors from equation (4.27),

$$\boldsymbol{\zeta} = \boldsymbol{\Psi}^{\mathsf{H}} \mathbf{N} \mathbf{v}. \tag{4.30}$$

With these modal contribution coefficients $\boldsymbol{\zeta}$, computation of the radiated acoustic power becomes trivial,

$$\bar{P} = \frac{1}{2} \sum_k z_0 \sigma_k \zeta_k^* \zeta_k = \frac{1}{2} \boldsymbol{\zeta}^{\mathsf{H}} \boldsymbol{\Lambda} \boldsymbol{\zeta}. \tag{4.31}$$

The advantages of the radiation modes are evident. Because the radiation modes are the velocity basis functions that orthogonalize the quadratic power expression, equation (4.20), they contribute independently to the radiated power. The velocity distribution can be decomposed in radiation modes with equation (4.30) and the power contribution of each mode is expressed through equation (4.31). The radiation modes only depend on the geometry of the acoustic domain, not on the structural properties of the structural domain. Thus, when the structural properties change, without changing the acoustic domain, the results of the radiation modes analysis can be reused, without the need for an additional full acoustic analysis. This property of the radiation modes formulation will be used in section 4.3 for the development of an acoustic reduction technique.

### 4.2.2  Radiation modes for subsystems

With the radiation modes formulation, independently radiating velocity patterns are identified for the complete acoustic domain, without incorporating its boundary conditions. However, sometimes one is interested in the radiation modes of a part of the total acoustic domain only. When for instance it is known, prior to any structural-acoustic computations, that a (large) part of the acoustic boundary is rigid, then the radiation modes should also be rigid on that part of the boundary. In that case, only the radiation modes of the non-rigid part of the acoustic boundary are of interest. These can be computed as follows.

Consider the quadratic power expression for an acoustic system with prescribed velocity boundary conditions at part 1 of the acoustic boundary and a priori unknown boundary conditions at part 2 of the boundary. Then, partitioning the quadratic power expression for the degrees of freedom for parts 1 and 2 of the boundary yields

$$\bar{P} = \frac{1}{2} \begin{bmatrix} \mathbf{v}_1^{\mathsf{H}} & \mathbf{v}_2^{\mathsf{H}} \end{bmatrix} \begin{bmatrix} \mathbf{C}_{11} & \mathbf{C}_{12} \\ \mathbf{C}_{21} & \mathbf{C}_{22} \end{bmatrix} \begin{bmatrix} \mathbf{v}_1 \\ \mathbf{v}_2 \end{bmatrix}, \tag{4.32}$$

or (using $\mathbf{C}_{21} = \mathbf{C}_{12}^{\mathsf{H}} = \mathbf{C}_{12}^{\mathsf{T}}$)

$$\bar{P} = \frac{1}{2} \mathbf{v}_1^{\mathsf{H}} \mathbf{C}_{11} \mathbf{v}_1 + \mathbf{v}_2^{\mathsf{H}} \mathbf{C}_{21} \mathbf{v}_1 + \frac{1}{2} \mathbf{v}_2^{\mathsf{H}} \mathbf{C}_{22} \mathbf{v}_2. \tag{4.33}$$

When part 2 of the boundary is rigid, then $\mathbf{v}_2 = \mathbf{0}$, and the power expression simplifies to

$$\bar{P} = \frac{1}{2}\mathbf{v}_1^H \mathbf{C}_{11}\mathbf{v}_1, \tag{4.34}$$

for which eigenvalue problem (4.24) can be solved with submatrices $\mathbf{C}_{11}$ and $\mathbf{N}_{11}$. When, in general, an impedance boundary condition of the form

$$\mathbf{p}_2 = \mathbf{Y}\mathbf{v}_2, \tag{4.35}$$

holds for part 2 of the boundary, then the power expression can also be written explicitly for $\mathbf{v}_1$. Similar to the power expression, the system equations can be partitioned,

$$\begin{bmatrix} \mathbf{p}_1 \\ \mathbf{p}_2 \end{bmatrix} = \begin{bmatrix} \mathbf{R}_{11} & \mathbf{R}_{12} \\ \mathbf{R}_{21} & \mathbf{R}_{22} \end{bmatrix} \begin{bmatrix} \mathbf{v}_1 \\ \mathbf{v}_2 \end{bmatrix}, \tag{4.36}$$

with matrix $\mathbf{R} = \mathbf{A}^{-1}\mathbf{B}$. This matrix is already computed as a part of the computation of matrix $\mathbf{C} = \mathrm{Re}[(\mathbf{A}^{-1}\mathbf{B})^T\mathbf{N}]$. With help of this relationship, the velocities at boundary 2 can be written as

$$\mathbf{v}_2 = \mathbf{H}\mathbf{v}_1, \qquad \text{with } \mathbf{H} = (\mathbf{Y} - \mathbf{R}_{22})^{-1}\mathbf{R}_{21}, \tag{4.37}$$

and the resulting power expression becomes

$$\bar{P} = \frac{1}{2}\mathbf{v}_1^H \mathbf{C}_{11}'\mathbf{v}_1, \qquad \text{with } \mathbf{C}_{11}' = \mathbf{C}_{11} + 2\mathbf{H}^H\mathbf{C}_{21} + \mathbf{H}^H\mathbf{C}_{22}\mathbf{H}. \tag{4.38}$$

Again the eigenvalue problem (4.24) can be solved, now with submatrices $\mathbf{C}_{11}'$ and $\mathbf{N}_{11}$. The rigid wall condition for boundary 2 is a special case where of this general form with $\mathbf{C}_{11}'$ where $\mathbf{H} = \mathbf{0}$.

## 4.3   Radiation modes reduction technique

The generalized eigenvalue problem of the real, symmetric matrices $\mathbf{C}$ and $\mathbf{N}$, both of dimension $(N \times N)$, in equation (4.24) yields $N$ real eigenvalues, ordered as $\lambda_1 > \lambda_2 > \ldots > \lambda_N$, and $N$ orthonormal real eigenvectors. This means that the eigenvector that should converge first in for instance a power iteration, corresponds to the largest eigenvalue and hence largest radiation efficiency. Following converging eigenvectors have smaller eigenvalues/efficiencies. Borgiotti [1990] and later Cunefare [1991] found that in the low frequency range, the radiation efficiencies fall off very rapidly with increasing mode order. This usually means that only the first few radiation modes contribute to the radiated power. The other radiation modes correspond to evanescent acoustic fields which do not radiate into the far field. This is why radiation modes are also known as surface velocity filters: they filter the vibration distribution on the radiating surface and only pass the efficiently radiating components into the far field [Elliott and Johnson, 1993]. The power radiation of the vibrating structure can be described accurately with only a limited number of (efficient) radiation modes. This property is often used to compute the power radiation in active structural-acoustic control (ASAC) schemes [Baumann et al., 1992; Naghshineh and Koopmann, 1993; Elliott and Johnson, 1993; Borgiotti and Jones, 1994].

The filtering property of radiation modes can be used in a reduction technique for the acoustic power radiation of vibrating structures. The power radiation can be described with a few radiation modes rather that with a full power coupling matrix $\mathbf{C}$. If the boundary conditions of the radiation problem are changed, without changing the structure's radiating geometry, then the power radiation can be quickly evaluated using equations (4.30) and (4.31) with truncated radiation modes matrix $\mathbf{\Psi}$ containing only those modes which contribute to the power. In practice this truncation can be made by comparing the efficiencies of the radiation modes and using a truncation criterion $c_t$,

$$10 \log_{10}(\sigma_1) - 10 \log_{10}(\sigma_{k_t}) > c_t, \tag{4.39}$$

i.e., the matrix $\mathbf{\Psi}$ is truncated at radiation mode index $k_t$ for which the radiation efficiency $\sigma_{k_t}$ is more than $c_t$ dB smaller than the efficiency of the first (modes efficient) radiation mode. For practical applications a value for $c_t$ of about 30 dB is a realistic criterion. However, one should be aware that the radiation efficiency does not alone determine the radiated power. The contribution coefficients $\zeta$ are present quadratically in the power equation (4.31). So, the contribution coefficients of the least efficient modes should not be more than about 15 dB higher than the contribution coefficients of the more efficient modes.

The error that is made by not incorporating the power contribution of the radiation modes that were truncated can be computed easily. For that, first the remainder of the velocity distribution should be calculated. Let $\mathbf{\Psi}_t$ be the truncated radiation modes matrix, and $\zeta_t$ the truncated contribution coefficient vector, then the residual velocity field $\mathbf{v}_r$ that is not described by the truncated series of radiation modes equals

$$\mathbf{v}_r = \mathbf{v} - \sum_{k=1}^{k_t} \zeta_k \psi_k = \mathbf{v} - \mathbf{\Psi}_t \zeta_t. \tag{4.40}$$

The power truncation error $e_{\bar{p}}$ is then limited by the product of the spatially-averaged and time-averaged squared residual velocity vector $\mathbf{v}_r$ and the lowest radiation efficiency of the radiation modes in $\mathbf{\Psi}_t$,

$$\begin{aligned} e_{\bar{p}} &< z_0 \sigma_{k_t} S \langle \overline{v_r^2} \rangle \\ &< z_0 \sigma_{k_t} \mathbf{v}_r^{\mathrm{H}} \mathbf{N} \mathbf{v}_r. \end{aligned} \tag{4.41}$$

This equation enables an accurate estimation of the maximum error that is made when the radiation modes reduction technique is used.

The implementation of the radiation modes reduction technique in a structural-acoustic design environment is displayed in figure 4.1. This shows that a complete acoustic analysis only has to be performed once for every new geometry of the acoustic domain. When the acoustic geometry remains unchanged, the radiation mode results of a previous analysis can be used. To be able to use the reduction technique effectively, only the significant radiation modes and their efficiencies need to be stored for every frequency that is used in subsequent analyses with different boundary conditions, not the whole matrix $\mathbf{C}$. To compute the contribution coefficients $\zeta$, the matrix $\mathbf{N}$ also needs to be stored, but fortunately this matrix is independent of the frequency. Because the number of significant radiation modes increases with increasing wavenumber [Elliott and Johnson, 1993], it may
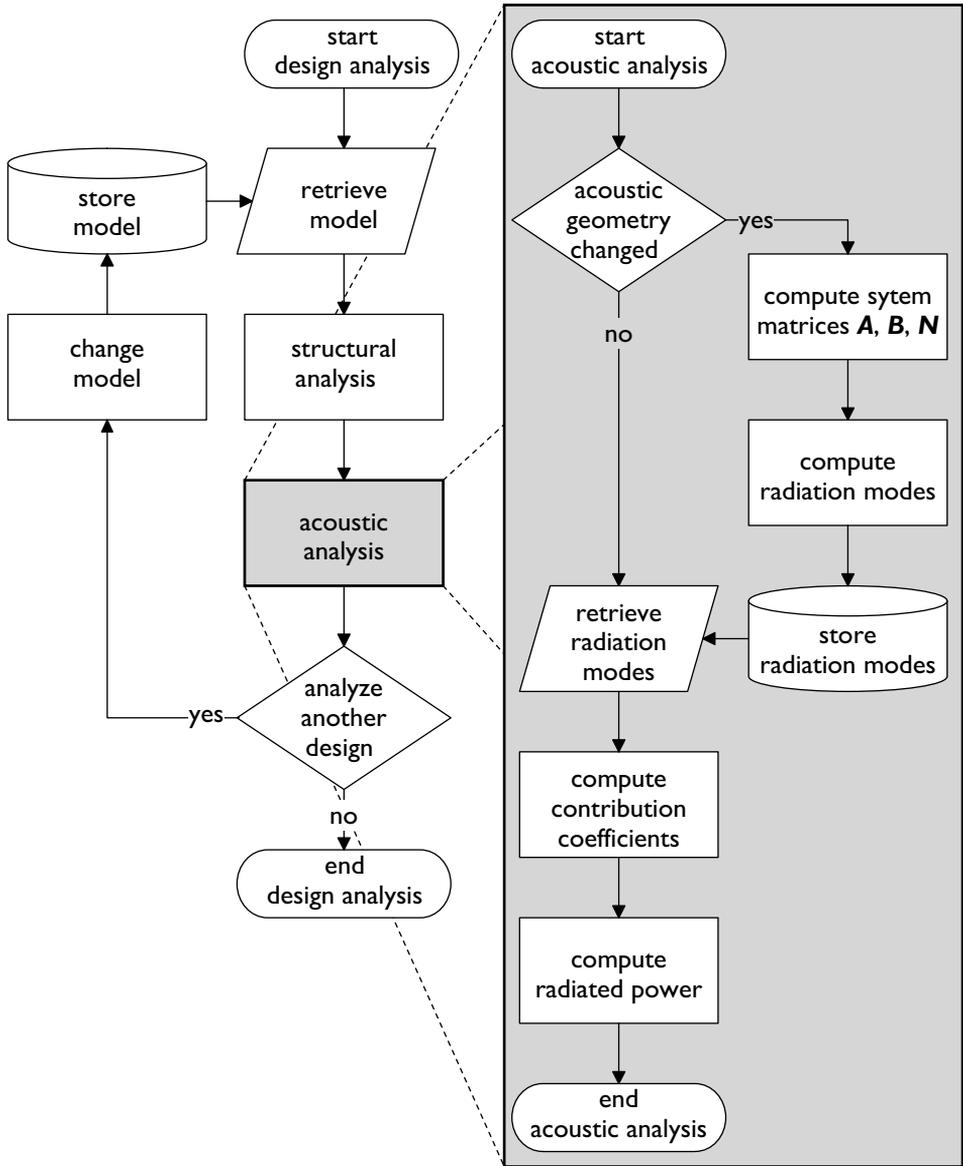
**figure 4.1** Flow chart of the implementation of the radiation modes reduction technique in a structural-acoustic design environment.

be unrewarding to use this radiation modes technique in the very high frequency domain. However, for the applications presented in this thesis, this is not the case (see chapters 5 and 6).

## 4.4  Summary

The general formulation of the radiation modes of an acoustic system was presented. With the radiation modes formulation a unique orthonormal basis for the surface velocity can be obtained. This basis is orthonormal with respect to the radiated acoustic power: it diagonalizes the quadratic power expression. As such it determines a velocity basis for which each of the basis functions, the so-called radiation modes, contributes independently to the radiated power.

The radiation modes that are found with the general radiation modes formulation are velocity patterns for the whole acoustic domain. Often only a part of the acoustic system is excited, while the remainder of the acoustic domain is passive. Such system knowledge can be introduced in the radiation modes formulation by using the radiation modes formulation for subsystems that was developed in this thesis.

The radiation modes formulation can also be used as an acoustic model reduction technique, to speed up the acoustic analysis part in a structural-acoustic design environment. A technique was outlined in which only the most efficient radiation modes for an acoustic geometry are stored and can be reused to compute the radiated acoustic power in subsequent design analyses for different structural designs, when the geometry of the acoustic domain remains unchanged. Thus, only one complete acoustic analysis is required for each acoustic geometry change, instead of a complete analysis for each structural design change. The number of radiation modes is truncated to decrease the storage requirements. The truncation error that is introduced by incorporating only the most efficient modes can be assessed easily.

The radiation modes formulation for subsystems, as presented here, was implemented in the acoustic code bArd [1998]. Using bArd as an engine to compute the radiation modes, the model reduction technique that was outlined, was implemented in the SATURN toolbox [Kessels et al., 1998; Kessels, 1999]. The application of the radiation modes formulation for the acoustic design of MRI scanners will be shown in chapters 5 and 6.

# 5 Towards the acoustic design of an MRI scanner

## 5.1 Introduction

To enable the use of acoustic models for the design of MRI scanners, it is important to know what kind of information needs to be provided by the models and how they should be used to obtain this information. Concretely, this means that an appropriate design objective function needs to be chosen to quantify the noise production of the MRI scanner, and some guidelines are necessary how to calculate numerical values for the design objective function with the acoustic models.

The first problem that needs to be addressed is the choice of an appropriate design objective function for acoustic design of the MRI scanner. The noise in the scanner is for a major part produced by gradient coil system vibrations. The noise can be quantified by for instance the sound pressure level in the MRI bore, or by the sound power level. The relationship between these quantities is unclear beforehand, so in principle it is possible to decrease the sound power level and at the same time increase the sound pressure level inside the MRI bore. On the other hand, it might also be possible that a strong positive correlation exists between the vibration level and the sound pressure and power levels. Then it would be possible and sufficient to use the vibration level of the gradient coil system as a design objective function, which makes a detailed acoustic analysis unnecessary. These issues are addressed in section 5.2.

When an appropriate design objective function has been defined, acoustic models of the MRI scanner are used to obtain numerical values for this function. This enables an acoustic comparison between different MRI designs. However, the acoustic information that is needed to obtain a value for the design objective function can often be obtained in many different ways, and in different levels of accuracy. Furthermore, most modeling techniques are somewhat restricted in the application range, so it might not be possible to cover the complete design space with a certain modeling technique. Conversely, some techniques might provide more information than is strictly needed to compute the design objective function. This might provide the designer with additional useful information. These issues necessitate a discussion about the characteristics, advantages, and disadvantages of the various modeling techniques that are presented in this thesis, for the design process of the MRI scanner. This discussion is covered in section 5.3.

## 5.2    Choice of an appropriate design objective function

Inside the MRI scanner, a patient experiences direct sound radiation from the gradient coil system (casing). The scanner's operator and the medical staff near the scanner also experience noise directly from the gradient coil system, but also from other parts of the scanner, which are excited indirectly by gradient coil system vibrations. However, measurements on an MRI scanner system have revealed that the major contribution to the sound production is caused by the direct radiation of the gradient coil system [Kooyman et al., 1993]. Therefore, given the current MRI scanner concept, the main objective of a low-noise design for the MRI scanner should be the decrease of the noise produced directly by the gradient coil system vibration. This objective is quantified in the design objective function, whose mathematical expression is a function of the design variables often indirectly expressed through the structural-acoustic response of the system.

### 5.2.1    Literature

The literature on the choice of design objective functions for acoustic design of radiating structures is limited. Often a choice is made for radiated sound power or sound pressure level at a certain position in space without providing much argumentation. An exception to this rule is the research of Lamancusa [1993]. In his paper, Lamancusa evaluated several choices for a design objective function for the numerical optimization of the structural-acoustic low-noise design of rectangular panels. He found that the choice of an appropriate objective function is critical to the success of the low-noise design optimization. For panels he concluded that power is a direct measure of acoustic performance and when used as a design objective function, produces the most consistently improved designs.

A disadvantage of power (or pressure) as the design objective function is that its calculation requires a complete acoustic analysis. Because structural vibrations are the origin of the noise production, the mean square velocity is sometimes used as an alternative design objective function. This is permissible when a good correlation exists between the radiated power and the vibration level. Using the vibration level has the advantage that only a structural calculation is required, which significantly decreases the total analysis time. For rectangular panels, Lamancusa [1993] found that using the vibration level as a design objective function produced similar results as using the sound power level as a design objective function. This indicates that for the rectangular panels that Lamancusa investigated, a strong correlation between vibration level and sound power level can be established.

An alternative method to decrease the computational effort and yet to incorporate the acoustic characteristics of the problem is to look at the radiation efficiency of the structural modes. Although this can unveil important radiation characteristics of a structure, it is not a good idea to use this in an optimization, because (at least for panels) Lamancusa found that decreasing the radiation efficiency of individual modes does not guarantee decrease of the radiated power due to modal coupling effects and due to potential increase in mean square velocity. These results were confirmed by a study of Termeer [1997].

Although the findings of Lamancusa can aid in the choice of an appropriate design objective function, his conclusions should be followed only with cautiousness as they were obtained by studying the radiation of square panels only. The acoustic behavior of an MRI scanner is quite different from the behavior of a vibrating panel. Therefore, a design objective function should be chosen here that properly incorporates the radiation characteristics of the MRI scanner. This will be discussed next.

### 5.2.2  Assessing the acoustic performance

For the MRI scanner three obvious acoustic design objective functions were considered:

- minimizing the vibration level (mean square velocity),
- minimizing the sound power level,
- minimizing the (spatially-averaged) sound pressure level.

The advantages and disadvantages of the application of these objective functions are discussed in the following paragraphs.

*Vibration level.*   Using the vibration level as objective function is computationally advantageous because it does not require an acoustic analysis. However, possible changes of the radiation efficiency characteristics are neglected then. As a consequence, lowering the vibration response does not automatically guarantee lowering the noise. Recall the expression for the sound power,

$$\bar{P} = \sigma \rho_0 c_0 S \langle \bar{v^2} \rangle.$$

If the vibration level decreases, but the radiation efficiency $\sigma$ increases, then the resulting noise level $\bar{P}$ will not decrease proportionally and could even increase. Moreover, it is not uncommon that an increase of vibration level accompanies a decrease in noise level [Baumann et al., 1992]. Thus the vibration level as a design objective function is only feasible when the radiation efficiency is nearly constant in the frequency range of interest *and* does not change significantly in the optimization process. Only then, a change in vibration level is directly related to the change in noise level, which means that the vibration level can be used as an objective function.

*Sound power level.*   Choosing the radiated sound power level as design objective function is a direct measure for the noise that is produced by a radiating structure. However, the power calculation requires a complete acoustic analysis after the structural calculations. Besides being a global acoustic measure, the radiated acoustic power is also closely related to the acoustic pressure that can be sensed in the far field. However, evanescent (non-radiating) pressure waves may be present near the surface of a radiating structure which may also determine the acoustic pressure load that is experienced there. Thus the radiated power is a good measure for the far field pressure and *can* be a good measure for the field near the structure if the evanescent pressure field is negligible with respect to the total radiated pressure field. Unfortunately, it is often impossible to prove whether or not such an assumption is justified. Its validity can only be established by studying the correlation between pressure and power results of many different structural designs and load cases.

Important for efficient structural-acoustic design is the case when the radiating shape of a structure (the boundary of the acoustic domain) does not change (often) during the design process. Then the acoustic power can be calculated rather fast with the radiation modes formulation (see section 4.3). When the acoustic power would be chosen as the objective function, then a complete acoustic analysis would have to be performed only once per geometry, and the results of the radiation modes analysis can be reused in subsequent acoustic analyses. This will greatly reduce the calculation time disadvantage due to taking the acoustic power as design objective function.

*Sound pressure level.*   Selecting the sound pressure level as design objective function seems to be very attractive because it most directly relates the calculated response to the

noise that is experienced. But, it is advisable to evaluate the acoustic pressure not on a single position, but on a number of points because the spatial dependence of the acoustic pressure is often quite large, and also very sensitive to small perturbations. Unfortunately, a reduction technique like radiation modes for the radiated acoustic power, is not (yet) available for the acoustic pressure, which means that a complete acoustic analysis is required for each design. So taking the pressure level as design objective function is only advisable when one is interested in the sound pressure at certain positions in the acoustic domain where the correlation between sound power and sound pressure is poor. This can happen for instance near the surface of a vibrating structure for which the evanescent pressure fields cannot be neglected, or in a strongly directional sound field.

### 5.2.3  A design objective function for MRI scanner noise

Applying the previous reasoning to an MRI scanner, it is certainly not advisable to use the vibration level beforehand as an objective function, because the behavior of the radiation efficiency as a function of frequency has not yet been established. In sections 5.3 and 6.2 it will be shown that the radiation efficiency of the MRI scanner is in fact a function that strongly depends on the frequency. Furthermore, it is not clear beforehand whether future design alterations will affect the radiation efficiency significantly. For these two reasons, a strong correlation between vibration level and acoustic performance of an MRI scanner is not to be expected.

The choice between selecting the sound power level or the sound pressure level as objective functions, is less easy to make. It will be shown in sections 5.3 that, for a (baffled) MRI system subject to a representative vibration distribution, the spectra of the radiated power and sound pressure inside the MRI bore are closely related. In other words, the evanescent pressure fields are negligible. However, similar spectra for one MRI scanner model do not guarantee similar spectra for an altered model. Therefore, for the design it is also important to know if alterations in the MRI scanner model will result in acoustic spectra changes that are similar for both sound power and pressure. Only if the strong correlation is preserved, then sound power and pressure are interchangeable as design objective functions. This issue is considered in the design studies presented in section 6.4.

If there is a close relation between sound power and sound pressure, then choice for sound power as design objective function is obvious for three reasons: it is a measure for both the field in the MRI bore and for the far field, it can be obtained relatively easy, and it is possible to reduce the calculation time of the acoustic analyses by using the radiation modes reduction technique.

### 5.2.4  Handling of broadband excitation

Lamancusa [1993] studied the acoustic optimization of rectangular panels and found that optimization improvements for single frequency excitations could be extended over a wider frequency range. This was caused by the fact that the improvements tended to decrease the (overall) vibration level, rather than decreasing the radiation efficiency at this single frequency. Therefore, he concluded that single frequency optimization is effective and produces very good broadband results. But, as for the choice between pressure and power as objective function, such a conclusion can only be made afterwards. For acoustic problems with different structures, these conclusions could easily be opposite. It is possible that optimization improvements will not alter the vibration level, but instead decrease

the radiation efficiency at one frequency. But, in a wider frequency band, the radiation efficiency might be increased and hence the optimized design would produce more noise in a wider frequency band. To prevent such problems, it is necessary to use broadband optimization techniques when dealing with broadband excitation.

The broadband excitation of the MRI scanner is handled in this thesis by performing acoustic analyses on a number of distinct frequencies. The frequency spacing has to be chosen such that no significant new response characteristics are introduced by further increasing the number of frequencies. Preliminary studies for this thesis have revealed that for the MRI scanner, about 50 frequencies are needed in the frequency range of interest ($100 - 2000$ Hz). The spacing between the frequencies was chosen logarithmically. With this spacing, the acoustic response was calculated at typically four frequencies per third octave band.

Small differences in the acoustic responses of different models do not have a serious impact on the amount of noise that is experienced. For instance, a small frequency shift of a resonance peak will be visible in the narrow-band spectrum, but the overall noise sensation will be similar. Therefore, some of the results presented in this thesis will also be shown as A-weighted responses which facilitates a more fair comparison of results.

To compute the third octave levels, the narrow-band spectra were *integrated* over third octave bands (indicated in the figures with the addition (3rd) in the ordinate labels). For the integration, it is assumed that the narrow-band spectra can be interpolated within each frequency band. Since the radiation efficiency is defined as a ratio of energies, A-weighing and integrating over a frequency band does not make much sense. Therefore, the third octave band levels for the radiation efficiencies were *averaged* over the frequency bands (indicated in the figures with the addition (3rd,avg) in the ordinate labels).

## 5.3    Application of the different acoustic formulations in the design process

In chapters 2 and 3, two acoustic modeling techniques for the MRI scanner were presented: a semi-analytical baffled finite duct formulation for cylindrical ducts with constant cross-section and a Fourier BEM technique which can handle a large variety of axisymmetric MRI geometries. Furthermore, in chapter 4, a technique was developed to obtain a modal decomposition of the vibration field to obtain independently radiating vibration patterns. These techniques all have their merits for the design process of the MRI scanner, but they also have disadvantages and restrictions. These will be discussed here.

### 5.3.1    Comparison between the baffled duct and Fourier BEM formulations

The main feature of the baffled finite duct formulation is that it directly provides insight into the physics of acoustic radiation of the scanner, as will be shown here. From its mathematical formulation it follows that the field inside the duct is a convolution of the field of a simple source in the duct and the vibration distribution of the gradient coil system (see equation (2.24)). The part of this acoustic field that is generated outside the scanner bore is determined by the transmission coefficients which depend on the frequency and the duct diameter (see equation (2.48)). Also, as in infinite ducts, the cut-on and cut-off phenomena are present, which are related to the fact that duct modes can only propagate acoustic energy above their so-called cut-on frequencies. The most

important phenomenon in finite ducts that is revealed by this baffled duct formulation, is that of so-called near cut-on resonances. This will be discussed in section 6.2, where it is shown that these radiation characteristics can be investigated easily and efficiently with the baffled duct formulation.

The benefits of Fourier BEM lie in the almost infinite variation in axisymmetric geometries that can be modeled with this formulation. This is in contrast with the baffled duct formulation, where only cylindrical ducts with constant cross-section can be modeled. Unfortunately the formulation of a Fourier BEM model for the MRI scanner provides no direct insight into its acoustical characteristics. But it is possible to convey the insights that were gained with the baffled duct model to a similar Fourier BEM model. When the Fourier BEM model is subsequently altered, it is still possible to relate the response changes caused by the design changes to the physics of the radiation phenomena that were observed with the baffled duct model. An example of the strength of using this methodology in the design process is presented in section 6.3.2.

An opposite approach can also be followed: by comparing results from different baffled duct models with a Fourier BEM model of the MRI scanner that is almost equivalent, also more physical insight into certain acoustic phenomena can be obtained. In this way, the altered response characteristics due to changes in the baffled duct model can be investigated when the Fourier BEM model serves as a reference. This will be shown next.

*Numerical experiments on the truncation of the Fourier-Bessel series.*

When the baffled duct formulation is used for an acoustic model of the scanner, the pressure field inside the MRI scanner bore is determined by the amplitudes of the Fourier-Bessel modes which describe the acoustic field (see equation (2.8)). For the MRI scanner, which is modeled as a duct with vibrating walls, these amplitudes are a function of the axial coordinate $z$ (see equation (2.38)). The number of Fourier-Bessel modes $N$ that is used in a numerical analysis with the baffled duct model (section 2.3) determines the accuracy of both the pressure field and the radiated power, but also determines the size of the system matrices and hence the computational effort.

From general duct acoustics theory, it is known that radiated acoustic power is transported only by cut-on modes (modes for which the axial acoustic wavenumber $k_{m\mu}$ is real; see section 2.2.2). Below a certain frequency there is only a limited number of cut-on modes. Therefore, for an accurate computation of the radiated power in a baffled duct model one only needs to incorporate the cut-on modes, so the number $N$ may be relatively small. On the other hand, Hewlett et al. [1995] found that some of the cut-off modes need to be included in a baffled duct model analysis to properly predict the pressure field. However, no recommendation was given on the number of extra modes. Therefore, it is unclear how many modes need to be used for an accurate prediction of the pressure field. This will be investigated here with a numerical experiment.

To assess the influence on the predicted acoustic response of truncation of the Fourier-Bessel series, the number of Fourier-Bessel modes for a baffled duct model was varied from $N = 5$, $N = 10$, $N = 25$ to $N = 40$. These results were compared with the results from a Fourier BEM model. The geometry, boundary conditions and numerical integration accuracy of the baffled duct and Fourier BEM models were similar, except for the outer radius which is infinite for the baffled duct model and $r = 1$ m for the Fourier BEM model. Both models are depicted in figure 5.1.

**(a)** Baffled duct model.                    **(b)** Fourier BEM model.
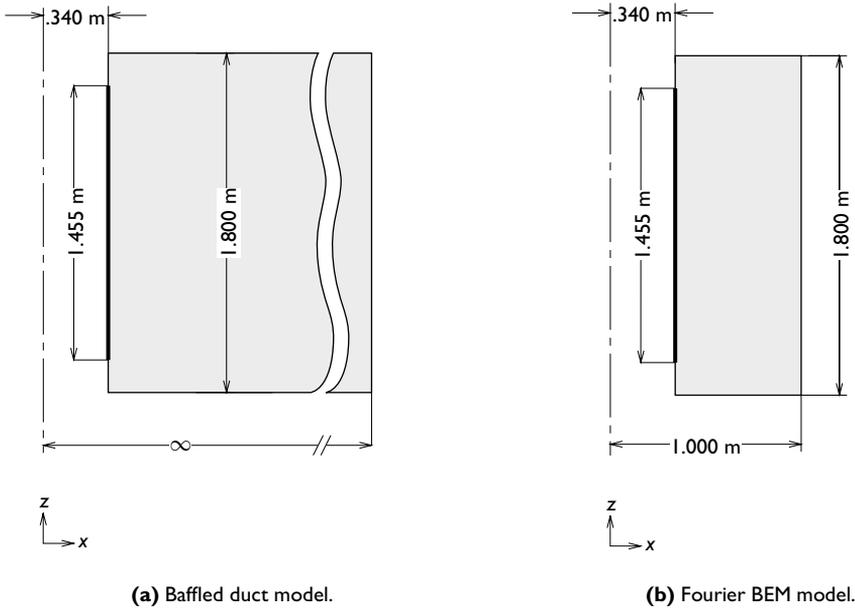
**figure 5.1** Axisymmetric duct models. The vibration field was described for the part of the duct where the gradient coil system is located for an MRI scanner, indicated by the thick lines.

For the excitation of the models, a vibration distribution must be specified inside the duct. In the case of the real MRI scanner, the acoustic domain in the scanner is excited by gradient coil system vibrations. For the acoustic analyses, a representative vibration excitation was computed with a simplified structural model of the scanner. Details about the computation of this excitation can be found in appendix C.

The amplitude of the Lorentz force excitation as a function of the frequency depends very much on the MRI scanning sequence that is used. Because it is impractical to analyze the structural response for every possible scanning sequence, it was chosen to apply a uniform force spectrum for the calculations. In this way, the response characteristics for a large class of scanning sequences can be studied. For a realistic scanning sequence, the non-uniform force spectrum should be accounted for, for instance by weighing the acoustic response spectra by the relative contribution of the forces as a function of frequency.

Since the scanner's excitation is broadbanded, the response at 53 frequencies in the frequency range $100 - 2000$ Hz was calculated (see also section 5.2.4). To facilitate the comparison of results throughout this thesis, the representative excitation that was used here, will be applied in all subsequent analyses, except where explicitly stated otherwise.

The vibration level of the representative excitation as a function of frequency is shown in figure 5.2. The results are presented here as the narrow-band spectrum and an A-weighted spectrum where the spatially-averaged mean square velocity has been *integrated* over each third octave band.

It should be noted that the representative vibration distribution only contains the $m = 1$ circumferential harmonic and displays distinct resonance peaks. Measurements by Kooy-
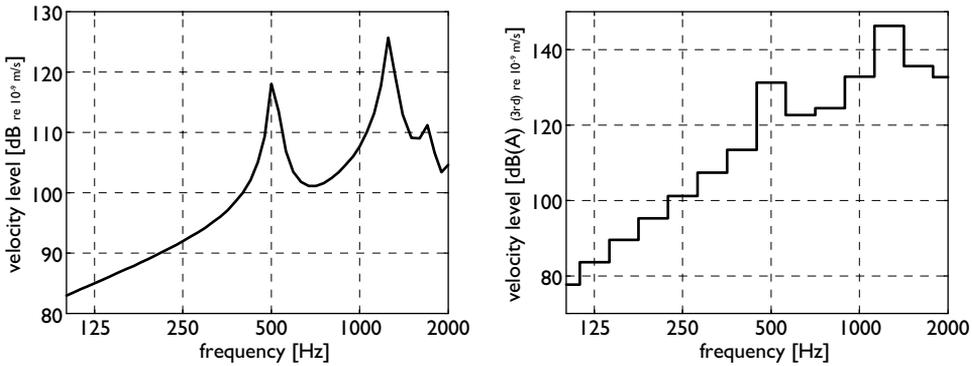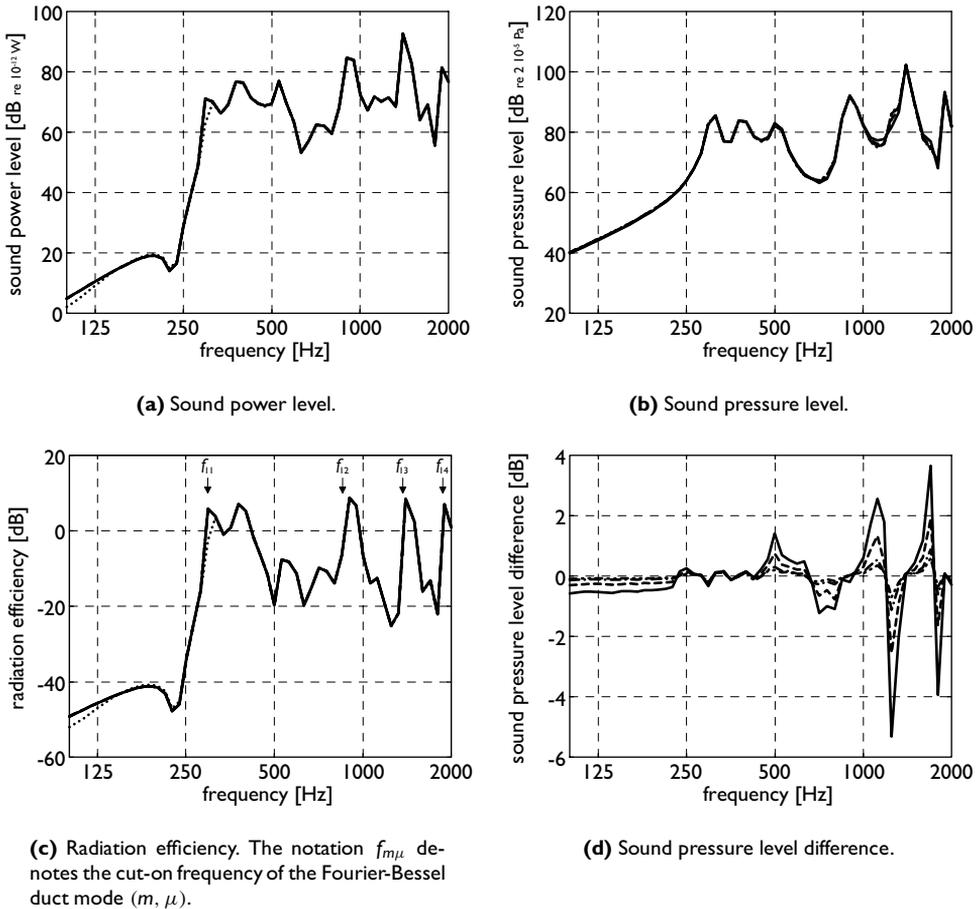
**figure 5.2** Representative excitation velocity level, presented as a narrow-band spectrum (left) and as an A-weighted spectrum which is *integrated* over third octave bands (right).

man et al. [1993] showed that the resonances in the vibration level of a real gradient coil system are less distinct which suggests an underestimation of the damping in the computed vibration distribution. Moreover, recent measurements by Kessels [1999] revealed that a real MRI scanner's vibration distribution also contains multiple circumferential harmonics. This is probably caused by a non-axisymmetric distribution of the material properties and construction imperfections, which causes excitation of multiple circumferential harmonics in the vibration response by each of the circumferential harmonic components in the distributed force. This harmonic coupling was not incorporated in the structural model. A discussion about the influence of these aspects can be found in Kessels [1999].

The above mentioned discrepancies between computed and measured vibrations, are a warning that not all of the results and conclusions can be promptly translated for practical use. When interpreting the computational results, the restrictions of the applied vibration field have to be kept in mind. Strictly speaking, the results computed here are only valid for real gradient coil systems with the same materials as used in the computations and subject to the same excitation force. But fortunately, the results computed here also reveal the important acoustic characteristics for a whole class of similar gradient coil systems in general, as will become clear from the studies presented next. Therefore, most conclusions and recommendations remain usable when the vibration distribution contains multiple harmonics and when the resonance peaks are less pronounced. Where appropriate, remarks will be made as to what extent the results and conclusions will change when the vibration excitation is altered.

*Results and discussion*

Now, the results of the numerical experiment will be presented and discussed. For the baffled duct models and the Fourier BEM model, the following response quantities were computed: the sound power level, radiation efficiency, and sound pressure level (mean square value, spatially averaged over the wall surface). All acoustic calculations here, as well as later in this thesis were performed with the program bArd [1998]. The frequency range and spacing for the acoustic analyses were chosen identical to those of the structural analysis: 53 frequencies, logarithmically spaced in the range $100 - 2000$ Hz, resulting in 4 frequencies per third octave band, on the average.

**(a)** Sound power level.



**(b)** Sound pressure level.



**(c)** Radiation efficiency. The notation $f_{m\mu}$ denotes the cut-on frequency of the Fourier-Bessel duct mode $(m, \mu)$.



**(d)** Sound pressure level difference.

**figure 5.3** Acoustic responses for Fourier BEM model and baffled finite duct with different number of Fourier-Bessel duct modes $N$. ——— : $N = 5$; ----: $N = 10$; —·—·— : $N = 25$; —··—··: $N = 40$; ·········: Fourier BEM model.

The sound pressure level at the wall is used as a measure of the pressure field inside the duct and includes the contribution of the evanescent pressure waves. The radiated power is taken as a measure for the far field response. The radiation efficiency is a measure for the effectiveness of the transformation of vibration energy into acoustic energy radiated from the duct. The spectra of these results can be found in figure 5.3. The sound pressure level difference in this figure is defined as the difference between the sound pressure level of the baffled duct model and the sound pressure level of the Fourier BEM model.

The radiated power spectra for the baffled duct models in figure 5.3(a) show that the power radiation is relatively insensitive to the number of Fourier-Bessel modes $N$. This indicates that a good approximation for the power can be made with only five Fourier-Bessel modes. This confirms the reasoning that radiated power is associated with cut-on (i.e. propagating) modes of the acoustic field. A mode is cut-on here if the excitation frequency is above the Fourier-Bessel mode's cut-on frequency $f_{m\mu}$ (see appendix A) so

its corresponding axial wavenumber $k_{m\mu}$ is real. If all cut-on modes are taken into account, the approximation of the radiated power will be good. In these simulations at most four cut-on modes can be present below 2000 Hz in the acoustic field (see table A.2(a) in appendix A). As a consequence, when taking more than $N = 3$ modes into account, the computed values for the radiated power are accurate. Differences between the power spectra for the Fourier BEM model and the baffled duct models are only visible for low frequencies. These differences are caused by the finiteness of the outer radius of the Fourier BEM model and decrease when the outer radius of the Fourier BEM model is increased [Kuijpers et al., 1998a].

The results for the sound pressure level at the duct wall are approximated sufficiently accurate at frequencies where the pressure is relatively high in figure 5.3(b). At these frequencies, the results obtained with the baffled duct model compare very well with the Fourier BEM model results. However, there are considerable pressure level differences at frequencies where the pressure is relatively low, especially when only a few Fourier-Bessel modes are taken into account (see figures 5.3(b) and 5.3(d)). For this model, this indicates that high sound pressure and radiated power values are associated with wall vibration energy being transferred to cut-on duct modes, whereas low sound pressure and power values are associated with vibration energy being transferred to cut-off duct modes. Thus, a logical consequence of not including these cut-off modes is a less accurate prediction of the pressure level at frequencies where the pressure level is relatively low.

If a decreased accuracy at low pressure values is not acceptable then at least $N = 25$ modes should be included to obtain results that are within a 0.5 dB range of the Fourier BEM results. If the constraints on the pressure results are less strict, then fewer modes are sufficient. For instance when the pressure should be accurate (i.e. within 1 dB of the Fourier BEM results) at frequencies where the pressure is relatively high, then even the model with only $N = 5$ Fourier Bessel modes suffices. It is anticipated that the pressure level differences can be further minimized when the number of Fourier-Bessel modes is further increased. However, the number of modes cannot be increased beyond a certain limit because of numerical overflow and underflow errors.[1]

A remarkable acoustical phenomenon that is observed, are the peaks in the radiation efficiency curves for both models. At a number of frequencies the radiation efficiency is very high, with values that reach out 20 dB above surrounding values. The peaks are located just above the cut-on frequencies $f_{1\mu} = 296, 855, 1368$, and 1877 Hz (see table A.2(a)). These are the cut-on frequencies for different numbers of nodal circles $\mu = 1, 2, 3$, and 4, respectively, of the Fourier-Bessel duct modes with Fourier harmonic number $m = 1$. These distinct peaks are also observed in the power and pressure spectra. Since these peaks are predicted by both formulations they are likely to indicate a genuine acoustic characteristic of a finite duct, rather than an artifact of the mathematical formulation of the methods. The origin of these peaks will be discussed in the next chapter in section 6.2.

Looking at the results for both models, there is no clear preference for one of both methods. But, an attractive additional property of analyses with the baffled duct models is their numerical efficiency compared with Fourier BEM models [Kuijpers et al., 1998a]. This is especially noticeable for the baffled duct models with only a low number of Fourier-Bessel modes $N$, when a speed increase factor of 15 was achieved. But, the side effect of

---

1.   Overflow and underflow errors occur in vectors $\boldsymbol{h}^{\textcircled{1}}$ and $\boldsymbol{h}^{\textcircled{2}}$ (see equations (2.53) and (2.58)) for large $N$ and consequently large values of the product $k_{m\mu} z$.

the less accurate low pressure values should then be allowed for. Fortunately, for low-noise design, the high pressure values determine the noise load, so inaccuracy of the low pressure values is of lesser importance. Hence, the baffled duct formulation can be used as a quick and accurate investigative tool for preliminary design studies with simplified MRI scanner models.

Another issue that has to be considered for modeling the MRI scanner is the fact that with the baffled duct model only ducts with a constant cross-section can be modeled. This restriction may prevent the baffled duct formulation to be used for the complete design space for the scanner, but its formulation then still offers some physical insights that can be extended to more complex geometries, as will be shown in section 6.3.2.

*Conclusions*

The application of the baffled duct and Fourier BEM formulation for design studies of MRI scanners was considered in this section. It was observed that a good prediction of the radiated power can be obtained with the baffled duct model with only a few Fourier-Bessel duct modes in the formulation. The acoustic responses show a good correlation between the sound power level and sound pressure level inside the MRI bore. This strong correlation manifests itself in the peaks in the power and pressure spectra just above the cut-on frequencies of the Fourier-Bessel duct modes. These typical aspects of the finite duct radiation will be discussed more extensively in the next chapter.

The use of the baffled duct model for all stages in the design of the MRI scanner is infeasible because the model geometry with this formulation is restricted to ducts with constant cross-section. But it can still be used as a quick investigative tool. For models with geometrical configurations other than constant cross-section, the Fourier BEM model is a usable alternative. The insights gained with the baffled duct model can be conveyed to the Fourier BEM model to cover a larger design space. The radiation modes formulation can aid in this process, as will be shown next.

## 5.3.2  Application of the radiation modes formulation

In this section it will be shown that the radiation modes formulation offers a unique perspective into the radiation characteristics of finite ducts with vibrating walls. It will also be shown that these characteristics make the use of the radiation modes reduction technique feasible for these finite ducts, for low to medium frequencies.

The velocity distribution of a vibrating structure can be decomposed in an orthogonal modal basis for each frequency. These modes are called radiation modes because they independently contribute to the radiated acoustic power. Each radiation mode has an associated modal radiation efficiency. This enables a decomposition of the vibration field in a set of efficiently and a set of less efficiently radiating components. As was explained in chapter 4, each velocity distribution can be expressed as a weighted sum of radiation modes. The weighting factors are called modal contribution coefficients. The radiated acoustic power is the simple sum of the products of the squared modal contribution coefficients divided by two and multiplied by their corresponding modal radiation efficiencies. This enables the use of the radiation modes formulation as a model reduction technique to speed up subsequent sound power calculations with the same acoustic geometry.
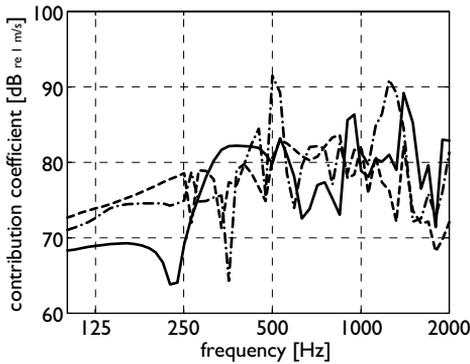
*Modal contribution coefficients*

The modal contribution coefficient is a measure for the contribution of a radiation mode to the vibration field. The squared modal contribution coefficient multiplied by its corresponding modal radiation efficiency is a measure for the (orthogonal) contribution of a certain radiation mode to the total radiated power. With these measures, the components of the vibration which contribute the most to the noise, can be identified. Suppressing the vibration level (i.e. the contribution coefficient) of the radiation modes that contribute the most to the radiated power results in a decrease of the noise level that is produced. For tonal or narrow-band excitation this can be practically realizable by passive or active vibration control [Baumann et al., 1992; Elliott and Johnson, 1993; Naghshineh and Koopmann, 1993; Borgiotti and Jones, 1994; Naghshineh et al., 1998]. For broadband excitations, this is much more difficult to accomplish because of the frequency dependence of the radiation mode shapes. This necessitates a suppression of a different efficient vibration distribution at each frequency, which is hard to accomplish for all efficient vibration distributions simultaneously. But a contribution analysis with radiation modes still offers insight into the radiation characteristics of structures with broadband excitation, as will be shown next.

There is a large amount of information that can be obtained from a radiation modes analysis of a structure with broadband excitation. To illustrate this statement, a radiation modes analysis was performed with a Fourier BEM model of a simplified MRI scanner (see figure 5.1(b)) with a representative broadband excitation (see section 5.3.1). The results of this analysis can be found in figure 5.4. In figure 5.4(a) the modal contribution coefficients of three radiation modes that *contribute* the most to the sound power are depicted for each frequency. These modes were ordered by magnitude of their radiation efficiency. This efficiency is shown in figure 5.4(b). The contribution to the radiated power for each of the selected radiation mode is shown in figure 5.4(c), together with the total power radiation. Finally, the actual radiation efficiency of this vibration can be compared with the radiation efficiency of the radiation mode that contributes the most in figure 5.4(d).

Some remarks have to be made before interpreting these results. The radiation modes that were chosen in this example are the modes that contribute the most to the radiated power. These modes are not necessarily the radiation modes with the largest efficiencies, but they have the largest product of squared modal contribution coefficient and the modal radiation efficiency. It may very well be possible that there are some radiation modes which are more efficient than these three, but they were not excited by the vibration field. In other words, their modal contribution coefficient is very small (or zero). For the analysis presented here, the excitation field is symmetric with respect to the duct's isocenter cross-section because the excitation force is also symmetric (see appendix C). Therefore, the modal contribution coefficients of the antisymmetric radiation modes will be zero although they might have a large radiation efficiency. To be more precise, in the results presented here, the three modes correspond to the three most efficient *symmetric* radiation modes.

The three radiation modes participate equally in the vibration field (see figure 5.4(a)) Their contribution coefficients are of the same order of magnitude. But, the radiation efficiencies of the second and third radiation mode are considerably lower than that of the first mode, especially in the lower frequency range (see figure 5.4(b)). Therefore, the contribution to the radiated power of the second and third mode is only significant at higher frequencies
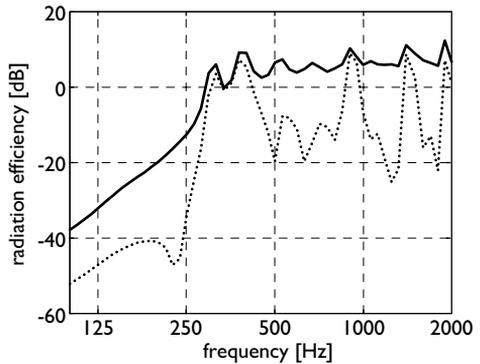
**(a)** Modal contribution coefficients per radiation mode.
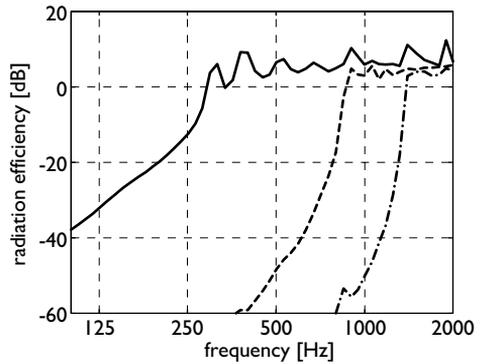
**(b)** Radiation efficiency per radiation mode.
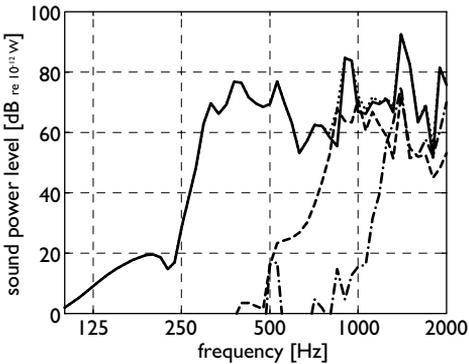
**(c)** Power contribution per radiation modes and total radiated power.

**(d)** Radiation efficiency of most efficient radiation mode and total radiation efficiency.

**figure 5.4** Radiation modes information for the MRI scanner model. ——— : first radiation mode; ---- : second radiation mode; –·–··– : third radiation mode; ········: total.

(see figure 5.4(c)). Until about the second cut-on frequency of the $m = 1$ duct mode (855 Hz), only the first radiation mode contributes to the radiated power, even though its contribution coefficient is the lowest for the major part of this frequency range. After that, until the third cut-on frequency of the $m = 1$ duct mode (1368 Hz), only the first and second modes contribute to the power. In the frequency range from 1368 Hz to 2000 Hz all three radiation modes contribute to the power. But, although the contribution of mode two and three is significant, the first mode (the most efficient symmetric radiation mode) still dominates the power radiation, because, for almost the whole frequency range, its power spectrum is indistinguishable from the total power spectrum. In figure 5.4(c), only at about 800 and 1800 Hz slight differences can be observed.

It is also interesting to see that the actual radiation efficiency of the vibration distribution is near its maximum value just above the cut-on frequencies of the duct (see figure 5.4(d)). This means that the actual vibration at those frequencies matches very good with the shape of the most efficient symmetric radiation mode. This can also be seen
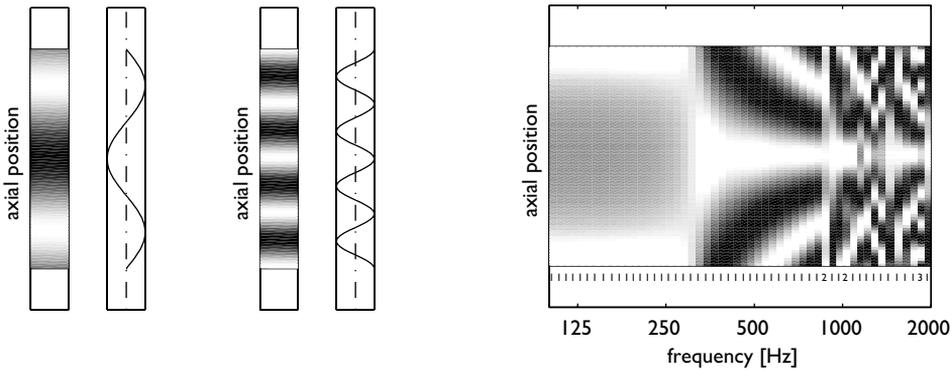
**(a)** Example of the grey scale representation of the vibration distribution along the axial coordinate.

**(b)** Radiation mode shapes of the mode that contributes modes to the radiated power. The numbers below the vibration distributions denote the order number of the predominant radiation mode (e.g. 2 means that at that frequency, the second radiation mode contributes the most to the radiated power and is plotted here).

**figure 5.5** Vibration distribution of the radiation modes in axial direction

from figure 5.4(a), where the contribution coefficient of the most efficient radiation mode is maximal just above the cut-on frequencies. This again points to the importance of duct acoustic phenomena for the (simplified) MRI scanner. Later in this thesis, the relevance of these insights for structural-acoustic optimization will be considered (see section 6.4).

*Radiation mode shapes*

It is important to remember that the axial shapes of the radiation modes change with increasing frequency. This can be illustrated by plotting the vibration distribution along the vibrating part of the finite duct model for Fourier harmonic $m = 1$ (so a cosine variation of the vibrations is assumed in the circumferential direction). The vibration distribution of the radiation mode that contributes the most to the radiated power is shown as a function of the frequency in figure 5.5.

The shape of the most contributing radiation mode is a gradually changing function of the frequency. The axial wavenumber content of the modes (indicated here by the number of black/white transitions) increases gradually with increasing frequency. But at the cut-on frequencies the shape changes dramatically. At those frequencies, the radiation mode shape has a much lower axial wavenumber. After this sudden change the axial wavenumber is again increasing gradually.

In fact, the vibration distribution near the cut-on frequency matches the axial variation of the Fourier-Bessel duct mode that has just become cut-on at that particular frequency. Near cut-on, the Fourier-Bessel duct mode also has low axial wavenumber $k_{m\mu}$, similar to the radiation mode, as can be seen in figure 5.5(b). This indicates that the cut-on phenomenon of the Fourier-Bessel duct mode plays an important role in the origination of the peaks in the pressure, power and radiation efficiency levels.

*Design insights*

From results of the radiation modes analysis, some important acoustic insights can be distilled for this MRI model and corresponding excitation.

- For a certain frequency, a radiation mode that is present in the velocity field does only contribute to the radiated acoustic power if its radiation efficiency is of the same order of magnitude as the maximum efficiency of other present components.

- For duct-like structures, the efficiency of say the $n$th efficient radiation mode becomes significant above the $n$th cut-on frequency of the duct mode with the same Fourier harmonic number $m$. In other words, the $n$th efficient radiation mode contributes only to the radiated power above the cut-on frequency $f_{mn}$.

- The contribution of the first radiation mode dominates the sound power spectrum.

- Just above the cut-on frequencies, there are peaks in the sound power, sound pressure and radiation efficiency levels. The radiation mode shapes just above the cut-on frequencies have a low axial wavenumber, similar to the corresponding Fourier-Bessel duct mode that has become cut-on, which implies a close relationship.

For the designer these insights can be valuable. The results indicate that design efforts should be focussed on the most efficient radiation mode that is excited, because this mode dominates the acoustic response. However, the changing shape of the most efficient mode illustrates that it will be difficult to suppress all efficient radiation mode shapes simultaneously for all frequencies to decrease the noise. But, the major part of the acoustic energy is radiated at the cut-on frequencies. For this simple MRI model it might be possible to suppress the efficient radiation modes only around these frequencies to decrease the total sound power.

By comparing the actual radiation efficiency with the efficiency of the most efficient radiation mode, the designer gets an impression at what frequencies the maximum gain for low-noise design can be achieved, namely at frequencies where the actual radiation efficiency is near its maximum achievable value. For the model investigated here, this happens just above the cut-on frequencies, where the actual vibration distribution resembles the most efficient radiation mode very well. Suppressing the vibration level of the most efficient radiation mode at those frequencies while maintaining (or decreasing) the total vibration level will result in a substantial decrease of the total sound power.

*Design rules*

For the *simplified* MRI scanner model studied here, some design rules can be formulated from the discussion above.

- Attention should be focussed at those parts of the spectrum which determine the total sound power. For the present model these are the parts of the spectrum just above the cut-on frequencies. The efficient radiation modes around these frequencies should be suppressed to decrease the total sound power.

- At frequencies where the actual radiation efficiency is near the maximum achievable radiation efficiency, decreasing the vibration level of both the most efficient radiation mode and in total will result in a substantial decrease of the total sound power.

Because the calculation of both the actual and maximum achievable radiation efficiency is not restricted to axisymmetric (MRI) models, these design rules can also be valuable for the acoustic design of other vibrating structures.

(a) Velocity level.

(b) Sound power level.

(c) Sound pressure level.

(d) Radiation efficiency. ——— : maximum.
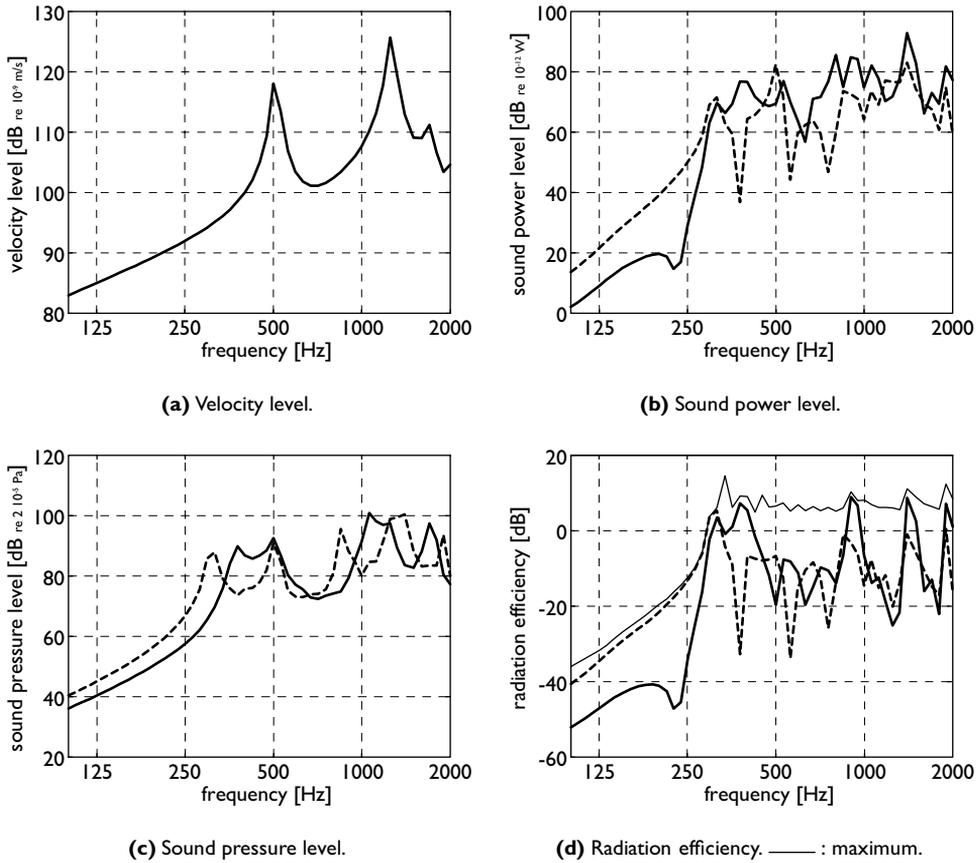
**figure 5.6** Response spectra for a simplified MRI scanner model. ———: realistic distribution; ----: uniform distribution.

Note that the vibration distribution used here only contains the $m = 1$ circumferential harmonic. When multiple harmonics are excited, then more cut-on frequencies are present and much more radiation modes will contribute significantly to the radiated power. This makes the practical implementation of this design rule more complicated.

To illustrate the use of these design rules for the simplified MRI scanner model, an additional analysis was made of the Fourier BEM model with identical vibration level, but now with a vibration distribution that is uniform along the axial coordinate direction (in contrast with the realistic excitation which is non-uniformly distributed). This should cause lower values of the contribution coefficient of the most efficient radiation mode because this vibration distribution matches less good to the most efficient radiation mode. The acoustic response spectra for velocity, sound pressure, sound power and radiation efficiency are shown in figure 5.6, and the corresponding levels are given in table 5.1. The sound pressure here is the mean square value of the sound pressure, spatially averaged over 40 positions inside the MRI bore. The maximum achievable radiation efficiency (i.e. the largest radiation efficiency of the radiation modes) is also shown in figure 5.6(d).

**table 5.1** Response levels for a simplified MRI scanner model with realistic and uniform vibration.

|  |  | realistic | uniform |
|---|---|---|---|
| $L_v$ | [dB(A) re $10^{-9}$ m/s] | 146.6 | 146.6 |
| $L_W$ | [dB(A) re $10^{-12}$ W] | 115.8 | 107.1 |
| $L_p$ | [dB(A) re $2 \cdot 10^{-5}$ Pa] | 136.9 | 131.7 |

Figure 5.6(a) shows that the velocity level is identical for both vibration distributions. But the pressure and especially the power levels for the uniform distribution are smaller than for the realistic vibration distribution. In figure 5.6(d), the cause for this difference is illustrated. The uniform distribution has a much lower radiation efficiency above 250 Hz. Near the cut-on frequencies, the radiation efficiencies are reduced with respect to their maximum achievable values as was suggested by the design rules. Below the first cut-on frequency, the efficiency has improved, but since the absolute value of the efficiency is low there, this has no adverse effect on the total power level. Thus, by maintaining the vibration level while changing the vibration distribution, the noise production of the simplified scanner model was significantly decreased. Note that changing the vibration distribution in a simulation is quite simple whereas it might be very difficult to accomplish this in practice. But with the simulations, it is possible to assess the effectiveness of such design efforts easily before trying to implement the design insights. This confirms the usefulness of these kinds of acoustic models for designers.

*Conclusions*

The radiation mode analysis indicated that per circumferential harmonic, only a few radiation modes are significant for the sound power radiation. As a general rule, the number of significant radiation modes is identical to the number of cut-on duct modes. This is the case, independently of the number of circumferential harmonics, although of course the total number of significant modes increases with an increasing number of harmonics. With the radiation modes analysis, the maximum achievable radiation efficiency of a vibrating surface can also be found. This can be helpful for the designer. At frequencies where the radiation efficiency is near its maximum achievable value, lowering the vibration level will generally result in a progressive decrease of the noise production. At those frequencies, a decrease in the vibration level cannot lead to an increase in the overall radiation efficiency and hence the vibration decrease is optimally utilized.

## 5.4   **Summary**

The acoustic design objective for the MRI scanner is the reduction of the noise that is experienced both inside the scanner by the patient, and in the close neighborhood of the scanner by the medical staff and the MRI operator. To quantify this goal an appropriate design objective function has to be chosen.

The radiated acoustic power is an ideal candidate for the design objective function. It is a global measure that incorporates the noise load on both patient and medical staff. Because there is a strong correlation between radiated power and acoustic pressure inside the MRI scanner bore, it should not be necessary to explicitly incorporate the acoustic pressure in the design objective function. In combination with the radiation modes formulation,

the radiated power can be computed directly from the vibration distribution. This only requires a single complete acoustic analysis, for each radiating geometry that is modeled.

The formulations that were developed for the acoustic design of the MRI scanner all have their own merits and restrictions. It was shown that the baffled duct formulation offers physical insight by its mathematical formulation. However, the geometries that can be modeled with this formulation are restricted to cylindrical ducts with constant cross-sections. The formulation is especially usable in for quick exploratory studies early in the design process. The Fourier BEM formulation does not have the constant cross-section restriction, but it does not offer direct insight into the acoustics of the problem via its formulation. Moreover, it is computationally more expensive than the baffled duct formulation. However, These disadvantages can, to a large extent, be overcome by combining the Fourier BEM formulation with a radiation modes analysis. Nevertheless, the acoustic insights gained from the baffled duct model can then still be valuable.

An example application of the combined Fourier BEM and radiation modes formulations for a simplified MRI scanner model was presented. The analysis revealed that there are typically only a few radiation modes that determine the sound power radiation of the MRI scanner model. Therefore, the use of the radiation modes reduction technique in parameter or optimization studies is feasible. Also, some important design insights resulted from the analysis. These insights lead to the formulation of two preliminary acoustic design rules: (i) Design efforts should be focussed at the radiation just above the cut-on frequencies, because the sound power radiated at those frequencies dominates the total sound power. (ii) When the actual radiation efficiency is near its maximum achievable value, then the noise can be reduced by changing the vibration distribution and/or changing the vibration level. The potential of these rules was illustrated with a numerical example study. The ability to quickly perform design studies and assess the influence of design changes, confirms the possible usefulness of these kinds of tools in a design environment.

# 6 Preliminary acoustic design studies for an MRI scanner

## 6.1 Introduction

Practical acoustic models for MRI scanners should be detailed enough to predict the important acoustic phenomena, and at the same time be simple enough to keep the computational effort manageable. An acoustic model for the MRI scanner is a simplified representation of a real scanner's acoustic behavior. For each simplification that is made, there is a tradeoff between the resulting predictive value of the acoustic model on the one hand, and its complexity and computational speed that determine the model's usability in the design process on the other hand. The acoustic designer's intuition, experience and prior knowledge are often used for evaluating these modeling simplifications. Where sufficient knowledge to make a fair evaluation is lacking, some preliminary design studies can aid the designer to gain an understanding of the important acoustic characteristics.

An important acoustic characteristic of finite baffled ducts in general, and for the MRI scanner in particular, is the occurrence of the so-called near cut-on resonances. These were first encountered in section 5.3, where a numerical study revealed that the scanner has a high radiation efficiency near some duct cut-on frequencies. This phenomenon needs further investigation to understand the underlying physics. By using a combination of the developed acoustic model formulations and by occasionally plunging into the model's mathematical formulation, the understanding of these acoustic characteristics of the MRI scanner can be improved. This research is covered in section 6.2.

Each of the simplifications that is made to develop a usable acoustic model for the MRI scanner introduces a modeling approximation error. The magnitude and severity of each approximation error is different for each of the simplifications and these properties need not be connected. An approximation error which is small in magnitude might change the design radically, so the approximation error is severe. The opposite is also possible: a difference in some acoustic property between model and reality might be very large, but when the effectiveness of design changes is not influenced by that, the approximation error is not severe. For the models studied in this chapter, approximations are made for the geometry, the vibration boundary conditions, and in the operating conditions of the scanner. For each of these approximations, the magnitude and severity of the approximation errors will be discussed.

The influence of the vibration distribution and level on the acoustic response will be briefly discussed in section 6.3.1. The geometry that is used for the acoustic model of the MRI scanner is another possible source of approximation errors. In practice the MRI scanner

is not a baffled finite duct: its flanges are not infinitely large, it does not have a constant cross-section, and it is not perfectly axisymmetric. This is discussed in section 6.3.2. Another possibly important aspect of the acoustic modeling of the MRI scanner is that of the operating conditions. During normal operation a patient is lying inside the MRI scanner bore which can change the acoustic response compared with the scanner without patient. The question whether or not this has to be taken into account in design studies, is addressed in section 6.3.4. Finally, in section 6.4, the potential of the developed tools is demonstrated in four parameter design studies for MRI scanners with different casing and subject to different excitations.

## 6.2   Near cut-on resonance phenomena in an MRI scanner

### 6.2.1   Maximum achievable radiation efficiency in plates and ducts

The radiation characteristics of plates [Elliott and Johnson, 1993; Cunefare and Currey, 1994] are considerably different from those of finite ducts with vibrating walls [Termeer, 1997]. This will be illustrated with some examples. Radiation modes analyses are discussed of both a vibrating baffled finite plate and a finite duct with vibrating walls, which is a simple representation of an MRI scanner without casing (see figure 6.1). The plate has the same length as the MRI gradient coil system ($2L = 1.455$ m) and a length/width ratio of $3/2$. The finite duct model is cylindrical with an inner radius of $a = 0.3405$ m, an outer radius of $A = 1.0$ m, a total length of $2L = 1.8$ m and a vibrating section of $2l = 1.455$ m. For the duct model, the radiation modes for the circumferential Fourier harmonics $0, 1, 2, \ldots 10$ were computed in the calculations. Details on the radiation modes computations for the plate can be found in Currey and Cunefare [1995].

With the radiation modes formulation it is possible to identify the maximum radiation efficiency which can be achieved at each frequency. The maximum achievable radiation efficiency is the largest efficiency of all radiation modes. When all vibration energy is put into that mode (which means that the modal contribution coefficients of all other radiation modes equal zero) then the actual radiation efficiency will be at its maximum.

The maximum achievable radiation efficiency for the finite plate (see figure 6.2(a)) increases quadratically ($+6$ dB/oct.) for low wavenumbers. For higher wavenumbers, the plate's maximum efficiency increases with the square root of the frequency ($+1.5$ dB/oct.). The slope change from quadratic increase to a square root increase in the graph for the maximum radiation efficiency of the plate occurs when approximately one acoustic wavelength fits into half of the plate's major dimension, or mathematically $f = c_0/l$.
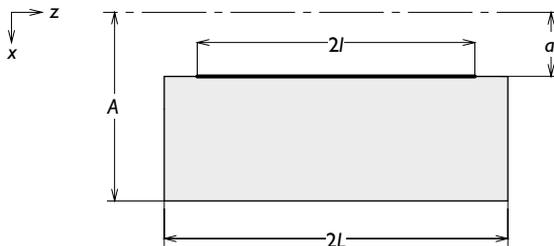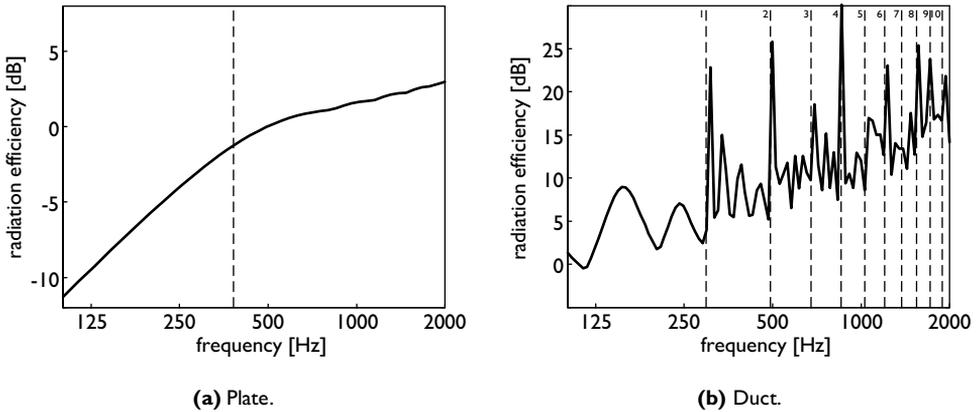


**figure 6.1** Axisymmetric duct model.

**(a)** Plate.                                      **(b)** Duct.

**figure 6.2** Maximum achievable radiation efficiencies. The numbers in the right graph indicate the first cut-on frequency $f_{m1}$, for each Fourier harmonic number $m$.

For the duct system, the behavior is totally different (see figure 6.2(b)). Firstly, the range of efficiencies is much larger. Secondly, an average quadratic increase ($+6$ dB/oct.) of the efficiency can be observed over the whole frequency range. Thirdly, the efficiency spectrum shows many peaks. These peaks are especially high near the cut-on frequencies (see section 2.2.2) of the duct modes (see the dashed vertical lines in figure 6.2(b)).

### 6.2.2  Near cut-on resonances

The peaks in the maximum efficiency graph for the duct are caused by a mechanism that is closely related to the cut-on mechanism for acoustic fields in infinite ducts. This becomes clear when the maximum efficiency of each circumferential harmonic is considered separately. For instance, for circumferential harmonic number $m = 1$ (see figure 6.3), the efficiency reaches a maximum just above the first cut-on frequency $f_{11}$ of the duct. Below the cut-on frequency, the axial wavenumbers $k_{1\mu}$ for the duct modes for harmonic $m = 1$ are all purely imaginary. This means that all duct modes with $m = 1$ are evanescent and thus do not radiate acoustic energy out of the duct. Just above the cut-on frequency, the first axial wavenumber $k_{11}$ is real and the corresponding duct mode starts to propagate and radiate acoustic energy. The transition point is the frequency where the radial wavenumber $\alpha_{1\mu}$ equals the acoustic wavenumber $k$, for a particular value of $\mu$. There, the axial wavenumber $k_{1\mu} = 0$ and this is often referred to as duct resonance for infinite ducts.

The origin of the peaks for the maximum efficiency of the duct cannot be explained solely by the cut-on phenomenon, but it is closely related to it. The peaks in the efficiency are caused by the finite length of the duct combined with a high value of some reflection coefficients at the duct's exits for a duct mode just above its cut-on frequency. This phenomenon will be called *near cut-on resonance* and its origin will be explained next.

Consider equation (2.48) in section 2.2.5, which indicates that acoustic duct modes that are incident in the plane of the duct's exit, are partly transmitted and partly reflected into all other duct modes with the same circumferential harmonic. The reflection coefficient $R_{m\mu\mu}$ describes how much of the duct mode is reflected back into the same duct mode.
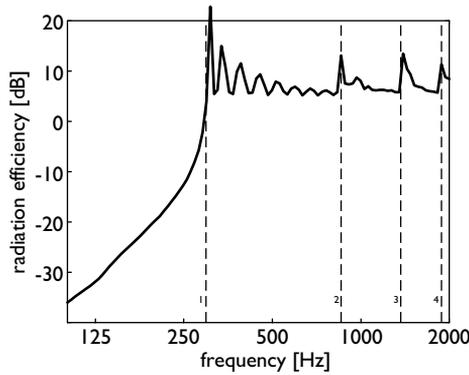
**figure 6.3** Maximum radiation efficiency for the axisymmetric duct model with circumferential harmonic number $m = 1$. The cut-on frequencies of the first four duct modes with $\mu = 1$ to $\mu = 4$ nodal circles are indicated by the dashed vertical lines.

This is called the auto-reflection coefficient here. The reflection coefficient for $\mu \neq \nu$ is called the cross-reflection coefficient. For the duct modes $(m, \mu) = (1, 1)$ and $(m, \mu) = (1, 2)$, the auto-reflection coefficients $R_{111}$ and $R_{122}$ are plotted in figure 6.4.

The auto-reflection coefficient of a particular duct mode is at its maximum near its cut-on frequency. Furthermore, at the cut-on frequencies of other duct-modes with the same circumferential harmonic number, the auto-reflection coefficient is at a minimum. This means that at the cut-on frequency of a mode, most (but not all) of the incident acoustic mode is reflected back into itself, and the cross-reflection (to modes with a different duct mode number $\nu$) is relatively small. At a number of frequencies above the cut-on frequency, the phase of the incident and reflected duct mode match very well and resonance occurs. This causes high values for the pressure inside the duct. Because the auto-reflection coefficient is large, but not unity, acoustic energy is still radiated out of the duct. As a consequence, there are peaks in the radiation efficiency of the duct, because the power radiation is rela-



**(a)** $R_{111}$.



**(b)** $R_{122}$.
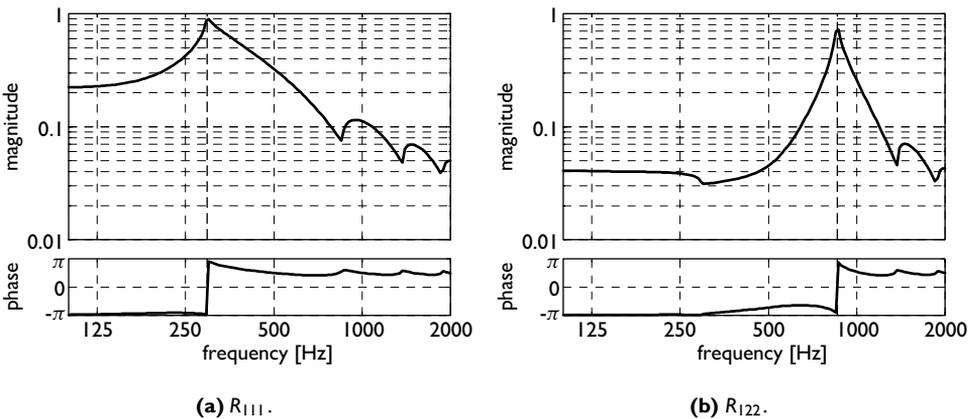
**figure 6.4** Magnitude (top) and phase (bottom) of the duct's exit auto-reflection coefficients. The thick dashed vertical line indicates the cut-on frequency of the corresponding duct mode.

tively large (see figure 6.3 for $f_{11} < f < f_{12}$). Further away from the cut-on frequency the auto-reflection coefficient is much lower, so more of the acoustic duct mode is directly transmitted and/or reflected back into modes with a different radial order $\nu$. There will be less pressure build-up and therefore the resonance effect will be smaller. Note that much of these insights can be directly attributed to analyses with the baffled duct model; it would have been impossible to obtain them from just the Fourier BEM model.

Comparing the auto-reflection coefficients, the maximum value of the of $R_{111}$ is observed to be larger than the maximum value of $R_{122}$ at their respective cut-on frequencies. This translates into a smaller near cut-on resonance for mode $(m, \mu) = (1, 2)$ in figure 6.3.

Another important observation that can be made from the maximum achievable efficiency graphs is that a particular duct harmonic contributes little to the acoustic power radiation below its first cut-on frequency. The maximum achievable radiation efficiency below the first cut-on frequency is often more than 25 dB lower than the efficiencies above the cut-on frequency (see figure 6.3). This means that a particular Fourier harmonic in the excitation field can be neglected if the first cut-on frequency of the duct mode with that Fourier harmonic number is above the frequency range of interest. Because of this, there is a limit on the number of harmonics that needs to be incorporated in an acoustic analysis: a harmonic $m$ only needs to be incorporated if its first cut-on frequency is below the upper limit of the frequency range, or mathematically if $f_{m1} < f_{max}$. This limit was used in figure 6.2(b) where only Fourier harmonics $m \leq 10$ were included in the calculations, because their first cut-on frequencies are below 2000 Hz (see table A.2(a)).

Because of the near cut-on resonance effects, an acoustic analysis seems to be an important part of the design process of the MRI scanner. To put it more simply: vibration levels are not representative for resulting noise levels and vice versa because the two quantities do not relate well for finite ducts. Assessing a design by looking at one of these quantities only is likely to result in erroneous design decisions, as will be demonstrated in section 6.4. On the other hand, if designers are aware of the near cut-on resonance phenomena, they might be able to take these into account in the design. When the cut-on phenomena are manifest, the designer should avoid the coincidence of certain structural resonances with near cut-on resonances, because coincidence results in high noise levels. When the designer is able to shift apart (one of) these resonance frequencies, this can lead to a significant decrease in the noise level, without even a reduction in the vibration level. Of course, this gain is only attainable when there are distinct (resonance) peaks in the velocity spectrum and clearly distinguishable near cut-on resonances. When the vibration level spectrum does not have significant peaks, or the near cut-on resonances are less prominent, the mismatch of resonances is less productive.

### 6.2.3 Conclusions with respect to design

The near cut-on resonances significantly influence the radiation efficiency of the MRI scanner model with constant cross-section. Just above the cut-on frequencies of the duct, the radiation efficiency reaches local maxima. These effects are not common to other externally radiating structures; they are typical of finite ducts. Because of these resonances, it is important to incorporate acoustic analyses in the design process, not only for the low frequency range as for plate-like structures, but also for the middle to high frequency range. When both vibration resonance peaks and near cut-on resonances are manifest, coincidence of the respective resonance frequencies should be avoided.

## 6.3    Some parameters in an acoustic MRI scanner model

### 6.3.1    Excitation of the acoustic system by gradient coil system vibration

*Structural model*

Generally speaking, incorrectly imposing the vibration boundary conditions on acoustic models may lead to significant errors in the predicted noise levels [Seybert et al., 1994]. Errors in the vibration boundary conditions may 'propagate' through the acoustic model and may have serious consequences for the accuracy of the acoustic analysis. Errors in the global level of vibration will show up linearly in the acoustic response, whereas errors in the vibration distribution have a nonlinear effect. Therefore, it is important to have an estimate of the nature and magnitude of errors in the structural model.

The vibration boundary conditions for the acoustic MRI scanner model can be obtained by measurements or numerical structural (FEM) models [Kessels, 1999]. Since the acoustic field in the MRI scanner is assumed not to influence the excitation distribution and level, the errors in the vibration distribution and level are determined solely by errors in the structural model or measurements, that provide the vibration data.

For a design tool, the accuracy requirements for the structural model can be relaxed. With a design tool, it is important to be able to accurately predict structural-acoustic response changes due to design alterations. So, the vibration levels need not be predicted strictly accurate, as long as the vibration distributions, which cause the characteristic level *changes* are correctly computed by the design tool. A full discussion on the desired accuracy of structural MRI models and vibration measurements is outside the scope of this thesis. For that, the reader is referred to Kessels [1999].

*Multiple circumferential harmonics*

An important issue related to the excitation is the number of circumferential Fourier harmonics that should be used in the acoustic analysis. In the first place, this number is determined by the number of circumferential harmonics in the structural analysis. A harmonic that is not present in the vibration field does not have to be incorporated in the acoustic analysis. In the second place, the number of harmonics can be reduced by taking the frequency range of interest into account. In sections 5.3.2 and 6.2 it was found that the radiation efficiency of a Fourier harmonic falls off rapidly below its cut-on frequency. This means that there is virtually no contribution to the noise production of a circumferential Fourier harmonic in the vibration below the first cut-on frequency $f_{m1}$ of the corresponding Fourier-Bessel duct mode. Therefore, the inaccuracy of the boundary conditions for higher circumferential harmonics does not influence the noise levels predicted by the acoustic models.

The importance of the near cut-on resonances is also influenced by the number of Fourier harmonics in the excitation. For the previously presented acoustic analyses, the vibration field did only contain circumferential Fourier harmonic $m = 1$. In practice, this assumption is only valid for homogeneous gradient coil systems (see appendix C). For non-homogeneous gradient coil systems it is very likely that more Fourier harmonics are present in the vibration field. The role of such a multiple harmonic excitation can be illustrated by looking at the acoustic responses of two simplified scanners models with constant cross-section: a model with a single Fourier harmonic excitation ($m = 1$) and a model with multiple Fourier harmonics excitation ($m = 0, 1, 2 \ldots 10$). Both models were

**(a)** Velocity level.

**(b)** Sound power level.

**(c)** Sound pressure level.

**(d)** Radiation efficiency. ——— : maximum.
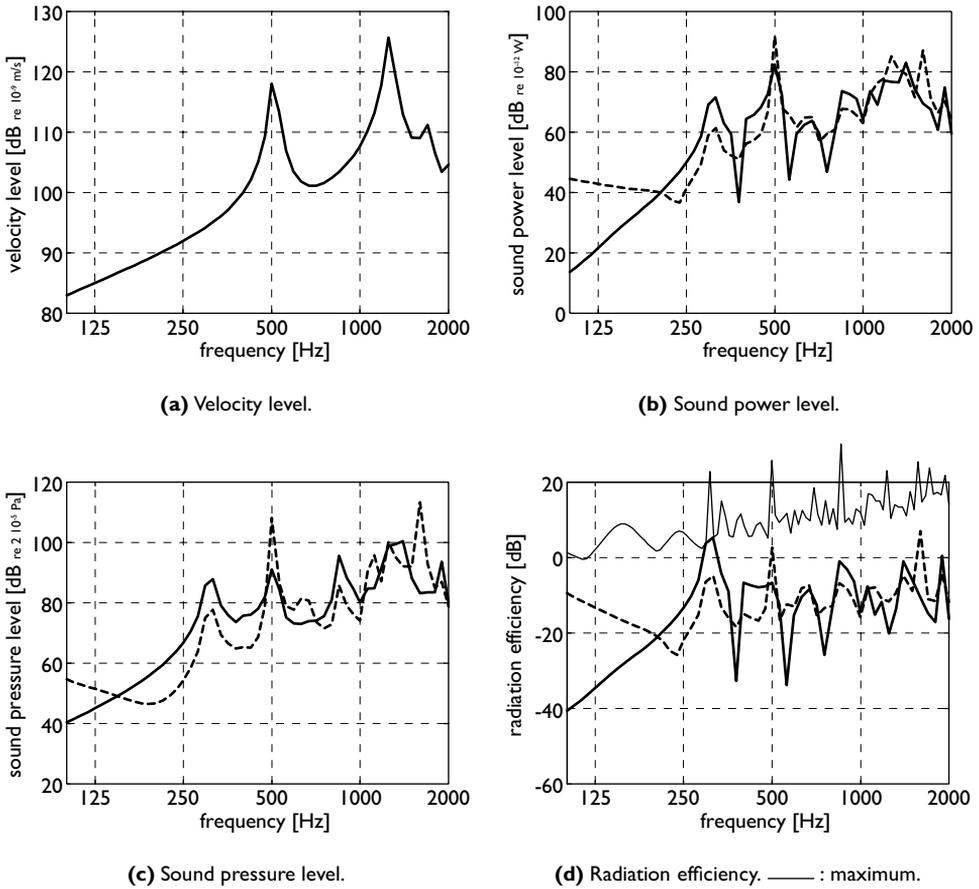
**figure 6.5** Example responses for an MRI scanner model with uniform vibration distribution. ——— : single Fourier harmonic; – – – : multiple Fourier harmonics.

excited with a uniform vibration distribution (i.e. the same vibration amplitude along the axial coordinate) and the total vibration level, summed over all circumferential harmonics was kept equal. The acoustic response curves for both models are shown in figure 6.5.

When the vibration field contains more Fourier harmonics, there are also much more duct modes that are excited and all these duct modes have their respective near cut-on resonances. The effects of these resonances add up in the total response curves so they become less erratic than the curves for single harmonic excitation. This is visible in the efficiency spectra in figure 6.5(d) where the efficiency variation is smaller for the multiple harmonics radiation model. In the response, this results in a more flat curve, although prominent near cut-on resonances can still be present (e.g. the peaks in sound power and sound pressure levels at 500 and 1700 Hz).

Comparing the pressure and power results, there is still a reasonable accordance between the single and multiple harmonic analyses. This means that the simplified acoustic MRI models are certainly insensitive to the number of Fourier harmonics in the analysis.

*Discussion*

In summary, the accuracy of the acoustic analysis is partly determined by the accuracy of the vibration boundary conditions that are imposed. The accuracy of the structural analysis is not influenced by the acoustic analysis, because of the assumed decoupling of structural and acoustic responses. For an acoustic design tool, absolute errors in the levels are not of primary concern. It is far more relevant to be able to predict the changes in the acoustic response due to design alterations. This means that *changes* in vibration level and distribution should be accurately predicted for an acoustic model to be valuable for the designer.

The close resemblance between the acoustic spectra due to single and multiple circumferential Fourier harmonics excitations indicates (but does not prove) that a quiet design resulting from studies with a single harmonic excitation will also be quiet when excited with multiple harmonics. This is consistent with later studies in section 6.4.3. But, to be on the safe side in general, it is recommended to incorporate all circumferential Fourier harmonics of the vibration field which have a significant amplitude *and* for which the corresponding acoustic duct mode is cut-on.

## 6.3.2 Geometric influences

The geometry of a simplified MRI scanner model was found to be very important to explain some of the radiation characteristics. For the designer, it is therefore relevant to know how the acoustics of a real scanner are influenced by geometric design changes. Numerical studies with virtual MRI scanner prototypes are ideally suited for assessing the geometric influences; they tend to deliver results faster and relatively less expensive than measurements on real prototypes would give.

The developed tools are well suited for acoustic design studies of the MRI geometry. For a number of geometric parameters (e.g. inner duct radius $a$ or duct length $2L$) the influence on the MRI acoustics is directly visible in the mathematical formulation of the baffled duct model. For other parameters (e.g. the scanner's outer radius $A$ or varying MRI bore radius), the geometric parameter sensitivities can be obtained with parameter studies deploying Fourier BEM models. In this way, a designer is able to link geometric alterations to changes in the observed response. In this section, this approach was used in some example analyses. These examples show the changes in the scanner's acoustic response due to modification of its geometry, from a simplified to a more realistic shape.

*Numerical experiments*

Four MRI scanner geometries were used to investigate the effects of geometric changes to the MRI scanner model (see figure 6.6). To assess the influence of the outer diameter, a baffled duct model with $N = 30$ Fourier-Bessel modes (see figure 6.6(a)) and a Fourier BEM model with outer radius $A = 1.0$ m (see figure 6.6(b)) were compared. The difference between a sharp and curved edge at the MRI bore's exits was investigated with an additional Fourier BEM model with a curved edge with radius $r = 0.1725$ m. Finally, an MRI model with dimensions similar to a Philips NT MRI scanner was used to assess the influence of a smaller bore diameter in the middle combined with a moderately increasing duct diameter towards the bore's exits.
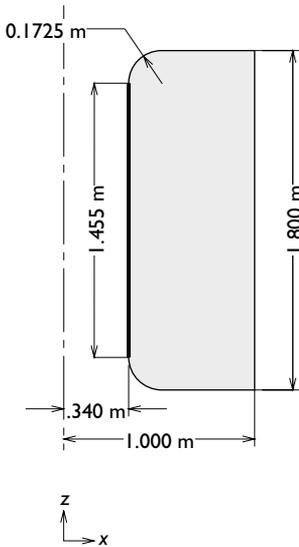
For the gradient coil system, a representative single harmonic vibration distribution was used as the input for an acoustic radiation calculation (see section 5.3.1 and appendix C).
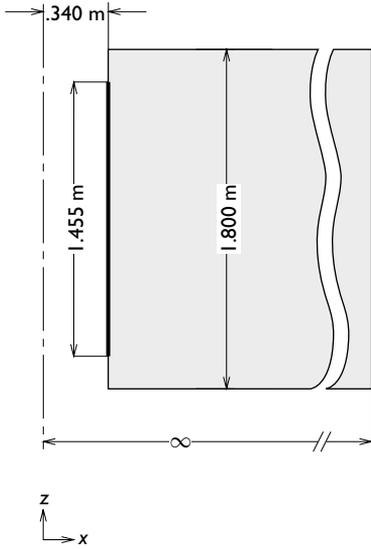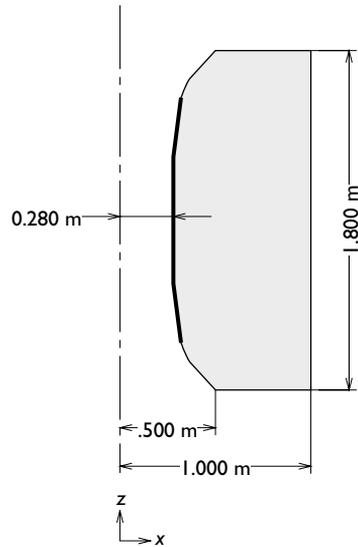
**(a)** Baffled duct, sharp edge.
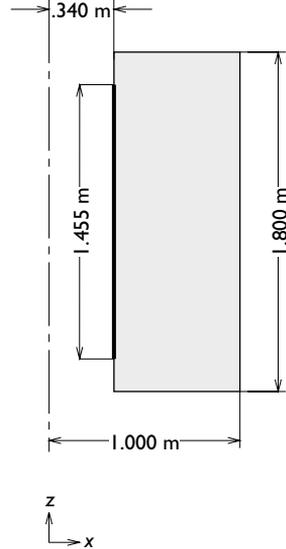
**(b)** Fourier BEM, without casing, sharp edge.

**(c)** Fourier BEM, without casing, curved edge.

**(d)** Fourier BEM, with realistically shaped casing.

**figure 6.6** Axisymmetric models of the MRI scanner with different geometries. The thick line represents the location of the gradient coil system which vibrates. The remainder of the scanner is considered hard-walled.

The vibration was prescribed at the location of the gradient coil system inside the MRI scanner. The remainder of the scanner was considered rigid. For the model in figure 6.6(d) the casing at the location of the gradient coil system was considered to be kinematicly constrained to the gradient coil system and hence the casing vibration exactly follows the gradient coil system vibration. For all these models, the mean square wall pressure, the sound power and the radiation efficiency in the frequency range $100 - 2000$ Hz were computed. The frequency spacing was similar to the spacing described in section 5.2.4: a logarithmic spacing with typically 4 frequencies in each third octave band. As before, the wall pressure level is used as a measure of the acoustic response in the MRI bore, the radiated power level is taken as a measure for the far field response, and the radiation efficiency level is a measure for the effectiveness of the transformation of vibration energy into acoustic energy radiated from the scanner.

*Results and discussion*

The wall pressure level, the sound power level and the radiation efficiency level for all four MRI scanner models are depicted in figure 6.7. In this figure as well as in following figures, the left graphs display the unweighted narrow-band response and the right graphs show the A-weighted responses, integrated or averaged over third octave bands.

The influence of the outer diameter on the acoustic radiation of the gradient coil system is negligible. This can be seen from the response curves for pressure, power and radiation efficiency, where the curves of the baffled duct scanner and the sharp edged scanner are almost indistinguishable. In the pressure graph, there is no visible difference, whereas in the power and radiation efficiency graph, in the low frequency range, the baffled duct model shows a somewhat stronger radiation. Above about 350 Hz the curves are again identical. The 350 Hz limit is determined acoustically. It can be explained by the fact that above this frequency, the acoustic wavelength is smaller than the scanner's outer radius. So, for the acoustic field inside the bore, the 'flanges' of the scanner are 'experienced' as being infinite. This indicates that the response attributes of a baffled duct model also apply to a simplified MRI scanner with a sufficiently large outer diameter.

The effect of changing the sharp edges at the bore's exits into curved edges is negligibly small as well. Some small positive and negative quantitative effects can be observed for pressure, power and efficiency in the third octave levels. The differences for the sound power are somewhat larger than for the sound pressure, which means that the pressure field in the MRI bore is only marginally affected by the edge curvature. The prominent near cut-on resonance effects are unaffected by the edge curvature change. This means that the cut-on frequencies should still be computed with the smallest bore radius $r = 0.3405$ m, not with the radius of the exit ($r = 0.3405 + 0.1725 = 0.513$ m). It seems that the cut-on effects are determined by the radius of the part of the bore with constant cross-section.

The presence of a realistically shaped casing around the gradient coil system shifts the near cut-on frequency resonances. This is caused by a decrease in the minimum radius of the bore, which shifts the cut-on frequencies to higher frequencies. This behavior can be illustrated by a maximum achievable radiation efficiency analysis (see section 6.2.1 for details) for the curved-edge bore and the bore with realistically shaped casing (see figure 6.8). Clearly, the near cut-on resonance effects are present in both the curved-edge MRI bore and the MRI with casing. The cut-on frequencies of the latter configuration are shifted to higher values because the part of the bore with constant cross-section has a
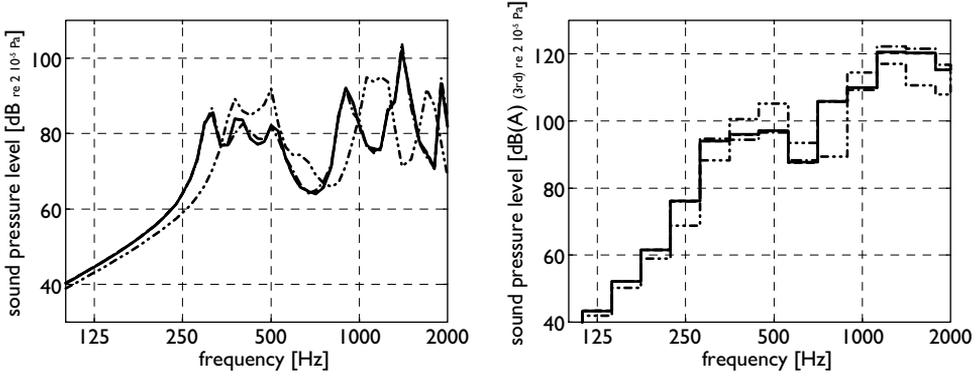
**(a)** Sound pressure level at the wall.
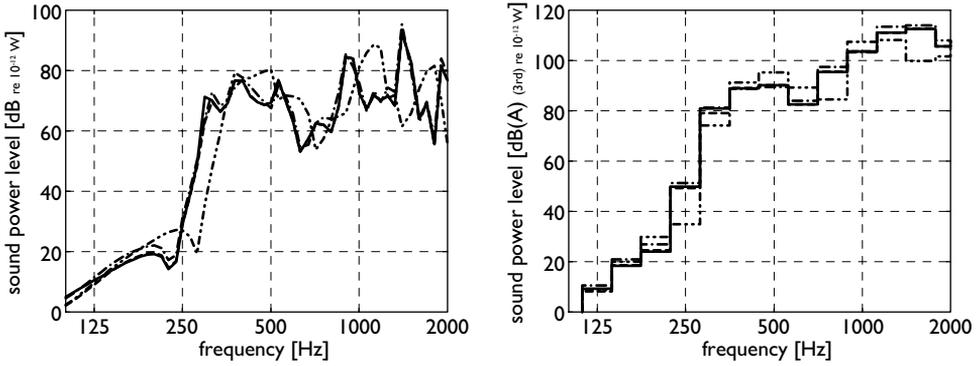


**(b)** Radiated sound power level.
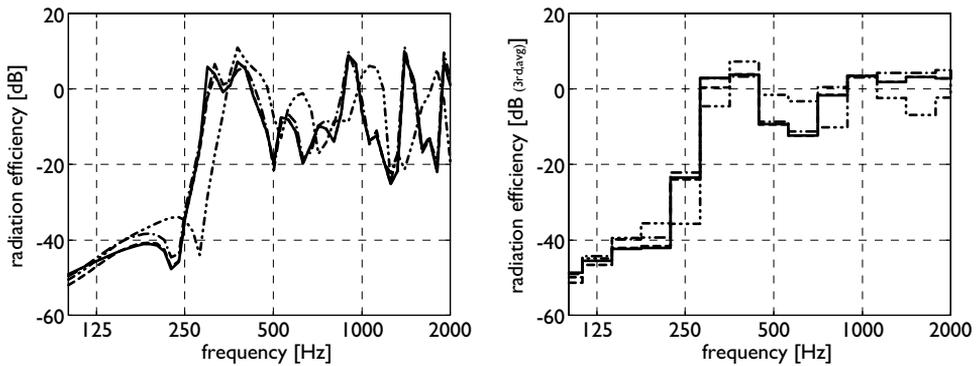


**(c)** Radiation efficiency level.

**figure 6.7** Acoustic responses for MRI scanner with different geometries. ——— : baffled duct scanner; – – – – : scanner without casing, sharp edge; – · – · · : scanner without casing, curved edge; – · · – · · : scanner with realistically shaped casing.

**(a)** MRI with curved exits.                    **(b)** MRI with realistically shaped casing.
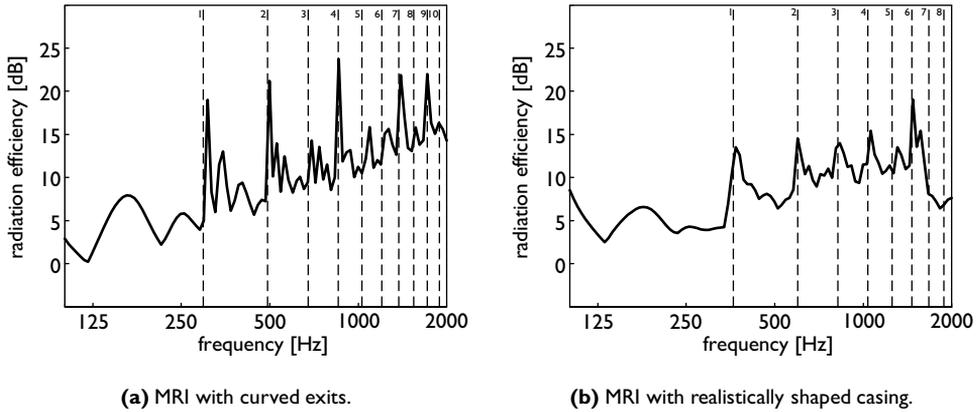
**figure 6.8** Maximum achievable radiation efficiencies for the MRI models. The numbers in the graphs indicate the first cut-on frequency for each Fourier harmonic number *m*. The minimum radius of the MRI bore's ($a = 0.34$ m and $a = 0.28$ m, respectively, for the left and right graph) was used to compute the respective cut-on frequencies.

smaller radius. Also, a decrease of the efficiency is found above the first cut-on frequency for Fourier harmonic $m = 7$, which was not present in the other models. Moreover, the near cut-on resonance effects for the MRI with casing are less prominent than for the bore with curved edges. The resonance peaks are less sharp and much lower. Comparing the results in figure 6.8(a) with the results for the sharp edged bore in figure 6.2(b) reveals that the curved edges at the bore's exits in comparison with sharp edges also decrease the near cut-on resonance peaks.

From the observed changes in the maximum achievable efficiency spectra, it is assumed that a gradually changing bore radius will cause a decrease in the prominence of the near cut-on resonances. To confirm this assertion, a study was made of an MRI model for which the bore geometry is conical towards both exits (see figure 6.9(a)). The bore's minimum and maximum radius were taken identical to the MRI model with realistic casing, but the latter model does not have a constant radius change per unit length.

For the conical MRI scanner model, the maximum achievable radiation efficiency was computed (see figure 6.9(b)). The peaks in the resulting maximum efficiency spectrum are much lower than for the other MRI scanner models. Furthermore, the peaks in the spectrum do not correlate with the cut-on frequencies based on the bore's minimum radius. Thirdly, the global steepness of the spectrum is smaller. It seems that the MRI bore should have a part with constant radius for significant resonances to occur.

*Conclusions with respect to design*

From the presented analyses, some important conclusions for the MRI scanner's radiation characteristics can be drawn. Changing the geometry of the bore influences the near cut-on resonances significantly. The radius of the part of the bore with constant cross-section determines the cut-on frequencies. Also, a gradually changing bore radius decreases the height and sharpness of the resonance peaks. Hence, the geometry of the bore casing might provide the acoustic engineer with some design freedom to decrease the possible importance of the near cut-on resonances in the acoustic response of an MRI scanner.
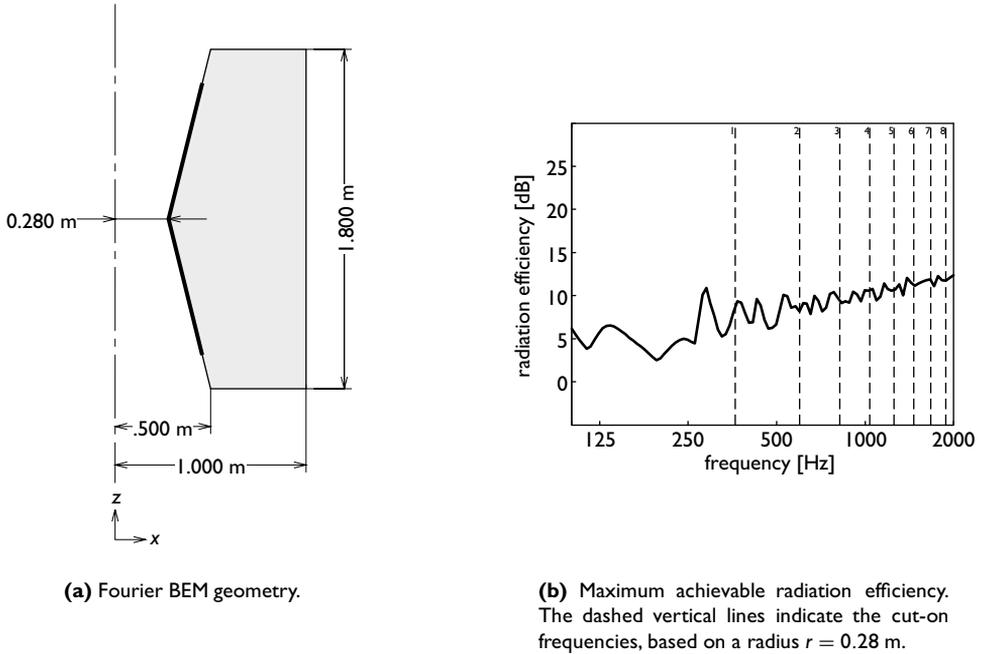
**(a)** Fourier BEM geometry.

**(b)** Maximum achievable radiation efficiency. The dashed vertical lines indicate the cut-on frequencies, based on a radius $r = 0.28$ m.

**figure 6.9** MRI scanner with a two-sided conical bore.

### 6.3.3  The acoustic influence of the scanner room

In the previous section, it was shown that changes to the geometry of the MRI scanner can have a considerable influence on its acoustic radiation characteristics. But besides the geometry of the scanner itself, the geometry and acoustic behavior of its working environment can be of influence.

The direct working environment of the scanner is the room in which the scanner is located. The room dimensions are normally larger than the maximum acoustic wavelength of the noise. This means that the sound power radiation of the scanner is not expected to be significantly influenced by the room properties. It is recognized that for low frequencies, standing acoustic waves might play a role in the pressure distribution in the room, but the low frequency components of the radiation are only of minor significance for the total sound production. Therefore, it is not necessary to incorporate the environment in the MRI scanner model. For the acoustic MRI scanner design, it is sufficient to calculate the sound production of the scanner in free space. This is fortunate, because for design purposes it would be impractical or even impossible to account for the room conditions, since the scanner rooms are very different from hospital to hospital.

### 6.3.4  The acoustic influence of a patient in an MRI scanner

Another important operating condition for the scanner is the presence of a patient in the scanner bore, which can possibly influence its radiation characteristics. If the presence of the patient would have significant effects, then this should be accounted for in the acoustic design of the scanner. Whether and to what extent the presence of a patient in the scanner affects the design of the scanner is the topic of the remainder of this section.

*Modeling*

*Fourier BEM model.*    To assess the influence of the presence of a patient in the MRI bore on the acoustic response of the scanner, a Fourier BEM model of the scanner and patient was made in b*Ard* [1998]. For the scanner model, the geometry with realistically shaped casing was chosen (see figure 6.10). This geometry is closest to an MRI scanner's geometry that is in use in practice. The patient geometries were derived from realistic data [Burkhard and Sachs, 1975; Nagel, 1988], but because of the use of Fourier BEM, the geometry of the patient was made axisymmetric. A representative single harmonic vibration distribution was chosen as excitation of the acoustic model (see section 5.3.1 and appendix C).

*Acoustic impedance of the patient.*    It proved to be difficult to build an acoustic model for a patient. Because of the total lack of appropriate data, the acoustic properties of the patient could only be roughly estimated. Burkhard and Sachs [1975] have found negligible influence of skin impedance on the acoustic response in the assessment of hearing aids (" … Being hard headed does not affect significantly the sound … "). Therefore, the skin was modeled as acoustically hard. However, the acoustic properties of clothing could possibly influence the acoustic response of the MRI scanner. From concert hall acoustics studies [e.g. Beranek, 1969], the resistive behavior of clothing could be roughly approximated. The reactive properties of the clothing seem to be uninvestigated. Therefore, a simple and generally usable expression of the absorption behavior of patient clothing as a function of frequency is not available and is unlikely to exist. The impedance behavior of the clothing depends on a large number of parameters: on frequency, on the type of clothing, on the clothing thickness, on the angle of incidence of the acoustic field, etc. The task to develop a reliable acoustic model for the patient's clothing is likely to equal the amount of work required to build an acoustic MRI scanner model and is therefore clearly outside the scope of this thesis. As an alternative approach, parameter studies were chosen to assess the influence of clothing absorption.

In studies of concert hall acoustics, Beranek [1969] found that the absorption coefficient $\alpha$ of audience ranges from $\alpha = 0.39 - 0.94$ in the frequency range of interest. An expression for the real part of the impedance of the clothing can be derived from these data as will be shown next.
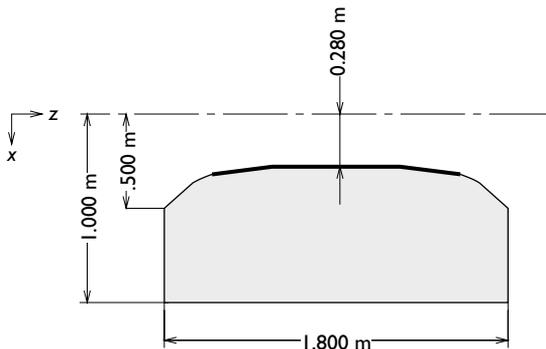


**figure 6.10** Axisymmetric MRI scanner model. The thick line represents the location of the realistically shaped casing that is assumed to vibrate. The remainder of the casing is considered rigid.

If plane waves in the air impinge in the normal direction upon a plane (in this case clothing) of specific impedance $z_p$, reflection will take place; the ratio between incident wave pressure $p_i$ and reflected wave pressure $p_r$ is defined as [e.g. Zwikker and Kosten, 1949]

$$r = \frac{p_r}{p_i} = \frac{z_p - z_0}{z_p + z_0}, \tag{6.1}$$

with $z_0$ as the specific impedance of the air. This ratio is called the complex reflection coefficient. The energy absorption coefficient is then defined as

$$\alpha = 1 - |r|^2 = 1 - \left| \frac{z_p - z_0}{z_p + z_0} \right|^2. \tag{6.2}$$

Rewriting this yields

$$|z_p - z_0| = |z_p + z_0|\sqrt{1 - \alpha}. \tag{6.3}$$

If $z_p$ is assumed to be purely real and its value is larger than $z_0$, the following expression for impedance $z_p$ can be derived:

$$z_p = \frac{1 + \sqrt{1 - \alpha}}{1 - \sqrt{1 - \alpha}} z_0. \tag{6.4}$$

The specific impedance of air is defined as

$$z_0 \equiv \rho_0 c_0, \tag{6.5}$$

with $\rho_0 = 1.21$ kg/m$^3$ as the air density and $c_0 = 343$ m/s as the speed of sound in air. With these the resistive part of the clothing impedance ranges from $z_p \approx 700 - 3400$ Pa s m$^{-1}$. When the clothing absorption coefficient equals one, i.e. total absorption, the impedance of the clothing is identical to the specific impedance of air: $z_p = z_0 = 415$ Pa s m$^{-1}$. It should be stressed that these values are very rough estimates, since they only apply to normal incidence of plane waves and the possibly complex nature of the clothing impedance was totally disregarded.

*Numerical experiments*

Two series of numerical experiments were performed to assess the influence on the acoustic field of the presence of a patient in the MRI scanner. In the first series, the influence of the patient's position was assessed (Experiment 1). In the second series, the influence of the impedance of the patient's clothing was investigated (Experiment 2).

*Experiment 1: patient position.*   The effect of the patient's position in the bore was investigated by two computations: with the patient's head located in the center of the scanner (position A), and with the patient's geometrical center in the center of the scanner (position B) (see figure 6.11).

The position of the patient relative to the scanner depends on the part of the patient's body that needs to be imaged. The imaging section of the scanner is located at the isocenter of the bore. Thus, the patient position A relative to the scanner in figure 6.11(a) is typical of head imaging and the patient position B in figure 6.11(b) is typical of lower abdominal imaging. The patient was modeled as acoustically hard in both simulations.

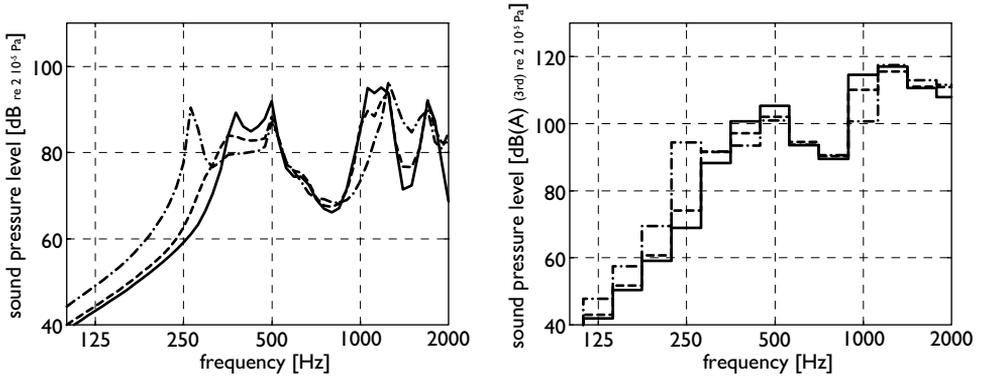**(a)** Position A.    **(b)** Position B.
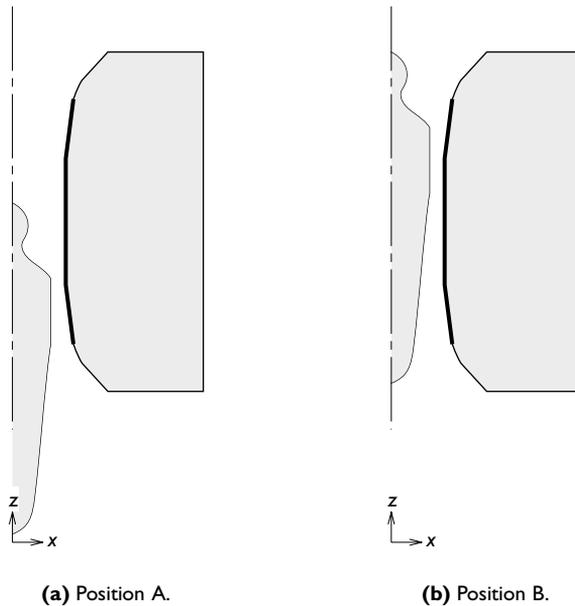
**figure 6.11** Axisymmetric models of MRI scanner with patient at different positions in the bore.

*Experiment 2: patient impedance.*    To assess the influence of the patient's clothing impedance on the acoustic field radiated by the scanner, the clothing impedance was varied. Four different values (i.e. $z_p = 415, 1500, 3000$, and $\infty$ Pa s m$^{-1}$) were taken for the clothing impedance, all for a patient in position A in the scanner. The impedance boundary condition was applied to the whole patient, and the impedance was assumed to be independent of the frequency. The impedance value $z_p = \infty$ corresponds to a boundary being acoustically hard. The influence will be assessed from the results for the mean square value of the acoustic pressure at the wall of the scanner, from the radiated power, and from the radiation efficiency.

*Results and discussion*

*Experiment 1: patient position.*    The results for the mean square sound pressure (spatially averaged at the wall), the sound power and the radiation efficiency as a function of frequency for varying patient's position in the scanner are shown in figure 6.12. The left graphs display the unweighted narrow-band responses and the right graphs show the A-weighted responses, integrated or averaged over third octave bands.

Above 500 Hz, the third octave levels for power and radiation efficiency for the MRI scanner with patient do not change very much compared to the same quantities for the scanner without patient. The radiation below 200 Hz is increased by the patient's presence. Between 200 and 500 Hz the differences are relatively small. The wall sound pressure spectra exhibit the same behavior as the sound power spectra, although the differences are larger. This is not surprising, as the wall pressure is a local acoustic quantity and is likely to be influenced more by local changes. For low frequencies there is also considerable difference between the two models with the patient in position *A* and *B*, respectively. For the empty scanner, the cut-on frequencies for the first four duct modes for harmonic

(a) Sound pressure level at the wall.
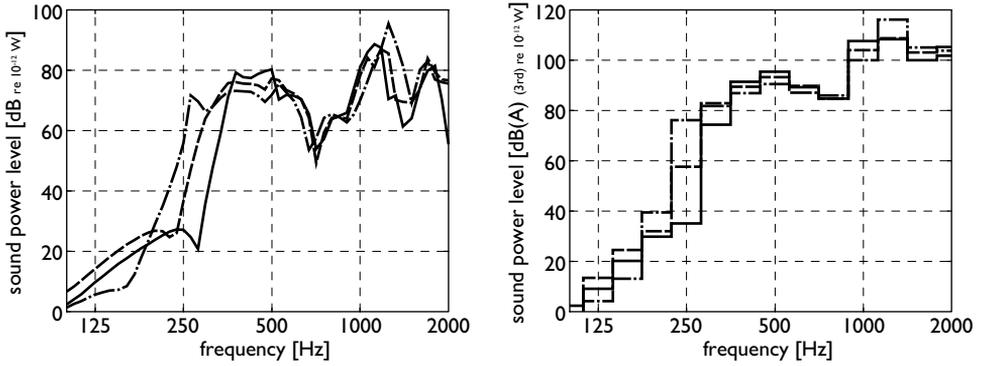


(b) Radiated sound power level.
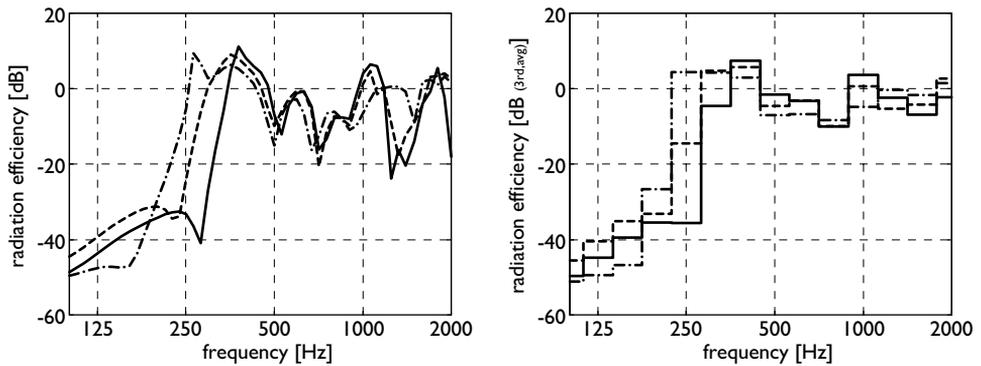


(c) Radiation efficiency level.

**figure 6.12** Acoustic responses for MRI scanner without and with an acoustically hard patient. ——— : empty scanner; scanner with patient, - - - - : position A; –·–·· : position B.

$m = 1$ are: $f_{1\mu} = 296, 855, 1368$, and $1877$ Hz (see table A.2(a)). In the narrow-band spectrum for the radiation efficiency level for the scanner without patient, the spectrum peaks just above these frequencies. The presence of a patient seems to shift the cut-on frequencies downwards, indicated by the down-shift of the radiation efficiency peaks (see figure 6.12(c), left). The effect of this down-shift of cut-on frequencies is also visible in the power and pressure responses. The third octave levels show that this effect is strongest for low frequencies.

*Experiment 2: patient impedance.*   The mean square sound pressure averaged over the wall, the sound power, and the radiation efficiency as a function of frequency, for varying impedance of the patient's clothing, are shown in figure 6.13.

Not surprisingly, the effect of a decreased clothing impedance is a decrease and smoothening of the acoustic spectra. With decreasing impedance, the clothing increasingly absorbs more of the acoustic energy and the net radiated acoustic energy decreases. But the effects are quite moderate and even less than for the analyses with varying patient positions.

A consequence of increasing the clothing impedance is that the down-shift of the cut-on frequencies observed in Experiment 1 seems to be canceled out. The total effect of the presence of a patient with absorbing clothing in the scanner is a very moderate decrease of sound power and pressure levels, and it decreases the radiation efficiencies, especially near the cut-on frequencies. These findings are experimentally confirmed by the research of Hedeen and Edelstein [1997]. Hence, the influence of the patient's presence is noticeable but does not change the typical radiation characteristics.

*Conclusions with respect to design*

The influence on the acoustic response of the presence of a patient inside an MRI scanner was assessed. Simulations were performed for several configurations using acoustic Fourier BEM models. The influence on the acoustic field of the patient's position and patient's clothing impedance were investigated in two series of numerical studies. The simulations showed that very moderate quantitative effects can be expected from the presence of a patient in the scanner, but showed no significant influence on the typical radiation characteristics. It is therefore unlikely that significantly different designs will result from an acoustic model for the MRI scanner with or without a patient. This means for the effectiveness as a design tool, that not incorporating the patient in an acoustic model of the MRI scanner has no practical consequences.

## 6.4   Design studies for an MRI scanner with layered gradient coil system

To demonstrate the potential of the developed acoustic tools for the MRI scanner, four parameter studies ware performed for different MRI scanner models. The models differed with respect to the geometry of the bore and the number of circumferential harmonics in the excitation. The model configurations are shown in table 6.1. With these models, the design influence of multiple circumferential harmonics in the excitation and the influence of the casing shape were investigated.
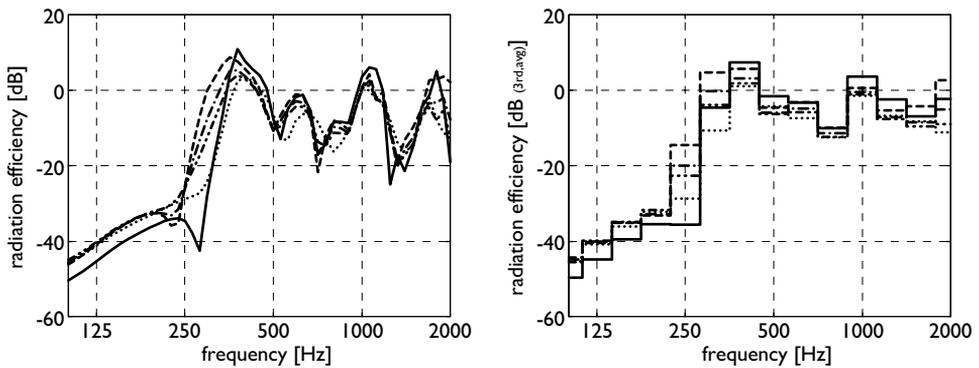
To compute the vibration excitation in these studies, a layered finite element model of the gradient coil system was used. This finite element model was excited with a representative Lorentz force distribution (identical to the one used in section 5.3.1 and the
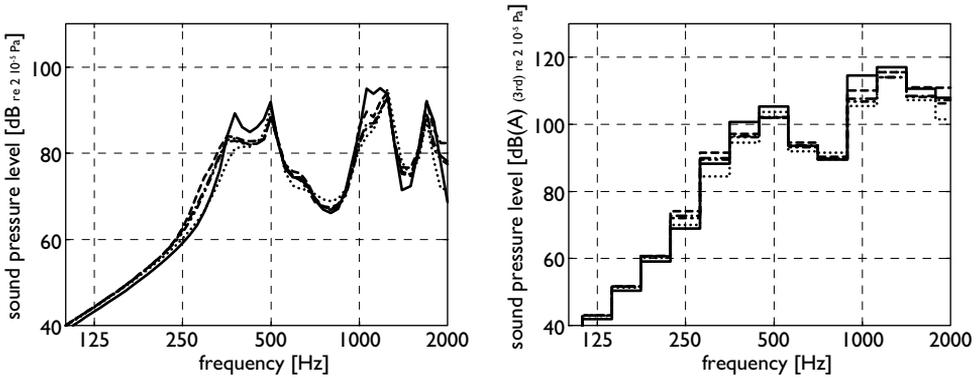
**(a)** Sound pressure level at the wall.
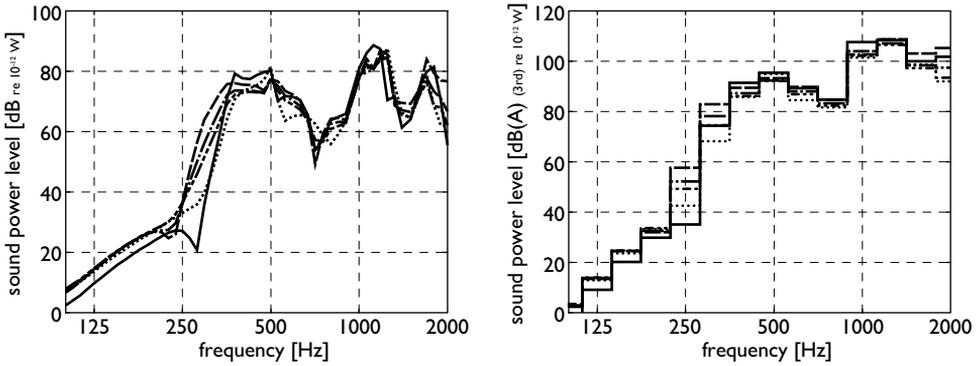


**(b)** Radiated sound power level.



**(c)** Radiation efficiency level.

**figure 6.13** Acoustic response for MRI scanner for different absorption characteristics for the patient (position A). ——— : empty scanner; scanner with patient, ---- : $z_p = \infty$; –·–··· : $z_p = 3000$; –··–··· : $z_p = 1500$; ········ : $z_p = z_0 = 415$.

**table 6.1** Model configurations for MRI scanner design studies.

|  | study 1 | study 2 | study 3 | study 4 |
|---|---|---|---|---|
| # harmonics | single | single | multiple | multiple |
| casing shape | none | realistic | none | realistic |

following sections, see appendix C). The response of the FEM model was computed with the SATURN package [Kessels et al., 1998]. In SATURN it is possible to perform automatic parameter studies. This feature was used here to assess the influence of thicknesses of the different material layers in the gradient coil system.

A layered gradient coil system was modeled consisting of five layers with different material properties (see figure 6.14): a conductor layer (copper-epoxy composite, thickness $t_1$), a damping layer (epoxy, thickness $t_2$), a undamped stiff layer (glass, thickness $t_3$), and again a damping layer (epoxy, thickness $t_4$) and a conductor layer (copper-epoxy composite, thickness $t_5$). The properties of the layer materials can be found in appendix C. The gradient coil system build-up and materials were chosen to resemble a realistic gradient coil system.

The total thickness of the gradient coil system was kept constant $t_{tot} = 100$ mm in the parameter study. The thicknesses of the conductor layers were also kept constant: $t_1 = t_5 = 10$ mm. Then the thickness of the first damping layer and the stiff layer were varied: $t_2 = 5 \ldots 35$ mm and $t_3 = 5 \ldots 35$ mm, respectively. The thicknesses were both increased in seven steps of 5 mm, making a total of 49 different gradient coil system designs. With constant thicknesses $t_1$, $t_5$, and $t_{tot}$, the fourth (damping) layer thickness $t_4$ is a dependent variable: $t_4 = t_{tot} - \sum_{i=1,2,3,5} t_i = 10 \ldots 70$ mm.

The acoustic response of the MRI models was computed with the program bArd [1998] after every structural analysis of the gradient coil system. If the radiated sound power would be the only interesting acoustic quantity, then the radiation modes reduction technique could be used here, because the shape of the radiating surface is not influenced by the parameter variations (see also chapter 4). This significantly speeds up the acoustic analysis part of the parameter study and hence speeds up the total parameter design study.
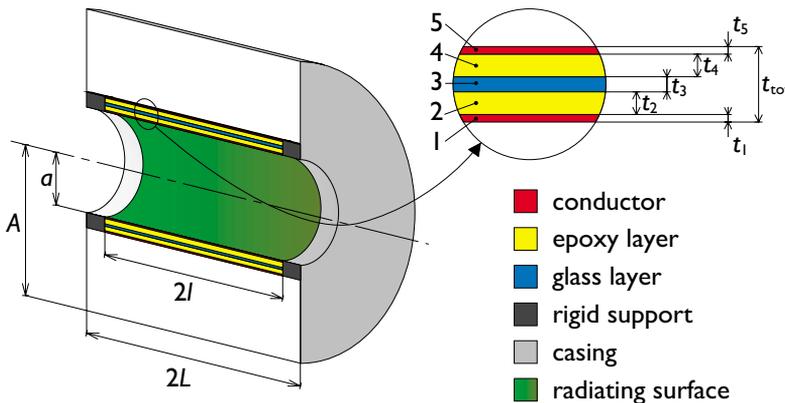


**figure 6.14** MRI model with layered gradient coil system, without casing.

However, an additional objective of these studies was to further evaluate the adequacy of sound power compared to sound pressure in the bore as a design objective function. Therefore, the radiation modes formulation could not be used for all studies.

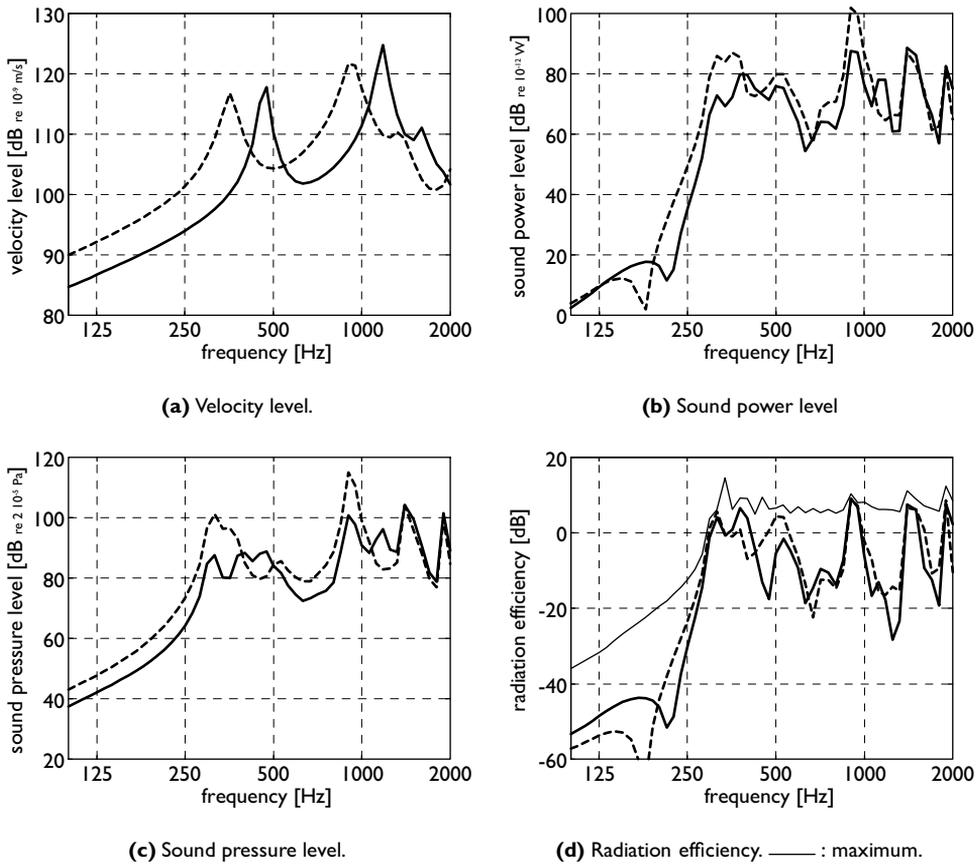### 6.4.1 Study 1: MRI scanner with single harmonic excitation, without casing

For an acoustic analysis of the scanner, the (radiating) geometry of the scanner has to be defined. For the first design study, an MRI scanner without bore casing was modeled. For this model, the gradient coil system is in direct contact with the acoustic fluid and therefore radiates sound directly into the bore of the scanner. The remainder of the scanner was assumed to be rigid. For the excitation, only circumferential harmonic $m = 1$ was used. This configuration is similar to the MRI model with sharp edges that was used in section 6.3.2 (see figure 6.6(b)).

The response surfaces that result from this design study, for the velocity level ($L_v$ re $10^{-9}$ m/s, mean square value, spatially averaged), the sound power level ($L_W$ re $10^{-12}$ W), and the sound pressure level ($L_p$ re $2 \cdot 10^{-5}$ Pa, mean square value, spatially averaged over 40 field points in the scanner bore) are depicted in figure 6.15. A first glance at the response surfaces reveals that the spread in the velocity levels is only 6 dB(A), whereas the spread for the power and pressure responses is almost 15 dB(A). A comparison between the response surfaces for velocity level and sound power level shows that they do not display similar parameter sensitivities. This means that gradient coil system designs with low vibration levels do not necessarily coincide with designs that have low sound power levels. The cause of this poor correlation can be explained by looking at the response spectra of two designs: a design with low power level (design 1$P$) and a design with low velocity level (design 1$v$). The frequency spectra for these designs are shown in figure 6.16. The dimensions and total level values for these designs can be found in table 6.2, which presents a summary of results for all four design studies.

The thinner stiffness layer $t_3$ of design 1$v$ results in a decrease in velocity level, combined with a lowering of the eigenfrequencies in figure 6.16(a). A consequence of this frequency shift is that the eigenfrequencies are located closer to the cut-on frequencies of the bore. This results in an increased power and pressure level at these frequencies (see figures 6.16(b) and 6.16(c)).
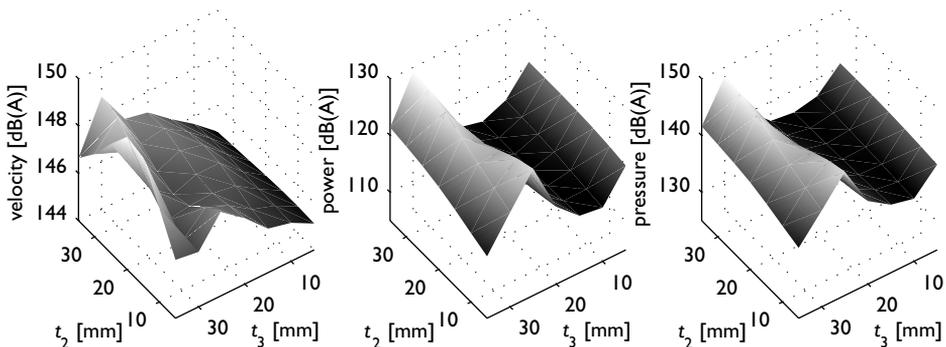


**figure 6.15** Response surfaces for MRI scanner parameter study 1: no casing and single circumferential harmonic excitation.

**(a)** Velocity level.

**(b)** Sound power level

**(c)** Sound pressure level.

**(d)** Radiation efficiency. ——— : maximum.

**figure 6.16** Response curves for MRI scanner models with different gradient coil system designs, with single circumferential harmonic excitation, without casing. ——— : design 1*P*, ---- : design 1*v*.

The correlation between sound power and sound pressure level is very good. Apart from the levels, the pressure and power response surfaces evince almost identical behavior. Also for designs 1*P* and 1*v*, the frequency spectra of sound power and sound pressure correlate well. This means that a low sound power design is also a low sound pressure design here. For this study, this means that the pressure results supply no additional information for the designer and that the power results suffice to evaluate the noise production of a design. This close agreement makes the pressure calculations superfluous, and thus it is possible to decrease the computational effort for the acoustic analyses by using the radiation modes reduction technique as described in section 4.3. For the present study, this would mean that the computation time for the *acoustic* analyses would be reduced by a factor of almost 48 (a single acoustic analysis plus an eigenvalue analysis, instead of 49 complete acoustic analyses). The calculation time for the power, based on the modal contribution coefficients and modal radiation efficiencies, is negligibly small.

### 6.4.2  Study 2: MRI scanner with single harmonic excitation and realistic casing

A second design study was performed, now with an acoustic MRI scanner model with realistically shaped casing. The radiating part of the geometry of the scanner was chosen as the part of the casing that is the closest to the gradient coil system (see figure 6.17). The remainder of the casing is considered rigid. For the excitation, only circumferential Fourier harmonic $m = 1$ was used. Similar to the analysis in section 6.3.2, the computed gradient coil system vibration is directly imposed on the radiating part of the casing. This configuration is represents a direct kinematic coupling of the gradient coil system and the casing in the bore. In a real MRI scanner, the coupling between gradient coil system and casing is considerably more complex, but can, as a first approximation, be modeled as outlined here. The direct coupling was chosen to facilitate the comparison of the vibration levels between the design studies without and with casing, respectively.

The response surfaces that result from the design study with this MRI scanner model, for the velocity level ($L_v$ re $10^{-9}$ m/s, mean square value, spatially averaged), the sound power level ($L_W$ re $10^{-12}$ W), and the sound pressure level ($L_p$ re $2 \cdot 10^{-5}$ Pa, mean square value, spatially averaged over 40 field points in the scanner bore) are depicted in figure 6.18. Again, as for the MRI model without casing, the correspondence between the velocity level and sound power level is poor, and the correlation between sound power and sound pressure level is rather good. Comparing the response surfaces for this MRI model and the model without casing reveals that the optimum design in terms of power or pressure is different. This means that the most quiet design for a gradient coil system in a scanner without casing might not be the optimum design for a scanner with casing. Note that the design with the lowest sound power level (design 2*P*, $t_2 = 25$ mm, $t_3 = 30$ mm) is not the exactly the same as the design with the lowest pressure value (design 2*p*, $t_2 = t_3 = 35$ mm). However, both designs lie in the same region of optimum designs, and the differences between the sound pressure and sound power values of designs 2*p* and 2*P* are relatively small ($<$ 1 dB). Hence, there is no preference for one of these optima, judging from only these data.

To understand why a quiet gradient coil system design for the scanner without casing is not optimal for the scanner with casing, a closer look at the frequency responses is required. For design 2*P* and the design with the lowest velocity level, design 2*v*, the levels
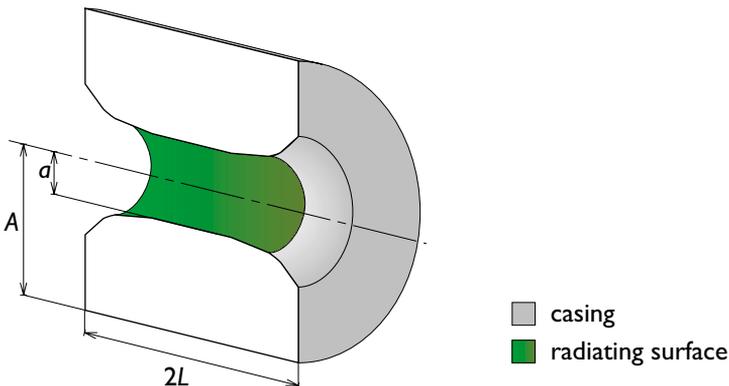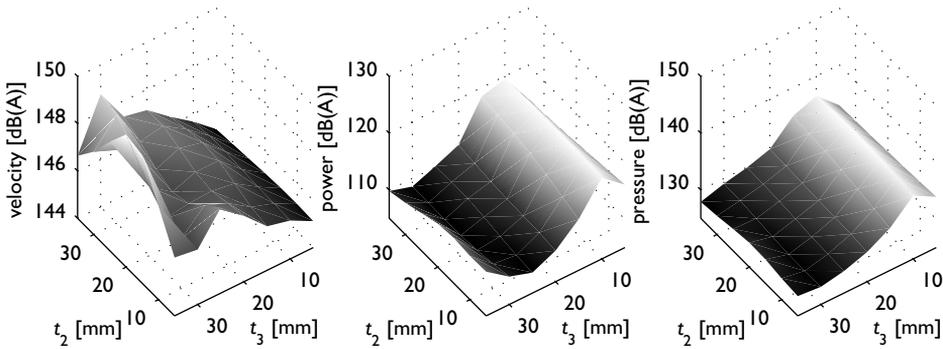


**figure 6.17** MRI model with layered gradient coil system (not shown) and realistically shaped casing.

**figure 6.18** Response surfaces for MRI scanner parameter study 2: with realistically shaped casing and single circumferential harmonic excitation.

are given in table 6.2, and the frequency response curves are given in figure 6.19. Note that design 2*v* is structurally equivalent to design 1*v*.
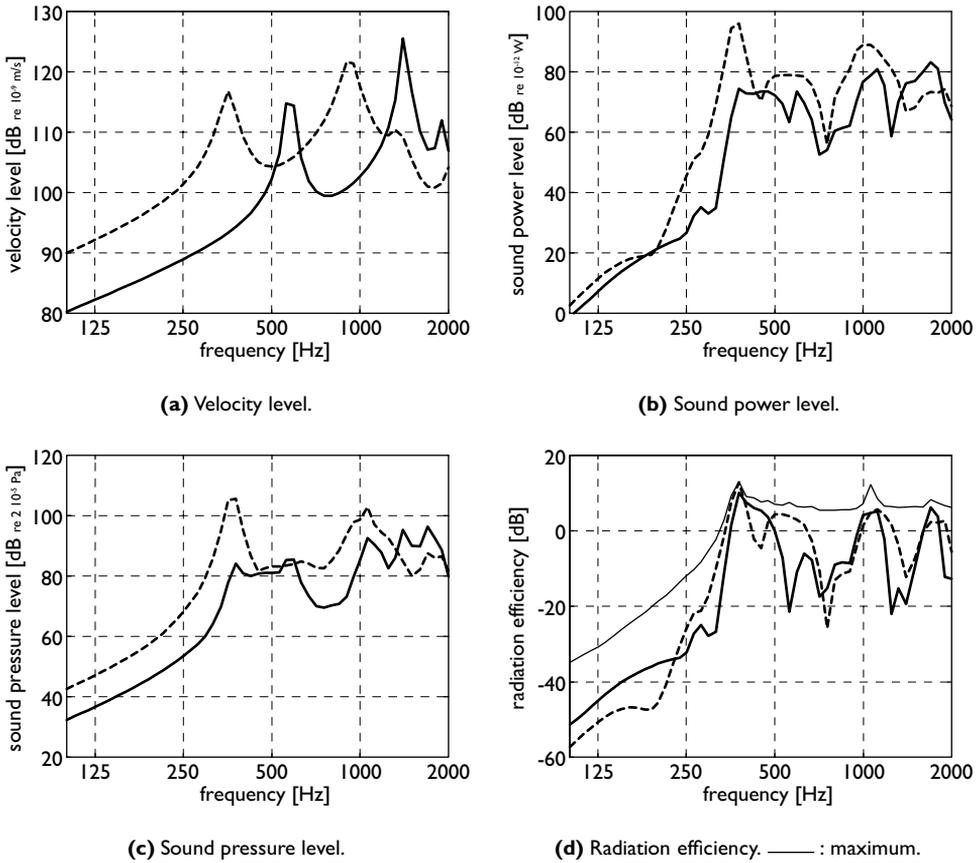
The most quiet gradient coil system designs, in this study and in the study of the scanner without casing, have in common that the peaks in the velocity level do not coincide with near cut-on resonances of the bore. But, the cut-on frequencies for the model without casing and the model with casing are different. Because of the smaller minimum bore radius for the latter model, its cut-on frequencies are higher. Comparing the velocity level spectra in figures 6.16(a) and 6.19(a) shows that the velocity spectrum of the optimal design for the scanner with casing is also shifted towards higher frequencies. This is accomplished by increasing the thickness of layer 3, the stiff glass layer.

Comparing the results for the scanner without and with casing, it is observed that the response surfaces for sound power levels and sound pressure levels for the scanner with casing are lower. This means that the same amount of vibrational energy results in lower production of acoustic energy for the scanner with casing. A justifiable conclusion here is that the scanner with casing may be about 6 dB(A) quieter, for single circumferential harmonic excitation, because of its shape.

### 6.4.3 Studies 3 & 4: MRI scanner design for multiple harmonics excitation without and with casing

The design studies of the previous sections were carried out with a single circumferential harmonic ($m = 1$) excitation. For that type of excitation, the optimum gradient coil system designs are characterized by a mismatch between peaks in the velocity level spectrum and near cut-on resonance peaks in the radiation efficiency spectrum. But, the study in section 6.3.1 showed that for multiple circumferential harmonics excitation, the effect of the cut-on resonances becomes smaller. Therefore, it is interesting to look whether multiple harmonic excitation will change the outcome of the design studies. This aspect will be investigated here.

For the design studies with multiple circumferential harmonics excitation, again both an acoustic MRI model without casing (study 3) and a model with casing (study 4) were used. These models are identical to the models in design studies 1 and 2, respectively, except for the excitation. For the excitation, the representative Lorentz force distribution (see

**(a)** Velocity level.



**(b)** Sound power level.



**(c)** Sound pressure level.



**(d)** Radiation efficiency. ——— : maximum.

**figure 6.19** Response curves for MRI scanner models with different gradient coil system designs, with single circumferential harmonic and realistically shaped casing. ——— : design 2*P*; - - - - : design 2*v*.

appendix C) was applied not only for the circumferential harmonic $m = 1$, but for the harmonics $m = 0, 1, \ldots 5$. The resulting vibration distribution was again computed with the SATURN package [Kessels et al., 1998].

The previous parameter studies showed that sound power and sound pressure respond similarly to design alterations, and are therefore interchangeable as design objective functions. For practical reasons, it was chosen to assess the acoustic performance of the scanner models with the radiated acoustic power only, because this enabled the use of the radiation modes reduction technique for the acoustic analyses (see section 4.3). This drastically accelerated the acoustic calculations of the design studies.

The response surfaces for the velocity level and sound power level of both the MRI scanner models without and with casing, are displayed in figure 6.20. Comparing the power response surfaces, it is apparent that the geometry of the acoustic MRI scanner model is still of influence on the acoustic response: the optimum power design for the scanner without casing is not the same as the optimum design for the scanner with casing.
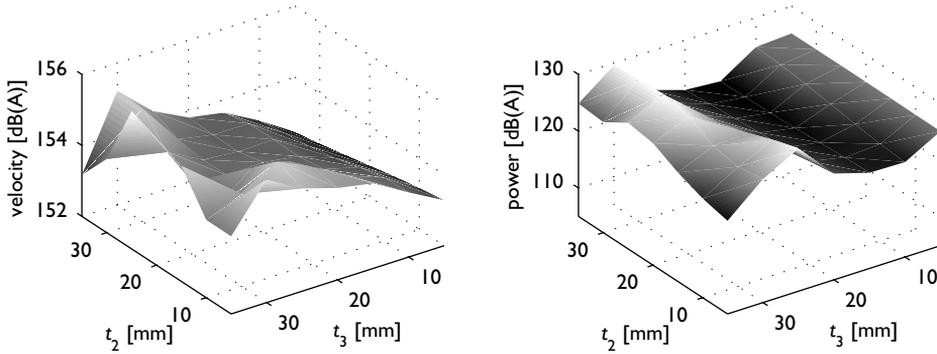
**(a)** MRI scanner model without casing.
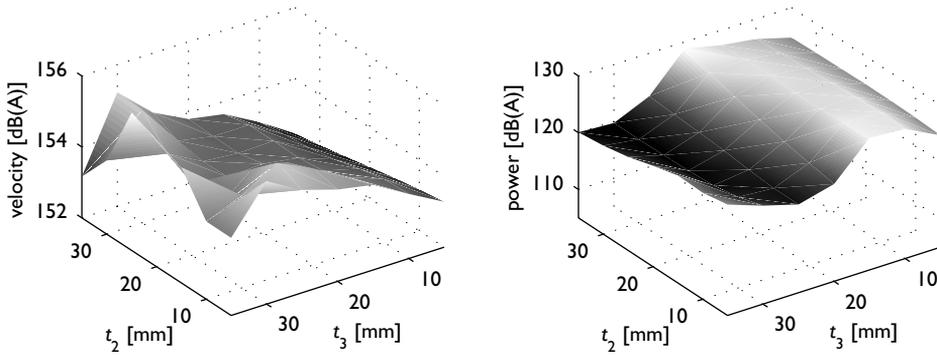


**(b)** MRI scanner model with casing.

**figure 6.20** Response surfaces for MRI scanner parameter studies 3 & 4: multiple circumferential harmonics excitation.

**table 6.2** Response values for optimum MRI designs from the design studies. the numbers 1 to 4 denote the design study number, and '*P*' and '*v*' denote an optimum with respect to sound power level and velocity level, respectively.

|  |  | 1P | 1v | 2P | 2v | 3P | 3v | 4P | 4v |
|---|---|---|---|---|---|---|---|---|---|
| $t_2$ | [mm] | 25.0 | 35.0 | 25.0 | 35.0 | 25.0 | 35.0 | 25.0 | 35.0 |
| $t_3$ | [mm] | 15.0 | 5.0 | 30.0 | 5.0 | 15.0 | 5.0 | 30.0 | 5.0 |
| $L_v$ | [dB(A) re $10^{-9}$ m/s] | 146.7 | 144.9 | 147.8 | 144.9 | 153.8 | 152.5 | 154.4 | 152.5 |
| $L_W$ | [dB(A) re $10^{-12}$ W] | 114.4 | 120.9 | 108.5 | 114.1 | 120.5 | 125.2 | 119.8 | 124.7 |
| $L_p$ | [dB(A) re $2 \cdot 10^{-5}$ Pa] | 136.3 | 140.7 | 128.7 | 132.9 |  |  |  |  |

Compared with the response surfaces for the single harmonic excitation in figures 6.15 and 6.18, the levels have increased, and the shape of the surfaces is flattened. But still, the response surface shapes for multiple harmonics excitation resemble the shapes for single harmonic excitation. This means that the optimum designs for design studies 3 and 4 are the same as for design studies 1 and 2, respectively (see table 6.2). Because the response

surface shapes have flattened, the level differences between optimum and 'worst-case' structural and acoustic designs have decreased: 3 dB for the velocity level and 9 dB for the sound power level. Note that in contrast with single harmonic excitation, the MRI scanner with casing in these studies is not intrinsically quieter than the scanner without casing.

Comparison of the response spectra for each of the scanners in figure 6.21 reveals that they are smoother than their single harmonic excitation counterparts. This is a consequence of the increased number of near cut-on resonances, due to the increased number of circumferential harmonics in the excitation. The peaks in the individual harmonic spectra might still be relatively high, but in the summed total spectra, the height of the peaks becomes less pronounced, which results in smoother spectra.

The smoothening of the acoustic spectra does not imply that the near cut-on resonances play a less important role for scanners subject to multiple harmonics excitation. This can be illustrated by the remarkable difference between the acoustic response of design 4P and 4v just above cut-on frequency $f_{11} = 360 \text{Hz}$ (see figure 6.21). For design 4P, the velocity level has a clear peak, which does not translate into a peak for the sound power level, because of the low radiation efficiency levels near that frequency. Design 4v displays the opposite behavior: the velocity level is rather smooth, but the peak in the radiation efficiency translates into a high sound pressure peak above 360 Hz. Paradoxically, a peak in the total velocity level, coinciding with a cut-on frequency does not lead to a sound power peak and on the other hand, a smooth velocity level leads to a peak in the sound power. This paradox can be explained by looking at the response levels for the individual harmonics in figure 6.22. These figures clearly show that the total level spectra are build up from the contributions of the individual circumferential harmonics. For design 4P, the velocity level peak at 360 Hz is caused by the circumferential harmonic $m = 0$, which obviously cannot couple to the first cut-on frequency $f_{11}$ for the $m = 1$ Fourier duct mode. On the other hand, for design 4v, there is a peak in the velocity level for harmonic $m = 1$ near cut-on frequency $f_{11}$, which translates in a peak for both the sound power level and radiation efficiency level. There is also a strong coupling with the $f_{02}$ and $f_{12}$ cut-on frequencies (see also table A.2(b)). This indicates that a mismatch between structural and near cut-on resonances still characterizes an optimal acoustic design, but it also indicates that the mismatch should be effectuated at the level of the individual circumferential harmonics, and not at the summed levels.

It is recognized that a resonance mismatch will probably be easier to accomplish for single harmonic excitation than for multiple harmonics excitation, since the number of structural and near cut-on resonances is much lower for single harmonic excitation. This is probably the reason why the level difference between optimum and 'worst-case' acoustic designs for single harmonic excitation are larger than for multiple harmonics excitation: 15 dB(A) versus 9 dB(A). Still, for the latter case, the spread is very significant from a designer's point of view.

### 6.4.4   Conclusions with respect to design

The optimum design of the gradient coil system was shown to depend on the geometry of the radiating surface of the scanner. When the radiating geometry is changed, so will the structural composition of the optimum design. The optimum designs for the vibration level do not necessarily coincide with optimum designs for noise levels, so the vibration level is certainly not a suitable *acoustic* design objective function. The correspondence between
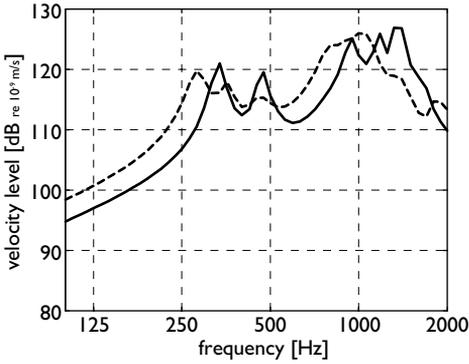
**(a)** Velocity level (without casing).
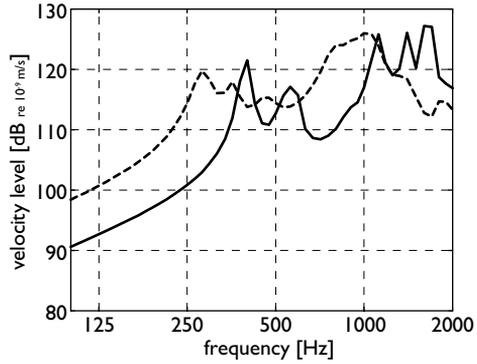
**(b)** Velocity level (with casing).
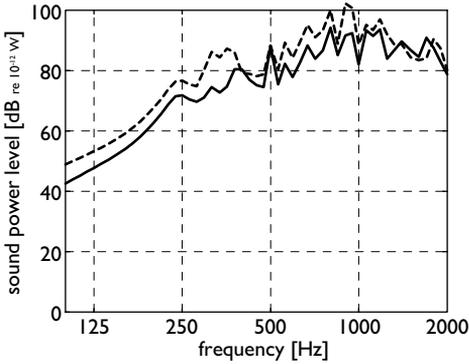
**(c)** Sound power level (without casing).
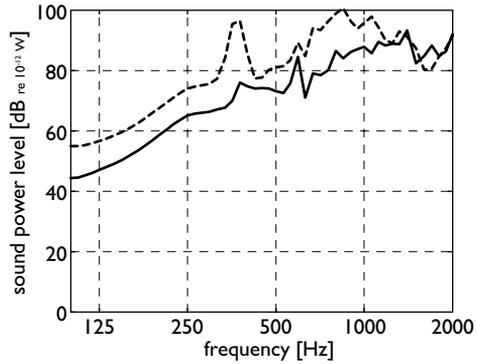
**(d)** Sound power level (with casing).
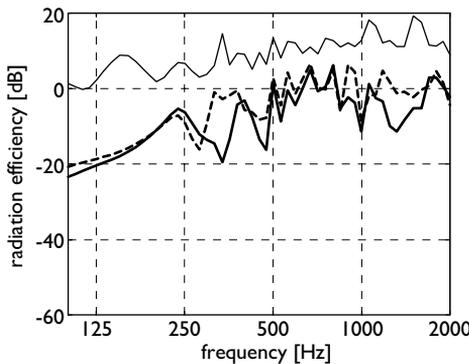
**(e)** Radiation efficiency (without casing). ——— : maximum.
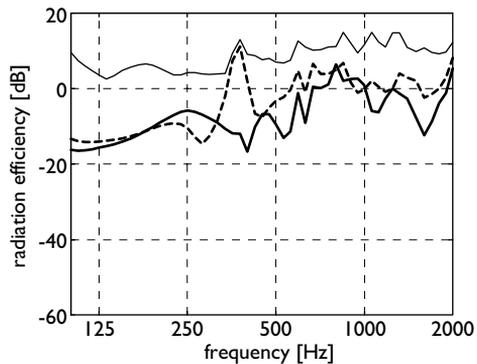
**(f)** Radiation efficiency (with casing). ——— : maximum.

**figure 6.21** Response curves for MRI scanner models with different gradient coil system designs (multiple harmonics excitation). Left graphs: scanner without casing, ——— : design 3*P*; ---- : design 3*v*. Right graphs: scanner with casing, ——— : design 4*P*; ---- : design 4*v*.

**(a)** Velocity level (design 4P).



**(b)** Velocity level (design 4v).



**(c)** Sound power level (design 4P).



**(d)** Sound power level (design 4v).
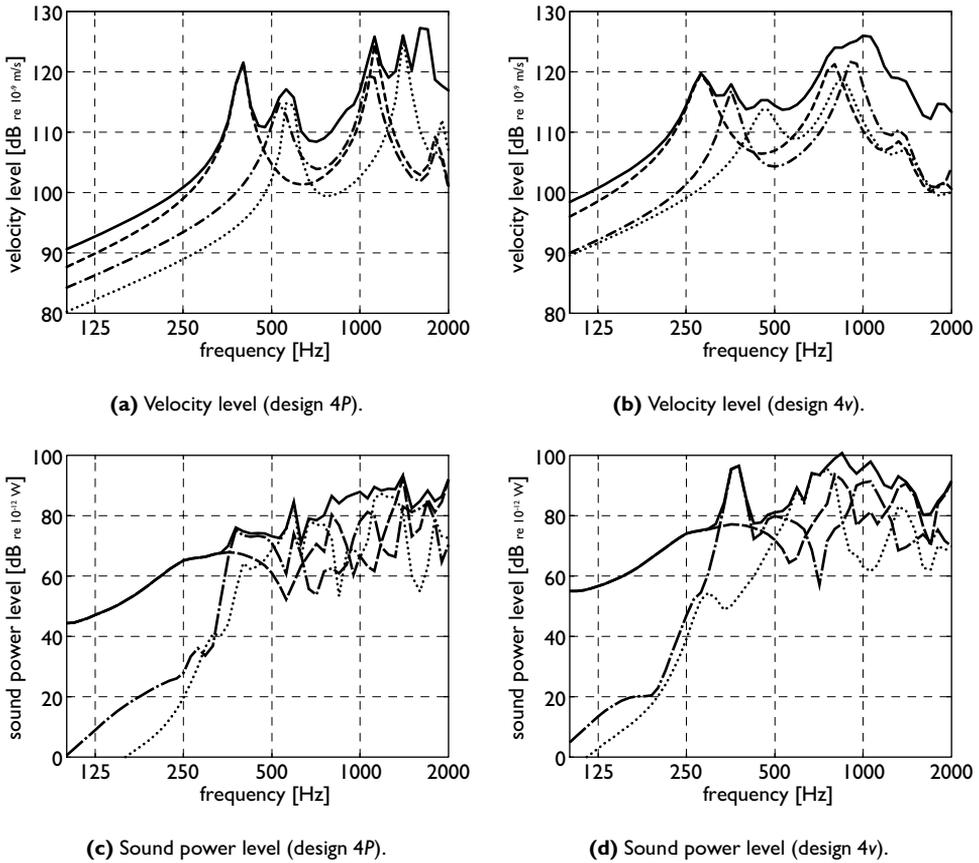
**figure 6.22** Response levels per circumferential harmonic number. ———: total; – – – –: $m = 0$; –·–·–: $m = 1$; ·········: $m = 2$.

the response surfaces of sound power and sound pressure levels was found to be good. Therefore, pressure calculations are not necessary to assess the acoustic performance in a design study. This enables the use of the radiation modes reduction technique, which significantly reduces the computation time for the acoustic design analyses.

For the design studies with both single and multiple Fourier harmonics excitation, the cut-on resonance phenomena play an important role. In these studies, acoustically optimal designs are characterized by a mismatch between vibration spectrum peaks and near cut-on resonances. This mismatch is effectuated at the level of the individual circumferential harmonics, and not at the level of the summed-up responses. It seems that this mismatch is harder to accomplish for multiple harmonics excitation because of the increased number of both structural and near cut-on resonances, with respect to single harmonic excitation. Nevertheless, a significant noise reduction with respect to the 'worst-case' design seems to be achievable.

## 6.5   Summary

Important for the sound radiation characteristics of the axisymmetric MRI scanner models are the so-called near cut-on resonances. Just above the cut-on frequency of a duct mode, a build-up acoustic pressure associated with that particular mode inside the MRI bore may occur, because of high auto-reflection coefficients at the bore's exits. This may result in a significantly increased power radiation just above the cut-on frequencies of the Fourier-Bessel duct modes. Below the first cut-on frequency, the radiation efficiency of a duct mode falls off very rapidly, so its contribution to the noise production can be neglected.

The geometry of the MRI scanner bore seems to be an important factor for the acoustic design. The bore's minimum radius was found to determine the location of the cut-on frequencies. Moreover, a gradually changing cross-sectional diameter along the axis of symmetry seems to diminish the maximum achievable radiation efficiency peaks due to the near cut-on resonances. The presence of a patient in the MRI scanner only has a very small acoustic influence, and it is therefore unnecessary for design purposes to model a patient in the scanner.

Four design studies, for an MRI scanner model with different bore geometries and different excitations, were performed to establish a suitable design objective function and to investigate the importance of the near cut-on resonances for the acoustic design. The studies showed that the sound pressure level in the bore and the radiated sound power level respond similarly to design changes. This means that the radiated sound power is suitable and sufficient as a design objective function for the MRI scanner. This is fortunate because it enables the use of the radiation modes reduction technique, in order to significantly speed up the acoustic analyses in design studies. The design studies also demonstrated that, compared to the 'worst-case' designs, a significant noise reduction of about $5 - 10$ dB(A) can be accomplished by mismatching structural vibration level peaks and near cut-on resonances, independently of the total vibration level. This indicates that the reduction of near cut-on resonances is very relevant for the acoustic design of MRI scanners. The prominence of these resonances can be decreased by changing the geometry of the bore and by altering the structural composition of the gradient coil system and the coupling with the surrounding casing.

# 7 Conclusions, discussion and recommendations

The development of acoustic tools for axisymmetric structures and their application for the design of MRI scanners was the main objective of the research that is presented in this thesis. From the acoustic designer's point of view, an essential requirement for these tools is that they accurately and efficiently predict the relevant acoustic response changes due to design alterations. Also, the tools should be sufficiently fast to ensure that design studies with these tools are feasible in an industrial environment. In this context, the research activities presented in this thesis will be summarized and discussed next. In addition, recommendations will be given which might broaden and enhance the application of the presented research results.

## 7.1 Conclusions and discussion

### 7.1.1 Baffled duct formulation

A semi-analytical model was developed to investigate the typical acoustic characteristics of a finite duct with vibrating walls and infinite flanges, which is a simplification of an MRI scanner. With this model , the acoustic radiation of a baffled finite duct is mathematically described by a convolution integral of the response of a source in a hard-walled finite duct and the vibration distribution at the wall. The efficiency of the method was increased by developing a new algorithm to compute the reflection coefficients that describe boundary conditions at the duct's exits.

The semi-analytical baffled duct model demonstrates the relationship of the MRI noise problem with duct acoustics theory. Typical infinite duct acoustic phenomena such as mode cut-on could also be observed in the MRI scanner models. Resonances are introduced in the duct just above the cut-on frequencies. These so-called near cut-on resonances, are caused by the impedance transition at the duct's exits, and explain the peak values of sound pressure, sound power and radiation efficiency that can be observed for ducts with constant cross-section. Hence this model proved to be valuable to gain insight into the important radiation characteristics of finite duct-like structures.

Because of its superior efficiency compared to element based formulations, the baffled duct model offers designers the opportunity to quickly obtain a rough impression of the important parameters, such as the scanner dimensions, in the MRI noise problem, and to obtain a global impression of the acoustic responses in the design space. However, the application of the model for detailed design studies is limited to MRI scanner geometries with constant cross-section. Because of practical and ergonomical considerations, it is

unlikely that such MRI scanners will be developed in the future. Hence, the application of the baffled duct formulation for MRI scanner design is restricted to exploratory design studies.

### 7.1.2 Fourier boundary element formulation

A novel Fourier boundary element method (Fourier BEM) was developed to analyze the acoustic radiation of axisymmetric structures. This method enables the acoustic analysis of MRI scanner geometries with non-constant bore diameter. With this method, the non-axisymmetric acoustic variables are described with Fourier series in circumferential direction. Mathematically, the three dimensional radiation problem is decomposed into a series of 'quasi-axisymmetric' radiation problems, one for each harmonic in the Fourier series expansions of the acoustic variables. In this way, the dimensionality of the problem is reduced by one. Compared with a 3-dimensional BEM formulations, the speedup factor that is achieved with the Fourier BEM is 50 to 200, depending on the problem size.

The novelty in the Fourier BEM formulation that was developed here is the algorithm that computes the Fourier integrals in circumferential direction. Traditionally this integration is performed separately for each Fourier harmonic. To decrease the computational effort for this most time-consuming step in the formulation, a new algorithm was developed, which computes the Fourier integrals simultaneously with an FFT algorithm. The speedup that is accomplished by deploying this algorithm is especially notable when the Fourier series of the boundary conditions consists of a lot of terms.

The efficiency of the Fourier BEM method makes it possible to apply it in all stages of the design process of the MRI scanner: for exploratory research as well as detailed design studies. As a part of the research, the Fourier BEM in bArd was interfaced with the structural analysis program SATURN, which is also Fourier series based. This enables designers to perform semi-automatic structural-acoustic parameter design studies, and therefore offers them a valuable tool for the acoustic design of a large class of axisymmetric MRI scanners.

The application of the Fourier BEM is certainly not restricted to MRI scanners; it can be used for various other axisymmetric acoustic radiation problems. Exemplary engineering applications of the presented Fourier BEM formulation can be found in the research of Geerts [1997] on the acoustic radiation of train wheels, and in the research of van Houten [1998] on the structural-acoustic optimization of carillon bells.

### 7.1.3 Radiation modes formulation

To obtain insight into the acoustically important components of the vibration distribution of the MRI scanner, the radiation modes formulation was used. The formulation presented in the literature was enhanced to enable the analysis of vibrating substructures in otherwise acoustically passive systems.

With the radiation modes analysis, it is possible to compute the maximum achievable radiation efficiency at each frequency, for a given radiating geometry. At frequencies where the actual radiation efficiency is near its maximum achievable value, decreasing the vibration level of both the most efficient radiation mode and in total will result in a substantial decrease of the total sound power. This design rule was found in MRI scanner studies, but is equally applicable to other vibrating structures, because the radiation modes analysis is not restricted to a specific geometry or acoustic analysis method.

Design alterations to an important class of structural parameters of sound radiating structures (e.g. the material properties, support, or load) only change the boundary conditions of the acoustic problem, not the geometry of the acoustic domain itself. This observation was exploited in a modal reduction technique, based on the radiation modes formulation. This reduction technique can be utilized in global structural-acoustic parameter or optimization design studies, in order to quickly compute the radiated sound power. For each geometry, a radiation modes analysis needs to be performed only once, and in subsequent analyses the results can be reused. This can significantly speed up the acoustic analysis part in structural-acoustic design studies. However, this advantage can only be exploited if the radiated sound power is an appropriate design objective function for low-noise design. For the MRI scanner, this is considered in section 7.1.4.

Specifically for the MRI scanner, it appears that application of the radiation modes reduction technique is advantageous for an additional reason. It was shown that a quite limited number of radiation modes is important for the acoustic behavior of the scanner. This could be explained by the cut-on effects inside the scanner bore, which limits the number of Fourier-Bessel duct modes that radiate acoustic energy outside of the bore.

### 7.1.4 Acoustic design of MRI scanners

The newly developed mathematical tools were deployed in a series of numerical experiments. These experiments demonstrate the use of these tools and answer a number of questions related to their application. First, the influence of the MRI scanner geometry on the noise production was established. The minimum duct radius of the part of the bore with constant cross-section determines the location of the cut-on frequencies and consequently the location of the near cut-on resonances. Furthermore, it was seen that a gradually changing bore radius seems to decrease the peak values of the maximum achievable radiation efficiency that are caused by these resonances. The outer diameter of the scanner only marginally influences the acoustic response in the low frequency range and is therefore an unimportant design parameter.

Next, the acoustic influence of the presence of a patient in a realistically shaped scanner was assessed. A patient with acoustically-hard clothing inside the scanner was observed to shift the location of the cut-on frequencies downwards. By introducing absorptive clothing for the patient this down-shift was canceled out. Only a moderate decrease in the radiated power and pressure was observed in the low frequency range, which was caused by the increased absorption in the acoustic system. From these observations it was concluded that it would be unnecessary to model the presence of the patient in an acoustic scanner model, because it is not expected to alter the effectiveness of acoustic design changes.

In another series of numerical experiments, the potential of the developed tools for design studies was demonstrated with four parameter studies. The gradient coil system design was varied for two different MRI scanner geometries, and two different force excitations. These studies show that the sound power level and the sound pressure level are interchangeable as design objective functions, as they respond equally to design changes. The velocity level was found to correlate poorly to the generated sound.

Another observation from these experiments is that optimum acoustic MRI designs are characterized by a mismatch between vibration level peaks and near cut-on resonances. With respect to the designs with the lowest vibration level, an additional noise reduction of about 5 dB(A) could be achieved by this mismatch. For excitations with only a

single circumferential harmonic, the difference between optimum and 'worst-case' acoustic designs is about 15 dB(A), whereas this difference for multiple harmonics excitation is smaller (about 9 dB(A)). This indicates that the mismatch for multiple harmonics excitation is harder to achieve. Nevertheless, compared to the 'worst-case', a significant noise reduction can be achieved, independently of the vibration level. The relevant design factors, that determine the mismatch, are the bore geometry and vibration distribution because they determine the acoustic radiation characteristics. The structural composition and forcing of the gradient coil system and casing are equally important design factors because they determine the vibrational behavior.

## 7.2   Recommendations

- Because of the typical acoustic behavior of MRI scanners, the acoustic models are an indispensable part in a structural-acoustic design tool. It is therefore recommended to use these models on a regular basis during the design cycle. But, it is equally important to use a suitable model in each phase of the design cycle. In the initial phase, simplified acoustic models should be used to assess the influence of conceptual structural-acoustic design changes on the noise production of MRI scanners. It will be more practical to obtain these insights by using the numerical tools than by performing extensive measurements on different MRI scanner concepts. In the subsequent engineering phase, more elaborate acoustic models should be applied for detailed design studies. With such studies, it is possible to assess the influence, of the dimensioning of different parts of the scanner, on the total structural-acoustic behavior. Finally, in the prototyping phase, experimental validation of optimum numerical designs will be inevitable, but with an adequate application of the acoustic tools, the number of necessary measurements to obtain a quieter MRI scanner design can be drastically reduced.

- The geometry of the MRI scanner bore was found to have significant influence on the radiation characteristics. Although, from an acoustic point of view, the geometry of currently available MRI scanners is not unfavorable compared to duct-like MRI scanners with constant cross-section, it might be possible to further optimize the shape to achieve a lower noise radiation. The study with the two-sided conical bore (see figure 6.9(b) indicates that the current bore geometry still leaves some room for improvements. It is worthwhile to investigate whether such improvements can be achieved.

- The variance of the acoustic response of the MRI scanner due to manufacturing and material variations was not investigated. But, such an investigation seems to be very relevant. If the difference between optimal and 'worst-case' acoustic designs is equal to the difference in sound level caused by manufacturing and material inaccuracies, then the designer might be able to formulate more strict manufacturing and material standards for low-noise MRI scanner designs. On the other hand, if the differences turn out to be small, then this indicates that the manufacturing and material standards can be relaxed from an acoustic point of view. It also indicates that a significant noise reduction can only be achieved, by applying structural changes that are more drastic than the changes introduced by the material and manufacturing variations. An investigation of these variations is therefore recommended.

- For a significant reduction of the noise levels produced by the MRI scanner, it is not sufficient to take purely acoustic measures only. A substantial noise level reduction can

only be expected when the vibration level is also decreased considerably. This might be accomplished by passively or actively isolating the gradient coil system vibration from the casing structure. An investigation of this concept is therefore recommended. The developed acoustic tools can then still be applied to investigate the effectiveness of the design measures, as long as a suitable model for the casing vibrations is available.

- The radiation modes formulation has proven to be a valuable tool in the design process, both to obtain insights into the acoustic behavior of a structure and to speed up design studies by using the modal reduction technique. For this thesis, the method was implemented for axisymmetric structures in b*Ard*, but for other kinds of structures the method is not available in commercially available acoustic software codes until now. This is unfortunate because the radiation modes formulation has a potential which is similar to the structural modes formulation in the dynamics field. Therefore, it is recommended that appropriate action is taken by the developers of (commercial) acoustics software.

- For the MRI noise problem, the structural and acoustic problems were assumed to be decoupled, and could therefore be separately solved. To enable the analysis of coupled structural-acoustic problems, an enhancement of the tools is required. Such an enhancement is quite easily realizable since the required system matrices are already computed as a part of the normal calculations with SATURN and b*Ard*. It is recommended to implement such an enhancement together with the radiation modes formulation of Chen and Ginsberg [1995]. This enables the exploitation of the advantages of the radiation modes formulation in coupled structural-acoustic analyses.

# Bibliography

**Akyol T.P. [1986]**. Schallabstrahlung von Rotationskörpern. *Acustica*, 61, pp. 200–212.

**Astley R.J. and Eversman W. [1988]**. Wave envelope elements for acoustical radiation in inhomogeneous media. *Computers & Structures*, 30, pp. 801–810.

**Astley R.J., Macaulay G.J., Coyette J.P., and Cremers L. [1998]**. Three-dimensional wave-envelope elements of variable order for acoustic radiation and scattering. Part I. Formulation in the frequency domain. *Journal of the Acoustical Society of America*, 103(1), pp. 49–63.

**bArd [1998]**. *version 3.0 manual.* Computational and Experimental Mechanics, Eindhoven University of Technology.

**Baumann W.T., Ho F.S., and Robertshaw H.S. [1992]**. Active structural acoustic control of broadband disturbances. *Journal of the Acoustical Society of America*, 92, pp. 1998–2005.

**Benthien W. and Schenck A. [1997]**. Nonexistence and nonuniqueness problems associated with integral equation methods in acoustics. *Computers & Structures*, 65(3), pp. 295–305.

**Beranek L.L. [1969]**. Audience and Chair Absorption in Large Halls. II. *Journal of the Acoustical Society of America*, 45(1), pp. 13–19.

**Borgiotti G.V. [1990]**. The power radiated by a vibrating body in an acoustic fluid and its determination from boundary measurements. *Journal of the Acoustical Society of America*, 88(4), pp. 1884–1893.

**Borgiotti G.V. and Jones K.E. [1994]**. Frequency independence property of radiation spatial filters. *Journal of the Acoustical Society of America*, 96(6), pp. 3516–3524.

**Burkhard M.D. and Sachs R.M. [1975]**. Anthropometric manikin for acoustic research. *Journal of the Acoustical Society of America*, 58(1), pp. 214–222.

**Burton A.J. and Miller G.F. [1971]**. The application of integral equation methods to the numerical solution of some exterior boundary-value problems. In *Proceedings of the Royal Society of London. A.*, pp. 201–210.

**Chen P.T. [1997]**. Vibrations of submerged structures in a heavy acoustic medium using radiation modes. *Journal of Sound and Vibration*, 208(1), pp. 55–71.

**Chen P.T. and Ginsberg J.H. [1995]**. Complex power, reciprocity, and radiation modes for submerged bodies. *Journal of the Acoustical Society of America*, 98(6), pp. 3343–3351.

**Cho Z.H., Chung S.T., Chung J.Y., Park S.H., Kim J.S., Moon C.H., and Hong**

**I.K. [1998]**. A New Silent Magnetic Resonance Imaging Using a Rotating DC Gradient. *Magnetic Resonance in Medicine*, 39, pp. 317–321.

**Choi S.H., Igusa T., and Achenbach J.D. [1996]**. Acoustic radiation from a finite-length shell with non-axisymmetric substructures using a surface variational principle. *Journal of Sound and Vibration*, 197(3), pp. 329–350.

**Ciskowski R.D. and Brebbia C.A.**, eds. **[1991]**. *Boundary Element Methods in Acoustics*. Elsevier Applied Science, London.

**Cremers L., Fyfe K.R., and Coyette J.P. [1994]**. A variable order infinite acoustic wave envelope element. *Journal of Sound and Vibration*, 171(4), pp. 483–508.

**Cunefare K.A. [1991]**. The minimum multi-modal radiation efficiency of baffled finite beams. *Journal of the Acoustical Society of America*, 90, pp. 2521–2529.

**Cunefare K.A. and Currey M.N. [1994]**. On the exterior acoustic radiation modes of structures. *Journal of the Acoustical Society of America*, 96(4), pp. 2302–2312.

**Currey M.N. and Cunefare K.A. [1995]**. The radiation modes of baffled finite plates. *Journal of the Acoustical Society of America*, 98(3), pp. 1570–1580.

**Doak P.E. [1973]**. Excitation, transmission and radiation of sound from a source in a hard-walled duct of finite length, II: The effects of duct length. *Journal of Sound and Vibration*, 31, pp. 137–174.

**Elliott S.J. and Johnson M.E. [1993]**. Radiation modes and the active control of sound power. *Journal of the Acoustical Society of America*, 94(4), pp. 2194–2204.

**Filippi P.J.T. and Habault D. [1989]**. Sound radiation by a baffled cylindrical shell: a numerical technique based on boundary integral equations. Part 1. *Journal of Sound and Vibration*, 131(1), pp. 13–23.

**Geerts N. [1997]**. Sound Radiation of Resilient Train Wheels with Sysnoise and bArd. Tech. Rep. WFW 97.031, Computational and Experimental Mechanics, Eindhoven University of Technology.

**Goldman A.M., Gossman W.E., and Friedlander P.C. [1989]**. Reduction of Sound Levels with Antinoise in MR Imaging. *Radiology*, 173, pp. 549–550.

**Grosh K., Pinsky P.M., Malhotra M., and Rao V.S. [1994]**. Finite element formulation for a baffled, fluid-loaded finite cylindrical shell. *International Journal for Numerical Methods in Engineering*, 37, pp. 2971–2985.

**Guiggiani M. and Casalini P. [1987]**. Direct computation of Cauchy principal value integrals in advanced boundary elements. *International Journal for Numerical Methods in Engineering*, 24, pp. 1711–1720.

**Habault D. and Filippi P.J.T. [1989]**. Sound radiation by a baffled cylindrical shell: a numerical technique based on boundary integral equations. Part 2. *Journal of Sound and Vibration*, 131(1), pp. 25–36.

**Harari A. and Sandman B.E. [1976]**. Vibratory response of laminated cylindrical shells embedded in an acoustic fluid. *Journal of the Acoustical Society of America*, 60, pp. 117–128.

**Hashemi R.H. and Bradley Jr. W.G. [1997]**. *MRI: The Basics*. Williams & Wilkins, Baltimore.

**Hedeen R.A. and Edelstein W.A. [1997]**. Characterization and Prediction of Gradient Acoustic Noise in MR Imagers. *Magnetic Resonance in Medicine*, 37, pp. 7–10.

**Hewlett D.A.K., Nelson P.A., and Morfey C.L. [1995]**. An exact solution for the acoustic radiation from a finite length circular duct. In *inter·noise 95*, pp. 1333–1336.

**van Houten M.H. [1998]**. *Function Approximation Concepts for Multidisciplinary Design Optimization*. Ph.D. thesis, Eindhoven University of Technology, the Netherlands.

**Hurwitz R., Lane S.R., Bell R.A., and Brant-Zawadski M.N. [1989]**. Acoustic Analysis of Gradient-Coil Noise in MR Imaging. *Radiology*, 173, pp. 545–548.

**Juhl P. [1993]**. An axisymmetric integral equation formulation for free space non-axisymmetric radiation and scattering of a known incident wave. *Journal of Sound and Vibration*, 163(3), pp. 397–406.

**Kessels P.H.L. [1999]**. *Engineering toolbox for structural-acoustic design – applied to MRI-scanners*. Ph.D. thesis, Eindhoven University of Technology, the Netherlands.

**Kessels P.H.L., Kuijpers A.H.W.M., Verbeek G., and Verheij J.W. [1998]**. Structural acoustics toolbox for understanding and reducing noise (Saturn). In *Proceedings of the inter·noise 98 conference,*. Christchurch, New-Zealand.

**Kinsler L.E., Frey A.R., Coppens A.B., and Sanders J.V. [1982]**. *Fundamentals of acoustics*. John Wiley & Sons, New York, third edn.

**Kooyman P.P. [1994]**. Vibrations and radiation of the gradient coil of an MRI device (Phase 5c, part 1). Tech. Rep. TPD-HAG-RPT-94-0085, TNO-TPD. (confidential).

**Kooyman P.P., Janssens M.H.A., van Vliet W.J., and Dittrich M.G. [1993]**. Acoustic research on a PHILIPS MR-system (Phases 1–4). Tech. Rep. TPD-HAG-RPT-93-0183, TNO-TPD. (confidential).

**Kreyszig E. [1993]**. *Advanced engineering mathematics*. John Wiley & Sons, New York, seventh edn.

**Kuijpers A.H.W.M., Rienstra S.W., Verbeek G., and Verheij J.W. [1998a]**. The acoustic radiation of baffled finite ducts with vibrating walls. *Journal of Sound and Vibration*, 216(3), pp. 461–493.

**Kuijpers A.H.W.M., Verbeek G., and Verheij J.W. [1997]**. An improved acoustic Fourier boundary element method formulation using fast Fourier transform integration. *Journal of the Acoustical Society of America*, 102(3), pp. 1394–1401.

**Kuijpers A.H.W.M., Verbeek G., and Verheij J.W. [1998b]**. Efficient low noise design of finite duct-like systems applying radiation modes. In *Proceedings of the inter·noise 98 conference,*. Christchurch, New-Zealand.

**Lamancusa J.S. [1993]**. Numerical optimization techniques for structural-acoustic design of rectangular panels. *Computers & Structures*, 48(4), pp. 661–675.

**Lean M.H. and Wexler A. [1985]**. Accurate numerical integration of singular boundary element kernels over boundaries with curvature. *International Journal for Numerical Methods in Engineering*, 21, pp. 211–228.

**Liao H. and Xu Z. [1992]**. A method for direct evaluation of singular integral in direct boundary element method. *International Journal for Numerical Methods in Engineering*, 35, pp. 1473–1485.

**Ling X.J., Amor A., and DeMeester G. [1995]**. Numerical and experimental studies of the vibration and acoustic behaviors of MRI gradient tube. In *15th Biennial conference on mechanical vibrations and noise*, vol. 84 of *Design Engineering Technical Conferences*, pp. 311–317. ASME, Boston, MA, USA.

**Matviyenko G. [1995]**. On the azimuthal Fourier components of the Green's function for the Helmholtz equation in three dimensions. *Journal of Mathematical Physics*, 36(9), pp. 5159–5169.

**Morfey C.L. [1969]**. A note on the radiation efficiency of acoustic duct modes. *Journal of Sound and Vibration*, 9(3), pp. 367–372.

**Morse P.M. and Ingard K.U. [1968]**. *Theoretical Acoustics*. McGraw-Hill, New York.

**Nagel J. [1988]**. *Handbook of biomedical engineering*, chap. 10.3, pp. 294–297. Academic Press.

**Naghshineh K., Chen W., and Koopmann G.H. [1998]**. Use of acoustic basis functions for active control of sound power radiated from a cylindrical shell. *Journal of the Acoustical Society of America*, 103(4), pp. 1897–1903.

**Naghshineh K. and Koopmann G.H. [1993]**. Active control of sound power using acoustic basis functions as surface velocity filters. *Journal of the Acoustical Society of America*, 93(5), pp. 2740–2752.

**Naghshineh K., Koopmann G.H., and Belegundu A.D. [1992]**. Material tailoring of structures to achieve a minimum radiation condition. *Journal of the Acoustical Society of America*, 92(2), pp. 841–855.

**Photiadis D.M. [1990]**. The relationship of singular value decomposition to wave-vector filtering in sound radiation problems. *Journal of the Acoustical Society of America*, 88(2), pp. 1152–1159.

**Pierce A.D. [1981]**. *Acoustics: an introduction to its principles and applications*. McGraw-Hill, New York.

**Rienstra S.W. and Hirschberg A. [1997]**. An introduction to Acoustics. Lecture notes. IWDE Report 92-06/revised June 1997.

**Sandman B.E. [1976]**. Fluid loading influence coefficients for a finite cylindrical shell. *Journal of the Acoustical Society of America*, 60, pp. 1256–1264.

**Sarkissian A. [1991]**. Acoustic radiation from finite structures. *Journal of the Acoustical Society of America*, 90, pp. 574–578.

**Schenck H.A. [1968]**. Improved integral formulation for acoustic radiation problems. *Journal of the Acoustical Society of America*, 36, pp. 41–58.

**Seybert A.F. and Rengarajan T.K. [1987]**. The use of CHIEF to obtain unique solutions for acoustic radiation problems. *Journal of the Acoustical Society of America*, 81, pp. 1299–1306.

**Seybert A.F., Wu T.W., and Wu X.F. [1994]**. *Experimental validation of finite element and boundary element methods for predicting structural vibration and radiated noise*. NASA contractor report 4561.

**Shephard Jr. W.S. and Cunefare K.A. [1997]**. Sensitivity of structural acoustic response to attachment feature scales. *Journal of the Acoustical Society of America*, 102(3), pp. 1612–1619.

**Skudrzyk E. [1971]**. *The Foundations of Acoustics*. Springer-Verlag, Vienna.

**Soenarko B. [1993]**. A boundary element formulation for radiation of acoustic waves from axisymmetric bodies with arbitrary boundary conditions. *Journal of the Acoustical Society of America*, 93(2), pp. 631–639.

**Stepanishen P.R. [1997]**. The forward projection of harmonic pressure fields using the generalized internal source density method. *Journal of the Acoustical Society of America*, 102(4), pp. 1955–1963.

**Sysnoise [1996]**. *revision 5.3 On-Line Documentation*. LMS Numerical Technologies, Leuven, Belgium.

**Termeer M. [1997]**. *Theory of acoustic radiation modes and its application to MRI scanners*. Master's thesis, Computational and Experimental Mechanics, Eindhoven University of Technology. WFW-report 97.045 (confidential).

**Verbeek G., Kuijpers A.H.W.M., and Verheij J.W. [1998]**. Radiation modes and axisymmetric duct acoustics. In *Proceedings of the inter·noise 98 conference,*. Christchurch, New-Zealand.

**Vlaardingerbroek M.T. and den Boer J. [1996]**. *Magnetic Resonance Imaging*. Springer, Berlin.

**Wang K.S. and Tszeng T.C. [1984]**. Propagation and radiation of sound in a finite length duct. *Journal of Sound and Vibration*, 93(1), pp. 57–79.

**Wang W., Atalla N., and Nicolas J. [1997]**. A boundary integral approach for acoustic radiation of axisymmetric bodies with arbitrary boundary conditions valid for all wave numbers. *Journal of the Acoustical Society of America*, 101(3), pp. 1468–1478.

**Watson G.N. [1966]**. *A treatise on the theory of Bessel functions*. Cambridge University Press, second edn.

**Zorumski W.E. [1973]**. Generalized radiation impedances and reflection coefficients of circular and annular ducts. *Journal of the Acoustical Society of America*, 54(6), pp. 1667–1673.

**Zwikker C. and Kosten C.W. [1949]**. *Sound absorbing materials*. Elsevier, New York.

# A Fourier-Bessel duct modes and their cut-on frequencies

The inflection points $j'_{m\mu}$ of $J_m(x)$ were first introduced in chapter 2. These inflection points are the zeros of the derivative $J'_m$ of the Bessel function of the first kind of order $m$ with respect to $x$,

$$\left.\frac{dJ_m}{dx}\right|_{x=j'_{m\mu}} = 0. \tag{A.1}$$

These points are used to calculate the radial wavenumbers $\alpha_{m\mu} = j'_{m\mu}/a$, and are given in table A.1 for low circumferential Fourier mode numbers $m$ and radial mode numbers $\mu$.

The cut-on frequency $f_{m\mu}$ for a Fourier-Bessel mode $(m, \mu)$ in a duct is defined as the frequency for which the axial wavenumber $k_{m\mu} = \sqrt{(k^2 - \alpha^2_{m\mu})}$ equals zero. With duct radius $a$ and speed of sound $c_0$ this frequency is given by,

$$f_{m\mu} \equiv \frac{j'_{m\mu} c_0}{2\pi a}. \tag{A.2}$$

A Fourier-Bessel duct mode is called cut-on if the excitation frequency is above the mode's cut-on frequency. If the frequency is below the cut-on frequency, the mode is called cut-off and cannot radiate energy out of the duct. Using the speed of sound in air, $c_0 = 343 \text{ m s}^{-1}$, the cut-on frequencies for ducts with radii of $a = 0.3405$ m and $a = 0.28$ m are given in tables A.2(a) and A.2(b), respectively.

Figure A.1 illustrates some simple mode shapes in a cross-section of the duct. The number $m$ denotes the number of *nodal diameters* and the number $\mu$ denotes the number of *nodal circles minus one* for the pressure expansion.

table A.1 Zeros of $J'_m$ for Fourier mode number $m$ and radial mode number $\mu$.

| $m$ | $\mu = 1$ | $\mu = 2$ | $\mu = 3$ | $\mu = 4$ |
|---|---|---|---|---|
| 0 | 0.00 | 3.83 | 7.02 | 10.17 |
| 1 | 1.84 | 5.33 | 8.54 | 11.71 |
| 2 | 3.05 | 6.71 | 9.97 | 13.17 |
| 3 | 4.20 | 8.02 | 11.35 | 14.59 |
| 4 | 5.32 | 9.28 | 12.68 | 15.96 |
| 5 | 6.41 | 10.52 | 13.99 | 17.31 |

**table A.2** Cut-on frequencies $f_{m\mu}$ in Hz for two different duct radii $a$, for Fourier mode number $m = 1 \ldots 10$ and radial mode number $\mu$. Frequencies above 2000 Hz were not included.

| (a) $a = 0.3405$ m | | | | | (b) $a = 0.28$ m | | | |
|---|---|---|---|---|---|---|---|---|
| $m$ | $\mu = 1$ | $\mu = 2$ | $\mu = 3$ | $\mu = 4$ | $m$ | $\mu = 1$ | $\mu = 2$ | $\mu = 3$ | $\mu = 4$ |
| 0 | 0 | 615 | 1125 | 1631 | 0 | 0 | 748 | 1368 | 1984 |
| 1 | 296 | 855 | 1368 | 1877 | 1 | 360 | 1040 | 1664 | |
| 2 | 490 | 1075 | 1598 | | 2 | 596 | 1307 | 1943 | |
| 3 | 674 | 1285 | 1819 | | 3 | 820 | 1563 | | |
| 4 | 852 | 1489 | | | 4 | 1036 | 1810 | | |
| 5 | 1028 | 1686 | | | 5 | 1251 | | | |
| 6 | 1203 | 1881 | | | 6 | 1463 | | | |
| 7 | 1375 | | | | 7 | 1672 | | | |
| 8 | 1546 | | | | 8 | 1880 | | | |
| 9 | 1718 | | | | 9 | | | | |
| 10 | 1888 | | | | 10 | | | | |
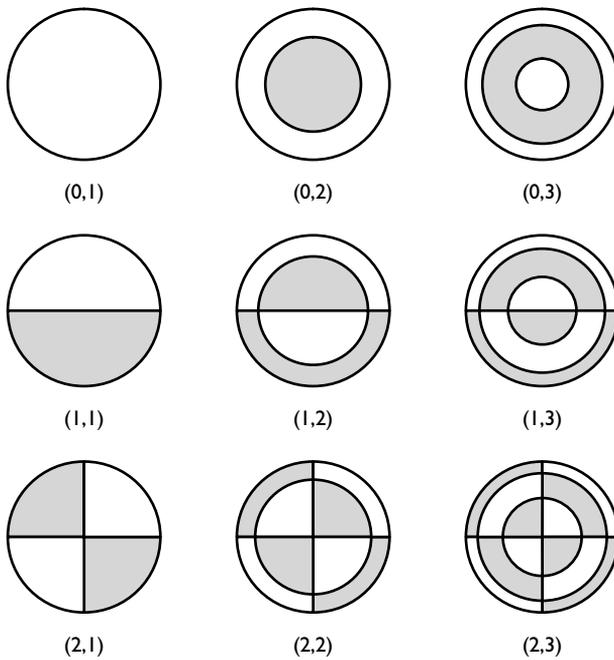


**figure A.1** Fourier-Bessel mode shapes for the pressure inside the duct. The notation $(m, \mu)$ denotes the circumferential and radial order of the mode. The white sections indicate positive and the grey sections denote negative acoustic pressure values.

# B  Computation of generalized radiation impedances

## B.1  Calculation of Fourier integrals with the residue integration method

The residue integration method can be used to calculate integrals of the form

$$\int_{-\infty}^{\infty} \frac{\text{num}(\gamma)}{\text{den}(\gamma)} e^{-i\gamma z} d\gamma,$$

and was used in section 2.2.3 to compute Fourier integrals. The residue integration theorem [e.g., Kreyszig, 1993,chap 15] states that for a meromorphic integrand $f(\gamma)$ (i.e. analytic on the complex plane except for isolated poles) with simple poles $\gamma_i$ inside a contour $C$,

$$C = \{-R < \gamma < R, \text{Im } \gamma = 0\} \cup \{\gamma = Re^{i\theta}, 0 \le \theta \le \pi\}, \tag{B.1}$$

its contour integral around $C$ equals the summation of its residues at the simple poles,

$$\oint_C f(\gamma) d\gamma = 2\pi i \sum_{\gamma_i} \underset{\gamma=\gamma_i}{\text{Res}} f(\gamma), \tag{B.2}$$

$$\underset{\gamma=\gamma_i}{\text{Res}} f(\gamma) = \underset{\gamma=\gamma_i}{\text{Res}} \frac{\text{num}(\gamma)}{\text{den}(\gamma)} e^{-i\gamma z} = \frac{\text{num}(\gamma_i)}{\frac{d}{d\gamma} \text{den}(\gamma)\big|_{\gamma_i}} e^{-i\gamma_i z} = \frac{\text{num}(\gamma_i)}{\text{den}'(\gamma_i)} e^{-i\gamma_i z}, \tag{B.3}$$

where the integral is being taken counterclockwise around the contour $C$. This contour can be split up into a part along the real axis and a semi-circle $S$,

$$\oint_C f(\gamma) d\gamma = \int_{-R}^{R} f(\gamma) d\gamma + \int_S f(\gamma) d\gamma. \tag{B.4}$$

This result can be used to compute the Fourier integral in equation (2.17), as will be shown in the following. The Fourier integral in this equation has a meromorphic integrand with its poles at the zeros for $J'_m(\alpha a)$, at $\gamma = \pm k_{m\mu}$. If the limit $R \to \infty$ is taken and Jordan's lemma is used, it can be shown that the integral over path $S$ equals zero under certain conditions for path $S$ and $z$. This happens for the integral when $S$ closes the contour via
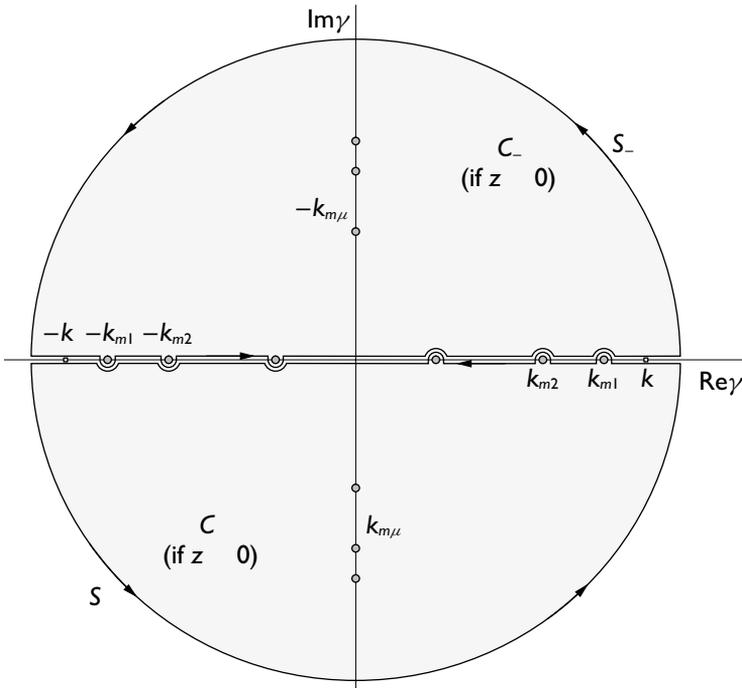
**figure B.1** Integration path in the $\gamma$-plane.

the lower half plane for positive $z$ ($C = C_+$ and $S = S_+$) and via the upper half plane for negative $z$ ($C = C_-$ and $S = S_-$). This is illustrated in figure B.1. Then the contour integral over $C_+$ or $C_-$ in the complex plane gives an expression for the Fourier integral for positive and negative $z$, respectively. In mathematical terms:

$$\oint_{C_+} f(\gamma)\mathrm{d}\gamma = -\int_R^{-R} f(\gamma)\mathrm{d}\gamma + \int_{S_+} f(\gamma)\mathrm{d}\gamma$$

$$\Rightarrow \int_{-\infty}^{\infty} f(\gamma)\mathrm{d}\gamma = -\lim_{R\to\infty} \oint_{C_+} f(\gamma)\mathrm{d}\gamma = -2\pi\mathrm{i} \sum_{\gamma_i = k_{m\mu}} \frac{\mathrm{num}(\gamma_i)}{\mathrm{den}'(\gamma_i)} e^{-\mathrm{i}\gamma z}, \qquad \text{for } z \geq 0, \quad \text{(B.5)}$$

$$\oint_{C_-} f(\gamma)\mathrm{d}\gamma = \int_{-R}^{R} f(\gamma)\mathrm{d}\gamma + \int_{S_-} f(\gamma)\mathrm{d}\gamma$$

$$\Rightarrow \int_{-\infty}^{\infty} f(\gamma)\mathrm{d}\gamma = \lim_{R\to\infty} \oint_{C_-} f(\gamma)\mathrm{d}\gamma = 2\pi\mathrm{i} \sum_{\gamma_i = -k_{m\mu}} \frac{\mathrm{num}(\gamma_i)}{\mathrm{den}'(\gamma_i)} e^{-\mathrm{i}\gamma z}, \qquad \text{for } z < 0. \quad \text{(B.6)}$$

In this way, the Fourier integral in equation (2.17)

$$\int\limits_{-\infty}^{\infty} \frac{J_m(\alpha r)}{\alpha a J_m'(\alpha a)} e^{-i\gamma z} d\gamma,$$

can be computed with the residue integration method.

A problem here is the fact that a finite number of poles of the integrand is located on the integration contour, between $-k$ and $k$. This makes the result of the integration ambiguous. The integral is to be interpreted via a suitable deformation of the contour (the integral of a meromorphic function does not change with deformation of the integration contour *within the region of analyticity*). However, this is either over or under the singularity, and the results are not the same. So, without further information this would leave us, for each singularity, with two possible but different answers!

The argument in order here is causality (i.e. any physical solution vanishes for $t \to -\infty$) which with the present $e^{i\omega t}$ notation requires the solution to be the analytical continuation in $\omega$ from the lower complex $\omega$ half plane. If a small negative imaginary part is added to $\omega$, it is easily verified that the poles $\gamma = k_{m\mu}$ shift to the lower half plane, and the poles $\gamma = -k_{m\mu}$ to the upper half plane. So, the contour of integration should be indented under $-k_{m\mu}$ and over $+k_{m\mu}$, as depicted in figure B.1 [see also Skudrzyk, 1971,p.652ff].

The residues for the Fourier integral can be written as

$$\operatorname*{Res}_{\gamma=\gamma_i}\left(\frac{J_m(\alpha(\gamma)r)}{\alpha(\gamma)a J_m'(\alpha(\gamma)a)} e^{-i\gamma z}\right) = \left.\frac{J_m(\alpha(\gamma)r)}{a\frac{d\alpha(\gamma)}{d\gamma}[\alpha(\gamma)a J_m''(\alpha(\gamma)a) + J_m'(\alpha(\gamma)a)]} e^{-i\gamma z}\right|_{\gamma=\gamma_i}$$

$$= \frac{-\alpha(\gamma_i)J_m(\alpha(\gamma_i)r)}{a\gamma_i[\alpha(\gamma_i)a J_m''(\alpha(\gamma_i)a) + J_m'(\alpha(\gamma_i)a)]} e^{-i\gamma_i z} \tag{B.7}$$

$$= \begin{cases} \frac{1}{a^2 k_{m\mu}} \frac{\alpha_{m\mu}^2 a^2}{\alpha_{m\mu}^2 a^2 - m^2} \frac{J_m(\alpha_{m\mu}r)}{J_m(\alpha_{m\mu}a)} e^{-ik_{m\mu}z} & \text{for } z \geq 0, \\[2ex] \frac{-1}{a^2 k_{m\mu}} \frac{\alpha_{m\mu}^2 a^2}{\alpha_{m\mu}^2 a^2 - m^2} \frac{J_m(\alpha_{m\mu}r)}{J_m(\alpha_{m\mu}a)} e^{ik_{m\mu}z} & \text{for } z < 0. \end{cases}$$

With this result the Fourier integral can be written as

$$\int\limits_{-\infty}^{\infty} \frac{J_m(\alpha r)}{\alpha a J_m'(\alpha a)} e^{-i\gamma z} d\gamma = -2\pi i \sum_{\mu=1}^{\infty} \frac{\alpha_{m\mu}^2 a^2}{\alpha_{m\mu}^2 a^2 - m^2} \frac{J_m(\alpha_{m\mu}r)}{J_m(\alpha_{m\mu}a)} e^{-ik_{m\mu}|z|}. \tag{B.8}$$

## B.2 Generalized radiation impedances

The pressure and velocity at the exit of a finite duct that terminates in an infinite flange can be written as (see section 2.2.5)

$$p(r_e, \theta_e, z_e) = \sum_{m=-\infty}^{\infty} e^{-im\theta_e} \sum_{\mu=1}^{\infty} P_{m\mu}J_m(\alpha_{m\mu}r_e), \tag{B.9}$$

$$u_z(r_e, \theta_e, z_e) = \frac{1}{\rho_0 c_0} \sum_{m=-\infty}^{\infty} e^{-im\theta_e} \sum_{\mu=1}^{\infty} V_{m\mu}J_m(\alpha_{m\mu}r_e), \tag{B.10}$$

with coordinates $\boldsymbol{x}_e = (r_e, \theta_e, z_e)$ for a point at the duct's exit. The pressure at a point $\boldsymbol{x} = (r, \theta, z)$ outside the duct ($z \leq -L$ or $z \geq L$) is given by the Rayleigh integral which

depends on the (axial) velocity at the duct's exit:

$$p(\mathbf{x}) = \frac{i\rho_0\omega}{2\pi} \int\limits_{S_e} u_z(\mathbf{x}_e) \frac{e^{-ikR(\mathbf{x},\mathbf{x}_e)}}{R(\mathbf{x},\mathbf{x}_e)} dS, \tag{B.11}$$

where

$$R(\mathbf{x},\mathbf{x}_e) = |\mathbf{x} - \mathbf{x}_e| = \left[ r^2 + r_e^2 - 2rr_e \cos(\theta - \theta_e) + (z - z_e)^2 \right]^{\frac{1}{2}} \tag{B.12}$$

is the distance between a point outside the duct and a point in the duct's exit, and $S_e$ is the cross-section of the duct's exit. The expression for $u_z(\mathbf{x}_e)$ from equation (B.10) can be substituted into the Rayleigh integral to obtain

$$p(r,\theta,z) = \frac{ik}{2\pi} \int\limits_0^{2\pi} \int\limits_0^a \sum_{m=-\infty}^{\infty} e^{-im\theta_e} \sum_{\mu=1}^{\infty} V_{m\mu} J_m(\alpha_{m\mu}r_e) \frac{e^{-ikR}}{R} r_e dr_e d\theta_e. \tag{B.13}$$

For further manipulation it is convenient to eliminate the function of $R$ in equation (B.13). Sonine's infinite integral [Watson, 1966,p. 416, eqn. (4), with $\text{Im}(\sqrt{1-\tau^2}) \leq 0$ and the complex integration contour passes above the real axis] is introduced:

$$\frac{e^{-ikR}}{-ikR} = \int\limits_0^{\infty} \frac{\tau}{\sqrt{1-\tau^2}} J_0(\tau kR) d\tau. \tag{B.14}$$

The Bessel function in equation (B.14) may be replaced, at the duct's exit ($z = z_e$ and thus $R = R(r,\theta,r_e,\theta_e)$), by use of Neumann's addition theorem [Watson, 1966,p. 358, eqn. (1)]:

$$J_0(\tau kR) = \sum_{m=-\infty}^{\infty} J_m(\tau kr) J_m(\tau kr_e) e^{-im(\theta-\theta_e)}. \tag{B.15}$$

Substituting equation (B.15) in equation (B.14) results in

$$\frac{e^{-ikR}}{R} = -ik \sum_{m=-\infty}^{\infty} e^{-im(\theta-\theta_e)} \int\limits_0^{\infty} \frac{\tau}{\sqrt{1-\tau^2}} J_m(\tau kr) J_m(\tau kr_e) d\tau. \tag{B.16}$$

With this result, equation (B.13) (at $z = z_e$) can now be expressed as

$$p(r,\theta,z_e) = k \sum_{m=-\infty}^{\infty} e^{-im\theta} \sum_{\mu=1}^{\infty} V_{m\mu} \int\limits_0^{\infty} \frac{\tau}{\sqrt{1-\tau^2}} J_m(\tau kr) D_{m\mu}(\tau) d\tau, \tag{B.17}$$

where the integration over angle $\theta_e$ has been performed and function $D_{m\mu}(\tau)$ is given by

$$D_{m\mu}(\tau) = k \int\limits_0^a J_m(\tau kr) J_m(\alpha_{m\mu}r) r dr. \tag{B.18}$$

The integral $D_{m\mu}(\tau)$ may be evaluated directly [Watson, 1966, p. 134, eqn. (8)]:

$$D_{m\mu}(\tau) = \frac{\tau k^2 a}{\tau^2 k^2 - \alpha_{m\mu}^2} J_m'(\tau ka) J_m(\alpha_{m\mu}a). \tag{B.19}$$

Equation (B.9) can now be equated to (B.17) to obtain

$$\sum_{m=-\infty}^{\infty} e^{-im\theta} \sum_{\mu=1}^{\infty} P_{m\mu} J_m(\alpha_{m\mu}r) =$$

$$k \sum_{n=-\infty}^{\infty} e^{-in\theta} \sum_{v=1}^{\infty} V_{nv} \int_0^{\infty} \frac{\tau}{\sqrt{1-\tau^2}} J_n(\tau kr) D_{nv}(\tau) d\tau. \tag{B.20}$$

Multiplying both sides of this equation by $e^{ip\theta} J_p(\alpha_{p\xi}r)$ and integrating over the duct's cross-section while exchanging the summation and integration operators gives

$$\sum_{m=-\infty}^{\infty} \sum_{\mu=1}^{\infty} P_{m\mu} \int_0^{2\pi} \int_0^a J_m(\alpha_{m\mu}r) e^{-im\theta} J_p(\alpha_{p\xi}r) e^{ip\theta} r dr d\theta =$$

$$k \sum_{n=-\infty}^{\infty} \sum_{v=1}^{\infty} V_{nv} \int_0^{\infty} \frac{\tau}{\sqrt{1-\tau^2}} \int_0^{2\pi} \int_0^a J_n(\tau kr) e^{-in\theta} J_p(\alpha_{p\xi}r) e^{ip\theta} r dr d\theta D_{nv}(\tau) d\tau. \tag{B.21}$$

The orthogonality property for the modes in radial and circumferential direction gives for the left hand side of equation (B.21) (where $\alpha_{m\mu}$ and $\alpha_{p\xi}$ are zeros of $J_m'(\alpha a)$, $J_p'(\alpha a)$, respectively):

$$\int_0^{2\pi} \int_0^a J_m(\alpha_{m\mu}r) e^{-im\theta} J_p(\alpha_{p\xi}r) e^{ip\theta} r dr d\theta$$

$$\tag{B.22}$$

$$= \delta_{mp}\delta_{\mu\xi}\pi(a^2 - m^2/\alpha_{m\mu}^2) J_m(\alpha_{m\mu}a)^2$$

$$= \delta_{mp}\delta_{\mu\xi} 2\pi N_{m\mu}^2 \qquad \text{for } m = 0, \pm 1, \pm 2, \ldots, \text{ and for } \mu = 1, 2, \ldots.$$

The amplitude of each pressure mode at the duct's exit are then given by

$$P_{m\mu} = \frac{k}{N_{m\mu}^2} \sum_{v=1}^{\infty} V_{mv} \int_0^{\infty} \frac{\tau}{\sqrt{1-\tau^2}} \int_0^a J_m(\tau kr) J_m(\alpha_{m\mu}r) r dr D_{mv}(\tau) d\tau,$$

which can be further simplified by using the definition for $D_{m\mu}(\tau)$ to obtain

$$P_{m\mu} = \sum_{v=1}^{\infty} \frac{V_{mv}}{N_{m\mu}^2} \int_0^{\infty} \frac{\tau}{\sqrt{1-\tau^2}} D_{m\mu}(\tau) D_{mv}(\tau) d\tau. \tag{B.23}$$

Equation (B.23) may be used to express the modal impedance given by

$$P_{m\mu} = \sum_{v=1}^{\infty} Z_{m\mu v} V_{mv}, \qquad \text{for } m = 0, \pm 1, \pm 2, \ldots, \text{ and for } \mu = 1, 2, \ldots, \tag{B.24}$$

where

$$Z_{m\mu\nu} = \frac{1}{N_{m\mu}^2} \int\limits_0^\infty \frac{\tau}{\sqrt{1-\tau^2}} D_{m\mu}(\tau) D_{m\nu}(\tau) d\tau, \tag{B.25}$$

and the boundary conditions are satisfied such that $J'(\alpha_{m\mu}a) = 0$.

## B.3   Computation of generalized radiation impedances

To compute the integral in equation (B.25), Zorumski [1973] suggested to split up the integration range in a part $\tau \in [0, 1]$ and $\tau \in [1, \infty]$. By using change of variables $\tau = \sin\phi$ for the first range and $\tau = \cosh\psi$ for the second, the expression for the generalized modal impedance becomes

$$\begin{aligned} Z_{m\mu\nu} = &\frac{1}{N_{m\mu}^2} \int\limits_0^{\frac{1}{2}\pi} \sin\phi D_{m\mu}(\sin\phi) D_{m\nu}(\sin\phi) d\phi \\ &+ \frac{i}{N_{m\mu}^2} \int\limits_0^\infty \cosh\psi D_{m\mu}(\cosh\psi) D_{m\nu}(\cosh\psi) d\psi. \end{aligned} \tag{B.26}$$

At first sight, this seems to be an elegant solution since the integral is split up in a real and imaginary part, and the singularity for $\tau = 1$ has been removed by the transformation. However, because of the oscillatory nature of the function $D_{m\mu}(\tau)$, numerical evaluation of the integral is very expensive. To make things worse, the oscillatory behavior of the integrand is blown up by the $\cosh(\psi)$ argument of the function $D_{m\mu}(\tau)$. In brief, the transformations suggested by Zorumski [1973] do not offer a numerically workable expression for the generalized radiation impedances. Together with Rienstra [cf. Kuijpers et al., 1998a] an alternative, numerically more attractive expression was therefore derived, which will be presented here.

For further manipulation it is convenient to write out $Z_{m\mu\nu}$ as

$$Z_{m\mu\nu} = \frac{2\alpha_{m\mu}^2 a^2 J_m(\alpha_{m\nu}a)}{(\alpha_{m\mu}^2 a^2 - m^2) J_m(\alpha_{m\mu}a)} \int\limits_0^\infty \frac{\tau^3 J'_m(\tau ka)^2}{\sqrt{1-\tau^2}(\tau^2 - \frac{\alpha_{m\mu}^2}{k^2})(\tau^2 - \frac{\alpha_{m\nu}^2}{k^2})} d\tau. \tag{B.27}$$

Note that

$$\frac{J'_m(\tau ka)}{(\tau^2 - \frac{\alpha_{m\mu}^2}{k^2})}$$

is analytic (even at $\tau = \alpha_{m\mu}/k$). Equation (B.27) can be rewritten to

$$Z_{m\mu\nu} = E_{m\mu\nu} \int\limits_0^\infty F_{m\mu\nu}(\tau) \left[ H_m^{(1)'}(\tau ka) + H_m^{(2)'}(\tau ka) \right] d\tau, \tag{B.28}$$

with Hankel functions

$$H_m^{(1)}(x) = J_m(x) + iY_m(x), \tag{B.29}$$

$$H_m^{(2)}(x) = J_m(x) - iY_m(x), \tag{B.30}$$

and

$$E_{m\mu\nu} = \frac{2\alpha_{m\mu}^2 a^2 J_m(\alpha_{m\nu}a)}{(\alpha_{m\mu}^2 a^2 - m^2) J_m(\alpha_{m\mu}a)}, \tag{B.31}$$

and

$$F_{m\mu\nu}(\tau) = \frac{1}{2} \frac{\tau^3}{\sqrt{1-\tau^2}} \frac{1}{(\tau + \alpha_{m\mu}/k)(\tau + \alpha_{m\nu}/k)} \frac{J_m'(\tau ka)}{(\tau - \alpha_{m\mu}/k)(\tau - \alpha_{m\nu}/k)}. \tag{B.32}$$

The function $F_{m\mu\nu}(\tau)$ is analytic, except for the case $\mu = \nu$ when the poles coincide. Rewriting equation (B.28) yields

$$Z_{m\mu\nu} = E_{m\mu\nu} \left[ \oint_0^\infty F_{m\mu\nu}(\tau) H_m^{(1)'}(\tau ka) d\tau + \oint_0^\infty F_{m\mu\nu}(\tau) H_m^{(2)'}(\tau ka) d\tau \right] \tag{B.33}$$

$$= E_{m\mu\nu} \left[ Z_{m\mu\nu}^{(1)} + Z_{m\mu\nu}^{(2)} \right], \tag{B.34}$$

where $\oint$ denotes that the integration path is deformed and passes above the pole $\tau = \alpha_{m\mu}/k$ for $\mu = \nu$. These integrals can be computed by using contour deformation in the complex plane. With the help of the equations

$$H_m^{(1)'}(ix) = \frac{2}{\pi}(-i)^{m+2} K_m'(x), \quad \arg(x) \in (-\pi, \tfrac{1}{2}\pi], \tag{B.35}$$

$$H_m^{(2)'}(-ix) = \frac{2}{\pi}(i)^{m+2} K_m'(x), \quad \arg(x) \in (-\tfrac{1}{2}\pi, \pi], \tag{B.36}$$

with the modified Hankel function

$$K_m(x) = \begin{cases} \frac{1}{2}\pi i^{m+1} H_m^{(1)}(ix), & \arg(x) \in (-\pi, \tfrac{1}{2}\pi], \\ \frac{1}{2}\pi i^{m+1} H_m^{(1)}(ix) - 2\pi i(-1)^m I_m(x), & \arg(x) \in (\tfrac{1}{2}\pi, \pi], \end{cases} \tag{B.37}$$

$$= \begin{cases} \frac{1}{2}\pi (-i)^{m+1} H_m^{(2)}(-ix), & \arg(x) \in (-\tfrac{1}{2}\pi, \pi], \\ \frac{1}{2}\pi (-i)^{m+1} H_m^{(2)}(-ix) + 2\pi i(-1)^m I_m(x), & \arg(x) \in (-\pi, -\tfrac{1}{2}\pi], \end{cases} \tag{B.38}$$

and with the modified Bessel function of the first kind

$$I_m(x) = i^{-m} J_m(ix), \tag{B.39}$$

the components of equation (B.34) can be written as

$$Z^{(1)}_{m\mu\nu} = \int_0^\infty F_{m\mu\nu}(\mathrm{i}\tau)\frac{2}{\pi}(-\mathrm{i})^{m+1}K'_m(\tau ka)\mathrm{d}\tau, \tag{B.40}$$

$$Z^{(2)}_{m\mu\nu} = 2\int_0^1 F_{m\mu\nu}(\tau)H_m^{(2)\prime}(\tau ka)\mathrm{d}\tau + \int_0^\infty F_{m\mu\nu}(-\mathrm{i}\tau)\frac{2}{\pi}\mathrm{i}^{m+1}K'_m(\tau ka)\mathrm{d}\tau$$
$$+\,\delta_{\mu\nu}2\pi\mathrm{i}\operatorname*{Res}_{\tau=\alpha_{m\mu}/k}F_{m\mu\mu}(\tau)H_m^{(2)\prime}(\tau ka). \tag{B.41}$$

Combining these terms yields

$$Z_{m\mu\nu} = 2E_{m\mu\nu}\left[\int_0^1 F_{m\mu\nu}(\tau)H_m^{(2)\prime}(\tau ka)\mathrm{d}\tau + \frac{\mathrm{i}}{\pi}\int_0^\infty \frac{\tau^3 I'_m(\tau ka)K'_m(\tau ka)}{\sqrt{1+\tau^2}(\tau^2+\frac{\alpha^2_{m\mu}}{k^2})(\tau^2+\frac{\alpha^2_{m\nu}}{k^2})}\mathrm{d}\tau\right.$$
$$\left. +\,\delta_{\mu\nu}\pi\mathrm{i}\operatorname*{Res}_{\tau=\alpha_{m\mu}/k}F_{m\mu\mu}(\tau)H_m^{(2)\prime}(\tau ka)\right]. \tag{B.42}$$

The singularity in $F_{m\mu\nu}(\tau)$ for $\tau = 1$ in equation (B.42) can be removed by substituting $\tau = \sin(\theta)$:

$$\int_0^1 \frac{\tau^3}{2\sqrt{1-\tau^2}}\frac{J'_m(\tau ka)H_m^{(2)\prime}(\tau ka)}{(\tau^2-\alpha^2_{m\mu}/k^2)(\tau^2-\alpha^2_{m\nu}/k^2)}\mathrm{d}\tau =$$

$$\int_0^{\frac{1}{2}\pi}\frac{\sin^3(\theta)J'_m(\sin(\theta)ka)H_m^{(2)\prime}(\sin(\theta)ka)}{2(\sin^2(\theta)-\alpha^2_{m\mu}/k^2)(\sin^2(\theta)-\alpha^2_{m\nu}/k^2)}\mathrm{d}\theta. \tag{B.43}$$

The infinite integral in equation (B.42) can be transformed to two finite integrals by splitting the integration interval $[0,\infty]$ into $[0,1]$ and $[1,\infty]$ and using the substitution $t = 1/\tau$ for the second interval:

$$\int_0^\infty \frac{\tau^3 I'_m(\tau ka)K'_m(\tau ka)}{\sqrt{1+\tau^2}(\tau^2+\frac{\alpha^2_{m\mu}}{k^2})(\tau^2+\frac{\alpha^2_{m\nu}}{k^2})}\mathrm{d}\tau =$$

$$\int_0^1 \frac{\tau^3 I'_m(\tau ka)K'_m(\tau ka)}{\sqrt{1+\tau^2}(\tau^2+\frac{\alpha^2_{m\mu}}{k^2})(\tau^2+\frac{\alpha^2_{m\nu}}{k^2})}\mathrm{d}\tau + \int_0^1 \frac{I'_m(ka/t)K'_m(ka/t)}{\sqrt{t^2+1}(1+\frac{\alpha^2_{m\mu}t^2}{k^2})(1+\frac{\alpha^2_{m\nu}t^2}{k^2})}\mathrm{d}t. \tag{B.44}$$

With limits

$$\lim_{x\to 0}x^2 I'_m(x)K'_m(x) = \begin{cases}-\frac{1}{2}x^2 & \text{for } m=0,\\ -\frac{1}{2}m & \text{for } m\geq 1,\end{cases} \tag{B.45}$$

$$\lim_{x\to\infty}I'_m(x)K'_m(x) = 0, \tag{B.46}$$

it can be shown that the first integrand approaches zero for $\tau \to 0$, and that the second integrand also approaches zero for $t \to 0$.

When $\mu = \nu$ the residue at pole $\tau = \alpha_{m\mu} = \alpha_{m\nu}$ has to be taken into account. Four cases can be distinguished: (1) the pole is not on the branch of $1/\sqrt{1 - \tau^2}$; (2) the pole lies on the branch of $1/\sqrt{1 - \tau^2}$, but not in 0 or 1; (3) the pole lies at $\tau = 0$; (4) the pole lies at $\tau = 1$.

In case (1) $\tau > 1$ or $\alpha_{m\mu}/k = \alpha_{m\nu}/k > 1$. This means that the free field wavenumber $k$ is smaller than radial wavenumber $\alpha_{m\mu}$, in other words, the mode is cut-off (evanescent). The residue at this pole is

$$\operatorname*{Res}_{\tau = \alpha_{m\mu}/k} E_{m\mu\mu} F_{m\mu\mu}(\tau) H_m^{(2)\prime}(\tau ka) = \frac{E_{m\mu\mu}(\alpha_{m\mu}^2 a^2 - m^2)}{4\pi \alpha_{m\mu}^2 a^2 \sqrt{(\alpha_{m\mu}/k)^2 - 1}}. \tag{B.47}$$

In case (2) $0 < \tau < 1$ or $0 < \alpha_{m\mu}/k < 1$ the pole lies on the branch of $1/\sqrt{1 - \tau^2}$. This means that the free field wavenumber $k$ is larger than radial wavenumber $\alpha_{m\mu}$, in other words, the mode is cut-on (propagating). The pole is not inside the integration contour, and it can be shown that it has no contribution to the modal impedance. However, the finite integral in equation (B.42) must then be interpreted as a Cauchy Principal Value integral:

$$Z_{m\mu\mu} = 2E_{m\mu\mu} \left[ \operatorname{CPV} \int_0^1 F_{m\mu\mu}(\tau) H_m^{(2)\prime}(\tau ka) d\tau + \frac{i}{\pi} \int_0^\infty \frac{\tau^3 I_m'(\tau ka) K_m'(\tau ka)}{\sqrt{1 + \tau^2}(\tau^2 + \frac{\alpha_{m\mu}^2}{k^2})^2} d\tau \right]. \tag{B.48}$$

In case (3) the pole lies on $\tau = \alpha_{m\mu}/k = 0$. This can only happen for the plane wave mode ($m = 0$, $\mu = \nu = 1$ and $\alpha_{01} = 0$). The modal impedance is then defined as

$$Z_{011} = 2E_{011} \int_0^\infty \frac{J_1^2(\tau ka)}{2\tau \sqrt{1 - \tau^2}} d\tau. \tag{B.49}$$

The identity

$$J_1(x) = \frac{1}{2} \left[ H_1^{(1)}(x) + H_1^{(2)}(x) \right],$$

is used to transform the integral in equation (B.49) into

$$Z_{011} = E_{011} \lim_{\varepsilon \to 0} \left[ \int_\varepsilon^\infty \frac{J_1(\tau ka) H_1^{(1)}(\tau ka)}{2\tau \sqrt{1 - \tau^2}} d\tau + \int_\varepsilon^\infty \frac{J_1(\tau ka) H_1^{(2)}(\tau ka)}{2\tau \sqrt{1 - \tau^2}} d\tau \right]. \tag{B.50}$$

Deformation of the complex integration path similar to the derivation used for equation (B.34) can be used. It can be shown that the pole at $\tau = 0$ has no contribution. The resulting expression for the modal 'self' impedance of the plane wave,

$$Z_{011} = 2E_{011} \lim_{\varepsilon \to 0} \left[ 2 \int_\varepsilon^1 \frac{J_1(\tau ka) H_1^{(2)}(\tau ka)}{2\tau \sqrt{1 - \tau^2}} d\tau - \frac{i}{\pi} \int_\varepsilon^\infty \frac{I_1(\tau ka) K_1(\tau ka)}{\tau \sqrt{1 + \tau^2}} d\tau \right], \tag{B.51}$$

contains two integrals whose integrands are singular for $\varepsilon \to 0$, but their contributions cancel each other. Therefore, it is convenient to combine the integrands in the region $\tau \in [0, 1]$:

$$Z_{011} = 2E_{011} \left\{ \int_0^1 \left[ \frac{J_1(\tau ka)H_1^{(2)}(\tau ka)}{2\tau\sqrt{1-\tau^2}} - \frac{i}{\pi} \frac{I_1(\tau ka)K_1(\tau ka)}{\tau\sqrt{1+\tau^2}} \right] d\tau \right.$$

$$\left. - \frac{i}{\pi} \int_1^\infty \frac{I_1(\tau ka)K_1(\tau ka)}{\tau\sqrt{1+\tau^2}} d\tau \right\}. \quad (B.52)$$

The singularity in the first integrand for $\tau = 1$ can be removed by substituting $\tau = \sin(\theta)$ and the second integral can be transformed into a finite integral by substituting $\tau = 1/t$. Thus, the modal impedance is defined by

$$Z_{011} = 2E_{011} \left\{ \int_0^{\frac{1}{2}\pi} \left[ \frac{J_1(ka\sin\theta)H_1^{(2)}(ka\sin\theta)}{2\sin\theta} - \frac{i}{\pi} \frac{I_1(ka\sin\theta)K_1(ka\sin\theta)\cos\theta}{\sin\theta\sqrt{1+\sin^2\theta}} \right] d\theta \right.$$

$$\left. - \frac{i}{\pi} \int_0^1 \frac{I_1(ka/t)K_1(ka/t)}{\sqrt{t^2+1}} dt \right\}. \quad (B.53)$$

In case (4) the pole lies on $\tau = \alpha_{m\mu}/k = 1$. This means that the free field wavenumber $k$ equals the radial wavenumber $\alpha_{m\mu}$. The axial wavenumber: $k_{m\mu} = \sqrt{(k^2 - \alpha_{m\mu}^2)}$ then equals zero. Physically, this occurs at duct mode resonance frequencies which are not studied here.

## B.4    Radiated acoustic power

To obtain an expression for the time-averaged power radiated by the baffled finite duct, that was used in section 2.3.2, the time average of the acoustic normal intensity $\bar{I} \cdot n$ has to be integrated over a surface that surrounds the duct,

$$\bar{P} = \int_S \bar{I} \cdot n \, dS, \quad (B.54)$$

with surface $S$, $I = pu$ as the acoustic energy flux vector, and $n$ as the unit normal vector. The bar notation $^-$ denotes the time average.

### B.4.1    Duct wall power radiation

The radiated power by the duct can be computed by integrating the time-averaged product of acoustic pressure $p$ and normal velocity $u_r$ over the duct wall surface:

$$\bar{P} = -\frac{1}{2} \text{Re} \int_{-L}^L \int_0^{2\pi} p(a, \theta, z) u_r^*(a, \theta, z) a \, d\theta \, dz, \quad (B.55)$$

where $*$ denotes the complex conjugate. By using equation (2.37) for pressure $p$ and equation (2.20) for normal velocity $u_r$ the following expression for the acoustic normal intensity at the duct wall can be derived:

$$\bar{I} \cdot \boldsymbol{n} = \frac{1}{2\pi} \sum_{m=-\infty}^{\infty} e^{-im\theta} \sum_{n=-\infty}^{\infty} \eta_n^*(z) e^{in\theta} \sum_{\mu=1}^{\infty} J_m(\alpha_{m\mu}a) \left[ A_{m\mu}(z) e^{-ik_{m\mu}z} + B_{m\mu}(z) e^{ik_{m\mu}z} \right].$$

(B.56)

Integrating this expression over the duct wall surface yields

$$\bar{P} = \frac{1}{2} a \operatorname{Re} \sum_{m=-\infty}^{\infty} \sum_{\mu=1}^{\infty} J_m(\alpha_{m\mu}a) \int_{-L}^{L} \eta_m^*(z) \left[ A_{m\mu}(z) e^{-ik_{m\mu}z} + B_{m\mu}(z) e^{ik_{m\mu}z} \right] dz.$$

(B.57)

## B.4.2 Duct exit power radiation

The transmitted power in the axial (positive z) direction $P_z$ over a duct's cross-section can be computed by integrating the time-averaged product of acoustic pressure $p$ and axial velocity $u_z$ over the cross-section:

$$\bar{P}_z(z) = \frac{1}{2} \operatorname{Re} \int_0^a \int_0^{2\pi} p(r, \theta, z) u_z^*(r, \theta, z) r d\theta dr.$$

(B.58)

Using equation (2.37) for pressure $p$, and

$$u_z(r, \theta, z) = \sum_{m=-\infty}^{\infty} \sum_{\mu=1}^{\infty} J_m(\alpha_{m\mu}r) e^{-im\theta} \frac{k_{m\mu}}{\rho_0 c_0 k} \left( A_{m\mu}(z) e^{-ik_{m\mu}z} - B_{m\mu}(z) e^{ik_{m\mu}z} \right)$$

(B.59)

for axial velocity $u_z$, the following expression for the acoustic axial intensity at the duct's exit can be derived:

$$\bar{I} \cdot \boldsymbol{e}_z = \sum_{m=-\infty}^{\infty} \sum_{n=-\infty}^{\infty} \sum_{\mu=1}^{\infty} \sum_{\nu=1}^{\infty} e^{-im\theta} e^{in\theta} J_m(\alpha_{m\mu}r) J_n(\alpha_{n\nu}r) \frac{k_{n\nu}^*}{k\rho_0 c_0} \times$$

$$\left[ A_{m\mu}(z) A_{n\nu}^*(z) e^{-i(k_{m\mu} - k_{n\nu}^*)z} - A_{m\mu}(z) B_{n\nu}^*(z) e^{-i(k_{m\mu} + k_{n\nu}^*)z} \right.$$

$$\left. + B_{m\mu}(z) A_{n\nu}^*(z) e^{i(k_{m\mu} + k_{n\nu}^*)z} - B_{m\mu}(z) B_{n\nu}^*(z) e^{i(k_{m\mu} - k_{n\nu}^*)z} \right].$$

(B.60)

Integrating this expression over the duct's cross-section yields

$$\bar{P}_z(z) = \sum_{m=-\infty}^{\infty} \sum_{\mu=1}^{\infty} \frac{\pi N_{m\mu}^2}{\rho_0 c_0 k} \times$$

$$\left\{ \operatorname{Re}(k_{m\mu}) \left[ |A_{m\mu}(z)|^2 - |B_{m\mu}(z)|^2 \right] + 2 \operatorname{Im}(k_{m\mu}) \operatorname{Im} \left[ A_{m\mu}^*(z) B_{m\mu}(z) \right] \right\}.$$

(B.61)

with $N_{m\mu}^2$ from equation (B.22). The total acoustic power radiated out of the duct can then be computed with

$$\bar{P} = \bar{P}_z(L) - \bar{P}_z(-L).$$

(B.62)

# C  Gradient coil system excitation

In chapters 5 and 6 the acoustic domain outside the MRI scanner is excited by vibrations of the gradient coil system. This vibration distribution was calculated with a structural finite element method (FEM) model of the gradient coil system, which was derived from Kessels [1999]. The structural model is axisymmetric, but the excitation is non-axisymmetric, so Fourier elements were used in the FEM calculations. These FEM calculations were performed with the program SATURN [Kessels et al., 1998].

The gradient coil system was modeled as a thick-walled cylinder with five homogeneous layers: a composite (copper/epoxy) conductor layer of 10 mm, an epoxy layer of 30 mm , a glass layer of 20 mm, and again a 30 mm epoxy layer and a 10 mm composite conductor layer, respectively, see figure C.1. The material properties of the gradient coil system layers can be found in table C.1.

The geometry of the gradient coil cylinder was chosen to resemble a real gradient coil system, with a total length of $2l = 1.455$ m, and an inner radius of $a = 0.3405$ m. The cylinder was rigidly supported at the ends and was excited using a stylized realistic Lorentz force distribution derived from Kessels [1999]. The force was assumed to be frequency
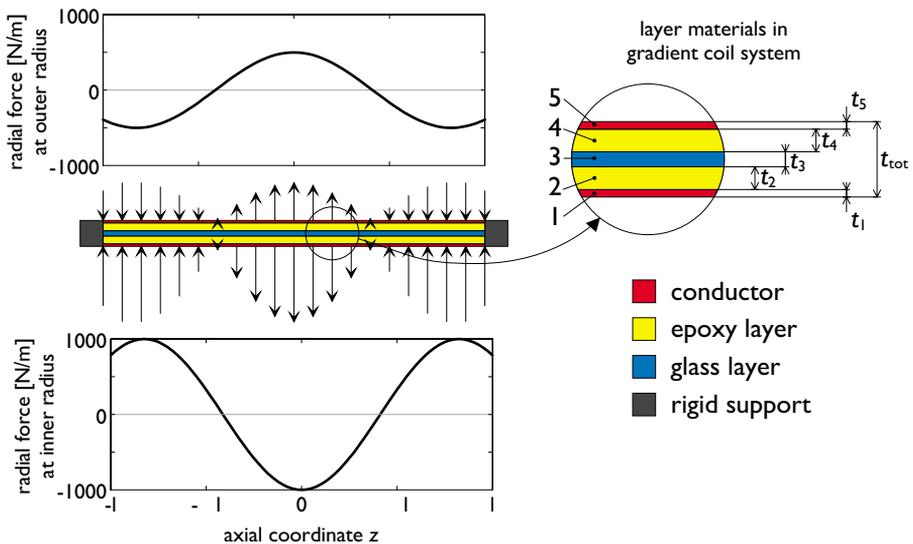


**figure C.1** Description of the material layers of the gradient coil system and the stylized Lorentz force distributions for the structural FEM calculations.

**table C.1** Material properties of the gradient coil system layers.

|  |  | layers 1,5 (composite) | | layers 2,4 | layer 3 |
|---|---|---|---|---|---|
|  |  | epoxy | copper | epoxy | glass (Pyrex) |
| Young's modulus | [GPa] | $3.4 + 0.68i$ | 117.0 | $3.4 + 0.68i$ | 62.0 |
| Poisson's ratio | [−] | 0.35 | 0.30 | 0.35 | 0.24 |
| density | [kg m$^{-3}$] | 1250 | 8941 | 1250 | 2300 |
| volume fraction | [−] | 0.05 | 0.95 | 1.00 | 1.00 |

independent to account for a large class of possible frequency spectra. Since the force excitation level for the first circumferential harmonic $m = 1$ was dominant, only this harmonic was used in the structural calculations. The resulting vibration distribution is a function of the frequency and has complex amplitudes because of the material damping in the epoxy layer. The resulting vibration level spectrum is shown in figure 5.2.

In this thesis, the term representative vibration distribution is used for the vibrations which were computed as outlined here. But these vibrations are only representative to a certain extent. Firstly, the force distribution is not the real distribution but a stylized version, both spatially and as a function of the frequency. Secondly, the materials that were used here are similar to, but not exactly the same as materials used in gradient coil systems produced nowadays. Measurements of the vibration levels [Kooyman et al., 1993; Kessels, 1999] show that the resonance peaks that are present in the computed vibration level are lower in practice. Thirdly, the computed vibration distribution only contains the $m = 1$ circumferential harmonic, while a vibration distribution of real scanner's gradient coil system also has other harmonics. This is probably caused by imperfections in the materials in circumferential direction [Kessels, 1999]. This will be shortly discussed next.

In the structural Fourier FEM model used here, the material layers are assumed to be homogeneous. But, in practice the layers are not homogeneous. Instead, small imperfections in circumferential direction exist, which causes a coupling of the separate Fourier harmonic responses. So, the excitation with an $m = 1$ force harmonic can result in multiple circumferential harmonics in the vibration response [Kessels, 1999]. The imperfections could not be handled by the Fourier finite element method that was used for this thesis, so this coupling behavior has been neglected; here the vibrations only contain the $m = 1$ harmonic component. Therefore, the vibration distribution used here is only representative for gradient coil systems with purely homogeneous material layers, or for gradient coil systems where the cross coupling of the harmonics can be neglected. An improved Fourier finite element method which can handle material imperfections is described by Kessels [1999], together with an extensive discussion about the implications of structural harmonics coupling for the MRI scanner model.

# Acknowledgements

Gratitude goes out to everyone who has supported me with the research and writing of this thesis. I would like to thank personally, in *random* order: my fellow Ph.D. student Peter Kessels, with whom I've worked together very pleasantly in the MRI project; my daily coach Bert Verbeek for his friendship, valuable comments and suggestions during the project, and of course for the 'Domus sessions'; my supervisors Jan Verheij and Dick van Campen for initiating the project and their always fruitful remarks; Sjoerd Rienstra for his help with the semi-analytical model; the people at Philips Medical Systems: especially Jan Konijn and Hans Tuithof; Jean-Pierre Coyette and Christophe Lecomte for their help with the Fourier BEM model; my students Jeroen Starreveld, Martijn Termeer, and Ruud Vermeulen; the participants in the STW meetings: Bert Schoofs, Rens Kodde, Bram de Kraker, Bert Roozen, Frank Kistemaker, Michael Dittrich, Paul de Vos, Frans van den Beemt, Peter-Paul Kooyman and Rick van Haaren; my (former) roomies: Hans, Leo, Marcel, Pascal, Wilco, and Wim for putting up with me; my colleagues at the Computational and Experimental Mechanics group; Linus Thorvalds for starting the Linux revolution; the LATEX community for an excellent typesetting system; Fritz, Heinz, and Pluk (a.k.a. Dollie); Toos & Noud Kuijpers; Sjoost for the cover design; The Paladins; the Korsakovies; and of course Yvonne for her love and patient support throughout the years.